Mathematical Modelling of the Mitochondrial Dicarboxylate Carrier (SlC25A10)

Ramin Nashebi*[1], Elías Vera-Sigüenza[3], Yingying Lyu[2], Daniel A. Tennant[2], and Fabian Spill†[1]

[1] *School of Mathematics, University of Birmingham, Birmingham, United Kingdom*
[2] *Institute of Metabolism and Systems Research, College of Medical and Dental Sciences, University of Birmingham, Birmingham, United Kingdom*
[3] *Okinawa Institute of Science and Technology Graduate University (OIST), Information Theory, Probability, and Statistics Unit, Okinawa, Japan*

1 Abstract

The mitochondrial dicarboxylate carrier SLC25A10 exchanges phosphate with dicarboxylates such as succinate and malate, playing a central role in metabolic regulation. Structural studies establish a ping–pong mechanism, but most mathematical models still assume sequential binding, lacking mechanistic justification and overlooking the alternation of a single binding site. Here, we present the first mechanistically derived and thermodynamically consistent model of SLC25A10 based on the ping–pong framework. The model incorporates competitive dicarboxylate binding, phosphate exchange, heteroexchange, reversibility, and electroneutrality, and is validated against experimental data. To estimate kinetic parameters and quantify their uncertainty, we employed Bayesian inference, enabling statistically rigorous calibration to competition assays. The model introduces new terms that quantify which substrate and from which side of the membrane is most likely to start the transport cycle. Beyond reproducing rapid exchange of different substrates that cannot be directly measured experimentally, the model captures the influence of mitochondrial morphology, enzymatic interactions, and metabolic perturbations on transporter behavior. Specifically, simulations reveal that swelling of the matrix and intermembrane space dilutes metabolite pools, reduces gradients, and decreases SLC25A10 fluxes. Moreover, the model demonstrates how SLC25A10 contributes to succinate handling under SDH deficiency, functioning both as a gatekeeper and a pressure-release valve for matrix succinate. Under these conditions, succinate accumulates and is exported into the intermembrane space via SLC25A10, a process critically dependent on phosphate and malate availability.

*Corresponding author: `rxn315@student.bham.ac.uk`
†Corresponding author: `f.spill@bham.ac.uk`

Keywords

Ping–Pong Mechanism; Bayesian Inference; MCMC; Succinate Metabolism; Mitochondrial Transport Mechanistic Modeling

2 Introduction

The solute carrier family 25 member A10 (SLC25A10), also known as the dicarboxylate carrier, is a transporter located in the inner mitochondrial membrane (IMM) [1, 2, 3, 4, 5, 6]. As its name suggests, this carrier facilitates the exchange of substrates containing two carboxyl groups, such as succinate and malate, together with other anions including inorganic phosphate, sulfate and thiosulfate [2, 4, 7, 8]. This exchanger plays a crucial role in the replenishment of intermediates of the tricarboxylic acid (TCA) cycle, supports oxidative phosphorylation, and maintains redox balance by enabling bidirectional exchange of metabolites [5, 4].

Under conditions such as cancer or ischaemia, SLC25A10 can become increasingly important in regulating succinate and malate levels [5, 2, 4, 9, 10, 11]. Evidence points towards SLC25A10 being a key player in the regulation of carbon metabolism under these circumstances, where its activity may contribute to the induction of a pseudo-hypoxic cellular state that promotes tumorigenesis [12, 13, 14].

Mechanically, SLC25A10 functions as a secondary active antiporter. It does not consume ATP directly, but instead utilizes concentration gradients —-particularly phosphate— to drive dicarboxylate exchange [15, 16, 17, 2]. Transport is reversible, meaning that substrates can move in either direction depending on relative gradients, and it supports both homoexchange, the exchange of identical metabolites (e.g., succinate-for-succinate), and heteroexchange, the exchange of different metabolites (e.g., phosphate-for-succinate). Since similar-charged molecules are exchanged in a strict 1:1 stoichiometry, the process is electroneutral and therefore insensitive to mitochondrial membrane potential [15]. Importantly, transport competition between dicarboxylates is well established, with malate generally exhibiting higher binding affinity than succinate [3, 15, 16, 17].

Recent structural studies by Ruprecht et al. [18, 4] and Mavridou et al. [19] have shown that mitochondrial carriers of the SLC25 family, including SLC25A10, function as monomers with a single substrate binding site located in a water-filled cavity. This site is accessible from one side of the inner mitochondrial membrane at a time, consistent with an alternating-access mechanism. Complementary kinetic analyzes by Cimadamore-Werthein et al. [1] demonstrated that these carriers operate through a ping–pong exchange mechanism, in which a substrate is bound, translocated and released before the counter-substrate can bind. Together, these structural and kinetic results support a single-displacement alternating mechanism, while challenging earlier sequential models that proposed that phosphate and dicarboxylates could bind simultaneously at distinct sites and be co-transported through conformational changes [3, 20, 21, 22, 23, 24, 15, 16, 17]. This combined evidence provides a strong motivation for revisiting the mathematical modeling of SLC25A10 within a ping pong kinetic framework.

An additional but underexplored layer of regulation is the effect of mitochondrial morphology on SLC25A10 transporter fluxes. Both experimental and computational studies have demonstrated that alterations in the relative volumes of the mitochondrial

matrix (MM) and intermembrane space (IMS), strongly influence metabolite diffusion and SLC25-mediated exchange rates [25, 26, 27, 28, 29]. In particular, swelling of the matrix or IMS dilutes metabolite pools and reduces effective concentration gradients. Because SLC25A10 transport relies on substrate gradients rather than ATP hydrolysis for energy, the relative volumes of the matrix and IMS directly determine the magnitude of its fluxes. Thus, it is worth exploring how volume changes modulate SLC25A10 activity at a coarse-grained level.

Several mathematical models have been developed to explore the kinetics of SLC25A10 [15, 16, 17]. While these models incorporate important features such as electroneutral heteroexchange, competitive inhibition, and thermodynamic constraints, they are generally based on a sequential mechanism and rely on the King–Altman method [30]—a graphical approach that simplifies kinetics but lacks mechanistic depth. As a result, these models are considered conceptual or proxy representations rather than mechanistically derived systems.

In this study, we present the first mechanistically derived and thermodynamically validated kinetic model of the mitochondrial dicarboxylate carrier SLC25A10 based on the ping–pong mechanism. Our framework integrates competitive binding of succinate, malate, and phosphate, phosphate-coupled heteroexchange, reversibility, and electroneutrality, and is calibrated against experimental data using Bayesian inference. In contrast to earlier sequential formulations, our model introduces conformational bias weights that quantify how different substrates bias the initiation of the ping–pong cycle, providing a mechanistic way to capture directional preferences in transporter activity. Beyond reproducing classical transport assays, the model extends experimental observations by revealing mechanistic features that are difficult to probe directly, including transient exchange dynamics, the influence of mitochondrial morphology, and the rewiring of transport behavior under succinate dehydrogenase (SDH) deficiency. In doing so, the model provides a predictive and generalizable framework for studying SLC25A10 and related mitochondrial carriers, linking transporter kinetics to broader physiological and pathological processes such as cancer metabolism and processes in which aberrantly high or low metabolite levels alter transporter activity.

3 Model and Methods

3.1 Model Construction

The ping-pong kinetic mechanism describes an alternating-access process in which the transporter cycles between two distinct conformational states, each exposing a single substrate-binding site to one side of the membrane. This mechanism prevents simultaneous binding of counter-substrates and ensures strictly alternating translocation. In the mitochondrial matrix, we consider a system where succinate (S_m) and malate (M_m) compete for binding to the carrier. The transporter in its initial state, with the binding site facing the mitochondrial matrix, is denoted T_m (Fig. 2).

Binding of either succinate or malate to T_m depends on their concentrations and binding affinities. When succinate (Fig. 2a) or malate (Fig. 2b) binds, a transient substrate–transporter complex (T_mS_m or T_mM_m) is formed [31, 1]. This association triggers a conformational change that reorients the binding site to the IMS, yielding the state

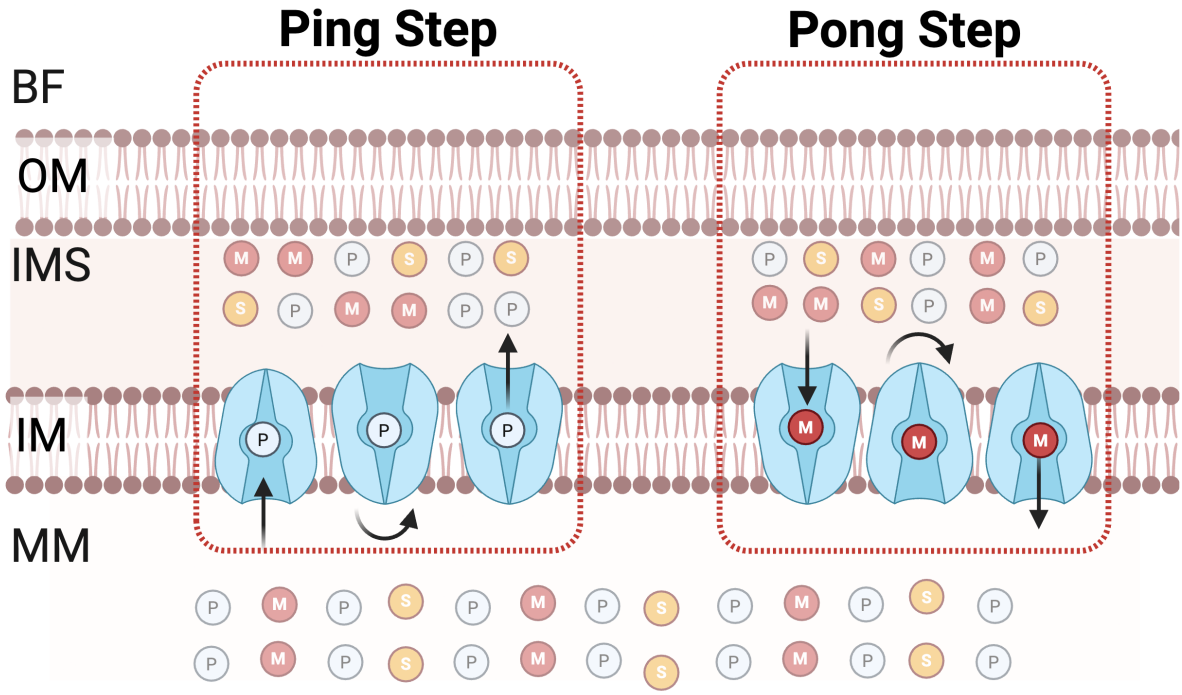

Figure 1: Schematic representation of the SLC25A10 transporter in the IMM, operating via a ping–pong mechanism. The dicarboxylates succinate (S, yellow) and malate (M, red) are exchanged with phosphate (P, white) across the IMM via SLC25A10. In the *ping* step, phosphate is exported from the matrix to the IMS: binding of phosphate is followed by a conformational change and subsequent release into the IMS. In the *pong* step, the vacant binding site is occupied by a malate, which is then imported into the matrix: binding of the malate is followed by a conformational change and final release into the matrix. Created with BioRender.com.

T_{ims}. In this configuration, the transporter preferentially releases the bound dicarboxylate into the IMS and becomes available to bind the counter-substrate phosphate (P_{ims}) [32]. Upon phosphate binding, the transporter reverts to its original matrix-facing state (T_m) and releases phosphate into the matrix (P_m), thereby completing the transport cycle.

A central feature of this mechanism is that the driving substrate—the one moving down its concentration gradient—powers the uphill transport of the counter-substrate [33, 34, 35]. The carrier first binds the driving substrate (e.g., a dicarboxylate in the matrix), releases it across the membrane, then binds the driven substrate (e.g., phosphate) on the opposite side, and translocates it against its gradient. Thus, SLC25A10 flexibly couples the direction of antiport to the relative concentration gradients: if the dicarboxylate gradient is dominant, succinate or malate drive phosphate import, whereas under phosphate-rich conditions, phosphate efflux can drive dicarboxylate uptake. Importantly, this cycle is fully reversible, meaning that transport can proceed in either direction depending solely on the prevailing substrate gradients, ensuring thermodynamic consistency and adaptability to changing metabolic demands [1].

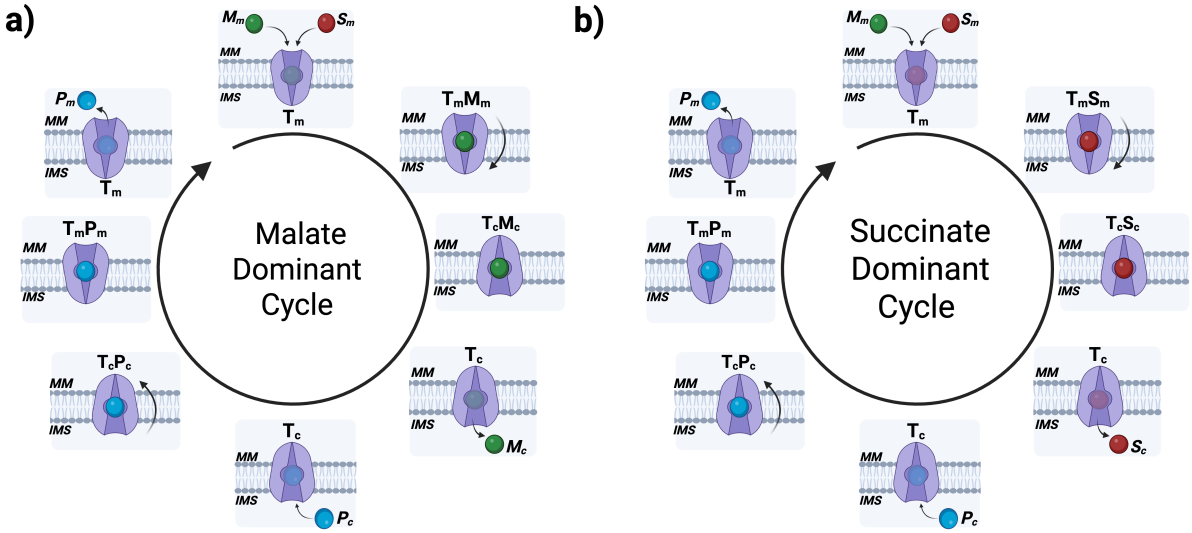

Figure 2: Ping–pong mechanism of the SLC25A10 transporter. (a) Malate dominant cycle: malate is imported in exchange for phosphate. **(b)** Succinate dominant cycle: succinate is imported in exchange for phosphate. The transporter alternates between a matrix-facing (T_m) and IMS-facing (T_{ims}) state, binding and releasing one substrate at a time. Created with BioRender.com.

3.1.1 Chemical Reaction Network of the Ping-Pong Mechanism

The reaction begins with the competitive binding of mitochondrial succinate (S_m) and malate (M_m) to the transporter in its matrix-facing conformation (T_m). Succinate binds to form the complex T_mS_m, or malate binds to form T_mM_m. These reversible reactions are characterized by forward (k_1^s, k_1^m) and backward (k_{-1}^s, k_{-1}^m) rate constants:

$$T_m + S_m \underset{k_{-1}^s}{\overset{k_1^s}{\rightleftharpoons}} T_mS_m, \tag{R1}$$

$$T_m + M_m \underset{k_{-1}^m}{\overset{k_1^m}{\rightleftharpoons}} T_mM_m. \tag{R2}$$

Once formed, the transporter–substrate complexes undergo conformational changes to expose the binding site to the IMS. For succinate and malate, these transitions occur with rate constants k_c^s, k_{-c}^s and k_c^m, k_{-c}^m, respectively:

$$T_mS_m \underset{k_{-c}^s}{\overset{k_c^s}{\rightleftharpoons}} T_{ims}S_m, \tag{R3}$$

$$T_mM_m \underset{k_{-c}^m}{\overset{k_c^m}{\rightleftharpoons}} T_{ims}M_m. \tag{R4}$$

At the IMS side, the transporter releases the bound dicarboxylate, regenerating the free transporter in its IMS-facing state with release rate constants k_3^s and k_3^m, and corresponding reverse rates k_{-3}^s and k_{-3}^m. These reactions leave the transporter in its modified state (T_{ims}), poised for subsequent interactions in the alternating-access cycle:

$$T_{ims}S_m \underset{k_{-3}^s}{\overset{k_3^s}{\rightleftharpoons}} T_{ims} + S_{ims}, \tag{R5}$$

$$T_{ims}M_m \underset{k_{-3}^m}{\overset{k_3^m}{\rightleftharpoons}} T_{ims} + M_{ims}. \tag{R6}$$

In its IMS-facing conformation (T_{ims}), the transporter binds phosphate (P_{ims}) to form the complex $T_{ims}P_{ims}$. This reversible step is governed by the forward (k_1^p) and backward (k_{-1}^p) rate constants:

$$T_{ims} + P_{ims} \underset{k_{-1}^p}{\overset{k_1^p}{\rightleftharpoons}} T_{ims}P_{ims}, \tag{R7}$$

The complex then undergoes a conformational change to the matrix-facing state with forward (k_c^p) and backward (k_{-c}^p) rate constants:

$$T_{ims}P_{ims} \underset{k_{-c}^p}{\overset{k_c^p}{\rightleftharpoons}} T_m P_m, \tag{R8}$$

after which phosphate is released into the matrix with forward (k_3^p) and reverse (k_{-3}^p) rates. This step regenerates the free transporter (T_m) and completes the transport cycle:

$$T_m P_m \underset{k_{-3}^p}{\overset{k_3^p}{\rightleftharpoons}} T_m + P_m. \tag{R9}$$

This fully reversible cycle ensures thermodynamic consistency and allows heteroexchange, depending on substrate availability and gradient direction.

3.2 System of Ordinary Differential Equations (ODEs)

The dynamics of the transporter system are described by a set of ordinary differential equations (ODEs) that capture the temporal evolution of transporter states, substrate complexes, and metabolite concentrations. To distinguish between MM and IMS, we explicitly include their respective compartment volumes, V_m and V_{ims}, in the rate equations. This ensures that fluxes are appropriately scaled by compartment size and that concentration changes are proportional to the fluxes across compartments. We further assume mass conservation and a spatially homogeneous system, since on the timescales considered, diffusion within each compartment is much faster than the transport processes being modeled. The complete ODE system is provided in Appendix A.

3.3 Model Assumptions and Derivation of Rate Equations for the SLC25A10 Transporter

We assume that conformational changes of the transporter–substrate complexes (T_mS_m, T_mM_m, $T_{ims}S_{ims}$, $T_{ims}M_{ims}$, $T_{ims}P_{ims}$, T_mP_m) occur much faster than the binding and dissociation events of these complexes [1, 2, 36]. This separation of timescales allows conformational changes to be treated as effectively instantaneous, enabling us to combine the matrix-facing and IMS-facing transporter–substrate states into effective reactions (see Appendix B).

We further assume that the SLC25A10 transporter operates under a symmetric transport mechanism [33, 34, 35]. In this framework, the rate constants governing substrate binding, conformational transitions, and product release are taken to be equal in magnitude for transport in both directions. For example, in the case of succinate, the binding and release rates on the matrix side (k_1^s, k_{-1}^s) are assumed identical to the corresponding

rates on the IMS side (k^s_{-3}, k^s_3). The same symmetry applies to malate and phosphate. This assumption reduces the number of independent kinetic parameters, thereby simplifying parameter estimation, while also ensuring that the transporter satisfies microscopic reversibility and detailed balance at equilibrium. Under this symmetry, the complete system of ODEs can be further reduced to a compact form, provided in Appendix C.

We also apply the quasi–steady-state assumption (QSSA), which is widely used in enzyme kinetics [37, 38].The motivation for this assumption in our context is that conformational changes of the transporter are fast relative to substrate binding and dissociation events [1, 2, 36].On the timescales relevant for SLC25A10-mediated exchange, the intermediate transporter–substrate complexes (e.g., T_mS_m, T_mM_m, $T_{ims}P_{ims}$) therefore equilibrate rapidly, and their concentrations can be considered approximately constant. This simplification allows us to balance the rates of formation and breakdown of these complexes, leading to tractable flux equations for both forward and reverse cycles; the full mathematical derivation is provided in Appendix D for readers interested in the technical details.

Within this framework, the net flux contribution from succinate (J_{succ}) is:

$$J_{\text{succ}} = \frac{1}{V_m}\left[\frac{T^s_{\max}\left(\phi_2[S_{ims}] - [S_m]\right)}{K^s_m\delta_1 + K^s_m\phi_2\delta_2}\right] - \frac{1}{V_{ims}}\left[\frac{T^s_{\max}\left([S_m] - \phi_1[S_{ims}]\right)}{K^s_m\delta_1 + K^s_m\phi_1\delta_2}\right], \tag{2}$$

the net flux contribution from malate (J_{mal}) is:

$$J_{\text{mal}} = \frac{1}{V_m}\left[\frac{T^m_{\max}\left(\phi_2[M_{ims}] - [M_m]\right)}{K^m_m\delta_1 + K^m_m\phi_2\delta_2}\right] - \frac{1}{V_{ims}}\left[\frac{T^m_{\max}\left([M_m] - \phi_1[M_{ims}]\right)}{K^m_m\delta_1 + K^m_m\phi_1\delta_2}\right], \tag{3}$$

and the net flux contribution from phosphate (J_{pho}) is:

$$J_{\text{pho}} = \frac{1}{V_{ims}}\left[\frac{T^p_{\max}\left([P_m] - \phi_2[P_{ims}]\right)}{K^p_m\delta_1 + K^p_m\phi_2\delta_2}\right] - \frac{1}{V_m}\left[\frac{T^p_{\max}\left(\phi_1[P_{ims}] - [P_m]\right)}{K^p_m\delta_1 + K^p_m\phi_1\delta_2}\right]. \tag{4}$$

where

$$\phi_1 = \frac{\lambda_1[S_m] + \lambda_2[M_m] + \lambda_3[P_m]}{\lambda_1[S_{ims}] + \lambda_2[M_{ims}] + \lambda_3[P_{ims}]}, \tag{5}$$

$$\phi_2 = \frac{\lambda_1[S_m] + \lambda_2[M_m] + \left(\frac{V_m}{V_{ims}}\right)^2\lambda_3[P_m]}{\lambda_1[S_{ims}] + \lambda_2[M_{ims}] + \left(\frac{V_m}{V_{ims}}\right)^2\lambda_3[P_{ims}]}. \tag{6}$$

The dimensionless ratios ϕ_1 and ϕ_2 compare the weighted presence of substrates on the two sides of the membrane, thereby modulating the extent to which the matrix side pulls the transporter relative to the IMS side. Here, ϕ_1 represents the activity ratio from the matrix perspective, while ϕ_2 represents the activity ratio from the IMS perspective. The parameters λ_1, λ_2, and λ_3 are conformational bias weights assigned to succinate, malate, and phosphate, respectively. These quantify how strongly each substrate drives

the transporter through its conformational transition once bound. Specifically, λ_1 corresponds to succinate, λ_2 to malate, and λ_3 to phosphate. Biologically, these parameters capture the competitive influence of each substrate at the single binding site of SLC25A10, where succinate, malate, and phosphate compete for access. The λ-weights thus scale the contribution of each substrate to the conformational bias terms (ϕ_1, ϕ_2).

It is important to clarify that, in the SLC25A10 ping–pong mechanism, the transport cycle is reversible. Depending on the prevailing concentration gradients, the transporter can initiate the cycle from either the matrix or the IMS side, and with either a dicarboxylate (succinate or malate) or phosphate as the starting substrate. For instance, if the cycle begins with phosphate, it will be exchanged for a dicarboxylate; conversely, if it begins with a dicarboxylate, it will be exchanged for phosphate. The ratios ϕ_1 and ϕ_2, together with the weighting parameters $\lambda_1, \lambda_2, \lambda_3$, govern this directional choice by determining which substrate and which side of the membrane most strongly bias the initiation of the transport cycle.

The terms δ_1 and δ_2 are dimensionless partition functions that describe the availability of the transporter for binding on the matrix and IMS sides, respectively:

$$\delta_1 = 1 + \frac{[S_m]}{K_m^s} + \frac{[M_m]}{K_m^m} + \frac{[P_m]}{K_m^p}, \tag{7}$$

$$\delta_2 = 1 + \frac{[S_{ims}]}{K_m^s} + \frac{[M_{ims}]}{K_m^m} + \frac{[P_{ims}]}{K_m^p}. \tag{8}$$

These include contributions from all three substrates, ensuring that succinate, malate, and phosphate compete for the same single binding site on whichever side of the membrane is exposed. The "1" term corresponds to the unbound transporter, while each substrate term (e.g., $[X_m]/K_m^x$ for the matrix or $[X_{ims}]/K_m^x$ for the IMS) represents the relative occupancy weight contributed by substrate X. Here, K_m^s, K_m^m, and K_m^p are Michaelis constants (dissociation constants) representing the binding affinities of the respective substrates to the carrier.

Conceptually, δ_1 and δ_2 have the same form as classical binding polynomials used in enzyme kinetics [39]. Each δ represents the sum of all possible occupancy states on the matrix or IMS side. Dividing an individual term (e.g. $[S_m]/K_m^s$) by δ gives the probability that the transporter is bound by that substrate. This highlights that our model treats transporter occupancy analogously to enzyme–ligand binding, but extended here to the ping–pong transport mechanism.

Here, $T_{\max}^s$, $T_{\max}^m$, and $T_{\max}^p$ represent the apparent maximal transport capacities for succinate, malate, and phosphate, respectively. Each $T_{\max}$ has units of concentration per unit time and reflects the product of the number of active transporter molecules and the turnover rate per transporter under saturating substrate conditions. These values set the upper limit of flux for each transport mode in the absence of competitive inhibition or thermodynamic constraints. Differences among $T_{\max}$ values may arise from distinct translocation rates for each substrate or from asymmetries in binding and release kinetics across the two halves of the ping–pong cycle.

Since no leak pathways are considered and SLC25A10 is assumed to have a single binding site, each complete ping–pong cycle exchanges one dicarboxylate for one phosphate. At steady state, the flux through both half-cycles is therefore identical. Using the sign convention of our ODEs, J_{succ} and J_{mal} are positive when succinate or malate enter

the matrix, while J_{pho} is positive when phosphate enters the IMS (i.e., exits the matrix). Under this convention, the phosphate flux equals the total dicarboxylate flux:

$$J_{\text{pho}} = J_{\text{succ}} + J_{\text{mal}}. \tag{9}$$

Finally, the overall transport magnitude of the dicarboxylate carrier is expressed as:

$$J_{\text{tot}} = |J_{\text{succ}}| + |J_{\text{mal}}| + |J_{\text{pho}}|. \tag{10}$$

3.4 Reduced Model

Using the approximate flux expressions ($J_{\text{mal}}, J_{\text{succ}}, \text{and } J_{\text{pho}}$), the ODEs governing the system dynamics can be simplified to the following form:

$$\frac{dM_m}{dt} = J_{\text{mal}}, \tag{11.1}$$

$$\frac{dM_{ims}}{dt} = -J_{\text{mal}}, \tag{11.2}$$

$$\frac{dS_m}{dt} = J_{\text{succ}}, \tag{11.3}$$

$$\frac{dS_{ims}}{dt} = -J_{\text{succ}}, \tag{11.4}$$

$$\frac{dP_m}{dt} = -J_{\text{pho}}, \tag{11.5}$$

$$\frac{dP_{ims}}{dt} = J_{\text{pho}}. \tag{11.6}$$

Here, positive fluxes are defined as transport into the matrix, such that the corresponding IMS terms carry the opposite sign. This reduced model preserves mass balance across the membrane while capturing the essential dynamics of succinate, malate, and phosphate exchange through the SLC25A10 transporter.

Table 1: General Model Parameter Values

Parameter	**Value**	**Source**
Mitochondria matrix volume (V_m)	$1\mu L \times mg^{-1}$ mitochondria protein	Sadri et al. (2023)
Mitochondria IMS volume (V_{ims})	Assume to be 10% of V_m	Sadri et al. (2023)
Mitochondrial Phosphate concentration ($[P_m]$)	$10mM$	Sadri et al. (2023)
Mitochondrial Succinate concentration ($[S_m]$)	$10mM$	Sadri et al. (2023)
Mitochondrial Malate concentration ($[M_m]$)	$10mM$	Sadri et al. (2023)

3.5 Available Experimental Data

In this study, we calibrated our mechanistic model using three key datasets from the kinetic analysis of the dicarboxylate carrier in rat liver mitochondria reported by Palmieri et al. [3]. While the governing equations of our model are general to the ping–pong mechanism of SLC25A10, the specific parameter values estimated here are context-dependent

and reflect the rat liver system. Application to other tissues or species would therefore require reparameterization with appropriate experimental data.

The datasets used consist of succinate uptake rates measured over a range of external succinate concentrations, malate uptake rates measured over a range of external malate concentrations, and malate uptake rates measured over a range of external malate concentrations in the presence of 0.5 mM external succinate, which revealed competitive inhibition between malate and succinate for transport through the carrier.

In our model, the concentrations of succinate, malate, and phosphate in the IMS ($S_{ims}, M_{ims}, P_{ims}$) were set according to these datasets. The mitochondrial matrix concentrations of malate (M_m), succinate (S_m), and phosphate (P_m), together with the volumes of the mitochondrial matrix and the IMS, were fixed based on the experimental conditions and literature values (see Table 6).

3.6 Structural Parameter Identifiability Analysis

As the first step of model calibration [40], we analyzed whether the values of all model parameters can, in principle, be determined from perfect, continuous-time, noise-free measurements of the observables, based solely on the model structure and available measurements. Here, observables refer to model outputs that are experimentally measurable, in this case the net fluxes J_{succ}, J_{mal}, and J_{pho}. To this end, we performed a local structural identifiability analysis of the 9-parameter SLC25A10 ping–pong transport model using the STRIKE-GOLDD method [41]. For this analysis, we used the reduced ODE model.

3.7 Local Sensitivity Analysis

To estimate the local sensitivity coefficients (LSCs), we compute the partial derivative of the flux with respect to a given parameter θ. This describes how small perturbations in that parameter change the flux. Each parameter θ_i in $\tilde{\theta}$ was perturbed individually by a factor $\varepsilon = 0.01$ (a 1% change), while keeping all other parameters fixed. The partial derivative was approximated using the central finite difference:

$$\frac{\partial J}{\partial \theta_i} \approx \frac{J(\theta_i\,(1+\varepsilon)) - J(\theta_i\,(1-\varepsilon))}{2\,\varepsilon\,\theta_i}. \tag{11}$$

Since raw sensitivities depend on the units and magnitudes of both the flux and the parameter, they are not directly comparable across parameters. To address this, we use normalized LSCs. In this normalization, each sensitivity is scaled relative to both the corresponding parameter value and the flux value. The normalized LSC is then defined as:

$$\text{LSC}_i = \frac{\theta_i}{J}\frac{\partial J}{\partial \theta_i} \approx \frac{J(\theta_i\,(1+\varepsilon)) - J(\theta_i\,(1-\varepsilon))}{2\,\varepsilon\,J}. \tag{12}$$

This renders the coefficients dimensionless, allowing the influence of parameters with different units (e.g. maximum transport rates versus dissociation constants) to be compared on the same scale. Intuitively, the normalized LSC represents the percentage change in a flux that results from a one percent change in a given parameter.

3.8 Bayesian Framework for Parameter Estimation

To estimate the unknown parameters and quantify their uncertainties in the SLC25A10 transporter flux equations, we apply Bayesian inference using the Metropolis–Hastings Markov Chain Monte Carlo (MCMC) algorithm [42, 43]. The parameter vector $\tilde{\theta}$ is defined as

$$\tilde{\theta} = \left[T^s_{\max},\ \ T^m_{\max},\ \ K^s_m,\ \ K^m_m,\ \ K^p_m,\ \ \lambda_{21},\ \ \lambda_{31}\right]^{\mathsf{T}}$$

Phosphate flux is not independently parameterized, as it is constrained by the cyclic balance equation (9). Therefore, we do not include $T^p_{\max}$ in the parameter vector.

According to Bayes' theorem, the conditional probability of the parameter vector $\tilde{\theta}$ given the measured data Y, known as the posterior distribution, is expressed as:

$$p(\tilde{\theta} \mid Y) = \frac{p(Y \mid \tilde{\theta})\, p(\tilde{\theta})}{p(Y)} \tag{13}$$

where $p(\tilde{\theta})$ is the prior distribution of the unknown parameters, encoding available knowledge or plausible ranges before considering the experimental data. $p(Y \mid \tilde{\theta})$ is the likelihood function, describing the probability of observing the experimental data Y given a specific parameter set $\tilde{\theta}$. $p(Y)$ is the marginal likelihood (or evidence), acting as a normalizing constant ensuring $\int p(\tilde{\theta} \mid Y)\, d\tilde{\theta} = 1$. In practice, $p(Y)$ is difficult to compute directly, so inference is carried out up to a proportionality constant:

$$p(\tilde{\theta} \mid Y) \propto p(Y \mid \tilde{\theta})\, p(\tilde{\theta}). \tag{14}$$

3.8.1 Likelihood Function

The results of our SLC25A10 model are always subject to error because it is only an approximation of the underlying transport process. If we consider the experimental measurements, Y, as the observation of the transport fluxes, then the model predictions with parameters $\tilde{\theta}$, denoted $F(\tilde{\theta})$, can be expressed as

$$Y_i = F_i(\tilde{\theta}) + \varepsilon_i, \tag{15}$$

where ε_i represents the error in the model and i indexes the experimental data points. The error is assumed to follow an independent Gaussian distribution with zero mean and constant variance σ^2. Under these assumptions, the likelihood function for the data Y given the parameters $\tilde{\theta}$ and variance σ^2 can be written as

$$p(Y \mid \tilde{\theta}, \sigma^2) = \prod_{i=1}^{n} \frac{1}{\sqrt{2\pi\sigma^2}} \exp\left[-\frac{\left(Y_i - F_i(\tilde{\theta})\right)^2}{2\sigma^2}\right], \tag{16}$$

where n is the total number of flux measurements across all experiments.

Since the error variance σ^2 is unknown, it is treated as an additional parameter to be inferred jointly with $\tilde{\theta}$ in the Bayesian framework. From this point onward, we introduce the overall parameter vector $\tilde{\xi}$, defined as:

$$\tilde{\xi} = \left[\theta_1,\ \ \theta_2,\ \ \theta_3,\ \ \theta_4,\ \ \theta_5,\ \ \theta_6,\ \ \theta_7,\ \ \sigma^2\right]^{\mathsf{T}}, \tag{17}$$

To simplify our computations, we take the natural logarithm of the likelihood function. The log-likelihood is then proportional to the sum of squared residuals between the measured and model-predicted fluxes:

$$\begin{aligned}\ln p(Y \mid \tilde{\xi}) &= \sum_{i=1}^{n} \left[-\frac{1}{2}\ln(2\pi\sigma^2) - \frac{(Y_i - F_i(\tilde{\theta}))^2}{2\sigma^2} \right] \\ &= -\frac{n}{2}\ln(2\pi\sigma^2) - \frac{1}{2\sigma^2}\sum_{i=1}^{n}(Y_i - F_i(\tilde{\theta}))^2 \end{aligned} \tag{18}$$

We emphasise that our assumption of independent, identically distributed Gaussian errors is not intended to fully capture the complexity of experimental uncertainty or model–data discrepancy. Instead, we regard this as a proof of concept choice that enables a tractable Bayesian calibration of a mechanistic model grounded in real physiological dynamics. The Gaussian assumption allows for closed form likelihoods and efficient computation, which is essential at this stage.

3.8.2 Prior

The prior distributions of the unknown parameters $\tilde{\xi}$ were assigned based on the results of the structural identifiability analysis and available experimental data.

The structural identifiability analysis indicated that $T^s_{\max}$, $T^m_{\max}$, K^s_m, K^m_m, and K^p_m are structurally unidentifiable. To address this, we adopted their values from the literature, as summarized in Table 2. For these parameters, we assigned Gaussian priors with means and standard deviations set to the reported experimental estimates, thereby constraining them to physiologically realistic ranges while allowing for uncertainty:

$$\tilde{\xi}_i \sim \mathcal{N}(\mu_{\tilde{\xi}_i}, \tau^2_{\tilde{\xi}_i}), \quad i = 1, 2, 3, 4, 5, \tag{19}$$

with probability density function:

$$p(\tilde{\xi}_i) = \frac{1}{\sqrt{2\pi\tau^2_{\tilde{\xi}_i}}} \exp\left(-\frac{(\tilde{\xi}_i - \mu_{\tilde{\xi}_i})^2}{2\tau^2_{\tilde{\xi}_i}} \right). \tag{20}$$

The parameters λ_{21} and λ_{31} were found to be structurally identifiable. We therefore assigned them independent uniform priors over a wide positive range, with lower bound l and upper bound u, reflecting the absence of strong prior constraints:

$$\tilde{\xi}_i \sim \mathcal{U}(l,\, u), \quad i = 6, 7, \tag{21}$$

with probability density function:

$$p(\tilde{\xi}_i) = \frac{1}{u - l}, \quad \tilde{\xi}_i \in [l, u]. \tag{22}$$

The observation error variance σ^2 was assigned an inverse-gamma prior with shape parameter α and scale parameter β:

$$\tilde{\xi}_i \sim \text{Inv-Gamma}(\alpha,\, \beta), \quad i = 8, \tag{23}$$

with probability density function:

$$p(\tilde{\xi}_i) = \frac{\beta^\alpha}{\Gamma(\alpha)} (\tilde{\xi}_i^2)^{-\alpha-1} \exp\left(-\frac{\beta}{\tilde{\xi}_i^2}\right), \quad \tilde{\xi}_i^2 > 0. \tag{24}$$

Assuming a priori independence, the joint prior distribution factorizes as:

$$p(\tilde{\xi}) = \prod_{i=1}^{8} p(\tilde{\xi}_i), \tag{25}$$

with each term defined according to the distributional choices described above. To ensure positivity and simplify computations, we used the logarithm of the prior distribution:

$$\ln p(\tilde{\xi}) = \sum_{i=1}^{8} \ln p(\tilde{\xi}_i). \tag{26}$$

Table 2: Literature values of kinetic parameters with mean, standard deviation, 95% confidence intervals, and references.

Parameter	**Mean**	**Std**	**95% CI (Low–High)**	**Reference**
K_m^s (mM)	1.17	0.10	0.97 – 1.37	[3]
K_m^m (mM)	0.23	0.02	0.19 – 0.27	[3]
K_m^p (mM)	0.93	0.40	0.13 – 1.73	[44, 17]
$T_{\max}^s$ (μmol/min/g)	64.2	5.1	54.0 – 74.4	[3]
$T_{\max}^m$ (μmol/min/g)	69.4	5.6	58.4 – 80.6	[3]

3.8.3 Posterior Distribution

Given the likelihood function $p(Y \mid \tilde{\xi})$ in Eq. (**??**) and the independent priors $p(\tilde{\xi})$ defined in Eq. (25), the posterior distribution of the parameter vector is obtained using Bayes' theorem (Eq. (14)).

For computational convenience and to ensure positivity, we work with the logarithm of the posterior distribution. Combining Eq. (18) and Eq. (26), the log-posterior can be written as:

$$\ln p(\tilde{\xi} \mid Y) \propto \ln p(\tilde{\xi}) + \ln p(Y \mid \tilde{\xi}). \tag{27}$$

3.8.4 Markov Chain Monte Carlo (MCMC) Method

Direct analytical evaluation of the posterior distribution $p(\tilde{\xi} \,|\, Y)$ is generally intractable due to the complexity of the nonlinear transporter model. Therefore, we employed a Markov Chain Monte Carlo (MCMC) approach to generate samples from the posterior distribution and estimate the kinetic parameters [42].

We used the Metropolis–Hastings algorithm to construct the Markov chain $\{\tilde{\xi}^{(j)} : j = 0, 1, 2, \dots\}$, where j denotes the sampling iteration. At each iteration j, a new candidate $\tilde{\xi}^*$ was generated using a log-normal random walk proposal:

$$\ln \tilde{\xi}^* = \ln \tilde{\xi}^{(j)} + z\eta, \quad \eta \sim \mathcal{N}(0, 1), \tag{28}$$

which ensures positivity of all parameters. Here, z is the step size, set to $z = 0.01$ in our calculations.

The acceptance probability is given by:

$$\alpha\Big(\tilde{\xi}^{(j)}, \tilde{\xi}^{*}\Big) = \min\left[1, \frac{p(Y \mid \tilde{\xi}^{*})\, p(\tilde{\xi}^{*})\, q(\tilde{\xi}^{(j)} \mid \tilde{\xi}^{*})}{p(Y \mid \tilde{\xi}^{(j)})\, p(\tilde{\xi}^{(j)})\, q(\tilde{\xi}^{*} \mid \tilde{\xi}^{(j)})}\right], \tag{29}$$

where $q(\cdot|\cdot)$ denotes the log-normal proposal density. Since the log-normal proposal distribution is asymmetric, the Hastings correction (the ratio of proposal densities) is included to guarantee detailed balance and ensure that the posterior distribution remains the stationary distribution of the chain [43].

If $\alpha \geq r$, where $r \sim \mathcal{U}(0, 1)$, the candidate is accepted:

$$\tilde{\xi}^{(j+1)} = \tilde{\xi}^{*}, \tag{30}$$

otherwise, the current state is retained:

$$\tilde{\xi}^{(j+1)} = \tilde{\xi}^{(j)}. \tag{31}$$

At each iteration, the fluxes J_{succ}, J_{mal}, and J_{pho} were computed using the transporter flux equations. We used all three dataset wihc we adopted form [3] whicho describe above. These datasets together comprise $n = 18$ data points and were used as the observation vector Y.

3.8.5 Estimation of Monte Carlo Standard Error (MCSE)

After generating a sequence of samples from the posterior distribution using the Metropolis–Hastings MCMC algorithm, we used these samples to estimate posterior quantities such as the mean, median, and credible intervals. However, because the number of samples is finite and they are often correlated due to the Markov chain structure;each sample depends on the previous one [45, 46, 47, 48], these estimates have some variability. The MCSE quantifies the error in an MCMC estimate (e.g. the posterior mean) that arises from sampling variability.

To calculate the MCSE of a kinetic parameter of interest θ_i from a chain of N samples, we first compute the sample mean:

$$\hat{\theta} = \frac{1}{N} \sum_{i=1}^{N} \theta_i. \tag{32}$$

We then compute the sample variance of the MCMC samples:

$$\Sigma^2 = \frac{1}{N-1} \sum_{i=1}^{N} (\theta_i - \hat{\theta})^2, \tag{33}$$

which represents the variability of the parameter values in the chain.

Since MCMC samples are correlated, the effective sample size (N_{eff}) is typically smaller than N. To estimate N_{eff}, we compute the autocorrelation at lag k, denoted ρ_k, using the autocorrelation function (ACF) [45]:

$$\rho_k \approx \frac{\sum_{i=1}^{N-k}(\theta_i - \hat{\theta})(\theta_{i+k} - \hat{\theta})}{\sum_{i=1}^{N}(\theta_i - \hat{\theta})^2}. \tag{34}$$

The effective sample size is then estimated as:

$$N_{\text{eff}} = \frac{N}{1 + 2\sum_{k=1}^{\infty} \rho_k}. \tag{35}$$

In practice, the sum is truncated at a lag where ρ_k becomes negligible [48].

Finally, the MCSE for the posterior mean is given by:

$$\text{MCSE} = \sqrt{\frac{\Sigma^2}{N_{\text{eff}}}}.$$

This formula accounts for correlation among the MCMC samples. A small MCSE indicates that the MCMC estimate is precise, meaning that the chain length is sufficient to approximate the true posterior statistic. In this study, we aimed for an MCSE smaller than 10% of the posterior standard deviation (Σ), which reflects the intrinsic uncertainty of the parameter under the posterior distribution. While we cannot guarantee the correctness of the finite set of N samples, by calculating the MCSE-to-SD ratio and targeting values below 0.10, we empirically assessed the convergence and reliability of the chains.

3.8.6 Estimation of $\hat{R}$ Statistic

To assess the convergence of our chains to the equilibrium or stationary distribution, we estimate the Gelman–Rubin statistic, $\hat{R}$ [49, 50]. This diagnostic evaluates whether independently initialized chains target the same stationary posterior. It does so by comparing between-chain to within-chain variability for each parameter.

Suppose there are Ω chains, each with N draws for a parameter θ. Let the draws from chain $\omega \in \Omega$ be denoted $\theta_{\omega,i}$, where i indexes the samples. The chain mean for chain ω is

$$\hat{\theta}_\omega = \frac{1}{N}\sum_{i=1}^{N} \theta_{\omega,i}. \tag{36}$$

The overall mean across all chains is

$$\bar{\theta} = \frac{1}{\Omega}\sum_{\omega=1}^{\Omega} \hat{\theta}_\omega. \tag{37}$$

The between-chain variance is

$$B = \frac{N}{\Omega - 1}\sum_{\omega=1}^{\Omega} \left(\hat{\theta}_\omega - \bar{\theta}\right)^2. \tag{38}$$

The within-chain variance for each chain is

$$\Sigma_\omega^2 = \frac{1}{N-1} \sum_{i=1}^{N} \left(\theta_{\omega,i} - \hat{\theta}_\omega \right)^2, \tag{39}$$

and the average within-chain variance is

$$W = \frac{1}{\Omega} \sum_{\omega=1}^{\Omega} \Sigma_\omega^2. \tag{40}$$

The pooled variance estimator is defined as

$$\Psi = \frac{N-1}{N} W + \frac{1}{N} B, \tag{41}$$

and the Gelman–Rubin statistic is then computed as

$$\hat{R} = \sqrt{\frac{\Psi}{W}}. \tag{42}$$

In practice, values of $\hat{R} \approx 1$ (e.g., < 1.1) indicate acceptable convergence, whereas $\hat{R} > 1.1$ suggests potential convergence issues [49]. In this study, we require $\hat{R} < 1.1$ for all parameters.

3.9 Gibbs Free Energy Calculations for SLC25A10 Antiporter

The Gibbs free energy change (ΔG) for the electroneutral antiport process mediated by the SLC25A10 transporter, which exchanges dicarboxylates (succinate or malate) with phosphate across the mitochondrial membrane, is calculated for the following reactions:

$$\begin{aligned} \mathrm{S}_{\mathrm{m}}^{2-} + \mathrm{P}_{\mathrm{ims}}^{2-} &\rightleftharpoons \mathrm{S}_{\mathrm{ims}}^{2-} + \mathrm{P}_{\mathrm{m}}^{2-}, \\ \mathrm{M}_{\mathrm{m}}^{2-} + \mathrm{P}_{\mathrm{ims}}^{2-} &\rightleftharpoons \mathrm{M}_{\mathrm{ims}}^{2-} + \mathrm{P}_{\mathrm{m}}^{2-}, \end{aligned}$$

following the methodology of Jol et al. (2010) [51]. The general Gibbs free energy equation for transport processes is:

$$\begin{aligned} \Delta G = &\sum_j W_j \Delta_f G_j^0 + RT \sum_j W_j \ln C_j + \sum_{i \in \text{transported}} w_i \Delta_f G_i^0 \\ &+ \sum_{i \in \text{transported}} s_i N_{H,i} \left(\Delta_f G_{\mathrm{H}^+,i}^0 + RT \ln[\mathrm{H}^+]_i \right) \\ &+ RT \sum_{i \in \text{transported}} w_i \ln C_{j,i} + F \Delta\varphi_m \sum_{i \in \text{inside}} w_i \zeta_i \end{aligned} \tag{43}$$

where w_i are the stoichiometric coefficients for the transported species, with values of -1 for substrates in the matrix and $+1$ for products in the intermembrane space. W_j

are the stoichiometric coefficients of reactants j, defined as the sum of the coefficients of all species participating in the reaction. The term $\Delta_f G_j^0$ denotes the transformed Gibbs energy of formation for species j, adjusted for pH to reflect mitochondrial conditions. C_j represents species concentrations in their respective compartments. For transported species i, $\Delta_f G_i^0$ is the Gibbs energy of formation, and $C_{j,i}$ is the concentration of the reactant pool containing species i. R is the gas constant, T is the absolute temperature, F is the Faraday constant, and $\Delta\varphi_m$ is the membrane potential.

For the SLC25A10 antiporter, the process is electroneutral, with both transported species (succinate or malate and phosphate) carrying a -2 charge. Thus, no net charge is moved across the membrane, and the electrochemical potential term ($F\Delta\varphi_m \sum_{i\in\text{inside}} w_i\zeta_i$) is zero. In addition, we assume no protons are co-transported ($N_{H,i} = 0$), so the proton-related term vanishes. Since the standard Gibbs free energies of formation of substrates and products are identical (they are the same chemical species in different compartments), these terms cancel in pairs and the contribution from W_j is zero. Consequently, the Gibbs free energy equation simplifies to:

$$\Delta G = \sum_{i\in\text{transported}} w_i \Delta_f G_i^0 + RT \sum_{i\in\text{transported}} w_i \ln C_{j,i}. \tag{44}$$

For succinate exchange, this becomes:

$$\begin{aligned}\Delta G = &\left(\Delta_f G^\circ_{\mathrm{S}_{ims}} + \Delta_f G^\circ_{\mathrm{P}_m} - \Delta_f G^\circ_{\mathrm{S}_m} - \Delta_f G^\circ_{\mathrm{P}_{ims}}\right) \\ &+ RT\left(\ln C_{\mathrm{S}_{ims}} + \ln C_{\mathrm{P}_m} - \ln C_{\mathrm{S}_m} - \ln C_{\mathrm{P}_{ims}}\right).\end{aligned} \tag{45}$$

Using our notation, with $[S_m], [S_{ims}], [P_m], [P_{ims}]$ in place of concentrations C, we write:

$$\Delta G = \left(\Delta_f G^\circ_{\mathrm{S}_{ims}} + \Delta_f G^\circ_{\mathrm{P}_m} - \Delta_f G^\circ_{\mathrm{S}_m} - \Delta_f G^\circ_{\mathrm{P}_{ims}}\right) + RT \ln\left(\frac{[S_{ims}]\,[P_m]}{[S_m]\,[P_{ims}]}\right). \tag{46}$$

Similarly, for malate exchange:

$$\Delta G = \left(\Delta_f G^\circ_{\mathrm{M}_{ims}} + \Delta_f G^\circ_{\mathrm{P}_m} - \Delta_f G^\circ_{\mathrm{M}_m} - \Delta_f G^\circ_{\mathrm{P}_{ims}}\right) + RT \ln\left(\frac{[M_{ims}]\,[P_m]}{[M_m]\,[P_{ims}]}\right). \tag{47}$$

Table 3: Thermodynamic parameters and constants for Gibbs free energy calculations of SLC25A10 antiport reactions.

Species / Constant	**Charge (z)**	**$\Delta_f G^\circ$ (kJ/mol)**	**Stoichiometry (s_i)**	**Reference**
Malate (IMS)	-2	-842.66	$+1$	[17, 52]
Malate (Matrix)	-2	-842.66	-1	[17, 52]
Succinate (IMS)	-2	-690.44	$+1$	[51, 52]
Succinate (Matrix)	-2	-690.44	-1	[51, 52]
Phosphate (IMS)	-2	-1069.1	-1	[51, 52]
Phosphate (Matrix)	-2	-1069.1	$+1$	[51, 52]
Gas Constant (R)	–	0.008314 kJ/K	–	[51]
Temperature (T)	–	298.15 K (25 °C)	–	[51]

At thermodynamic equilibrium, $\Delta G = 0$, giving:

$$\frac{[S_{ims}^{eq}]\,[P_m^{eq}]}{[S_m^{eq}]\,[P_{ims}^{eq}]} = K_{eq}, \tag{48}$$

where

$$K_{eq} = \exp\left(-\frac{\Delta_f G^\circ_{rxn}}{RT}\right), \tag{49}$$

and

$$\Delta_f G^\circ_{rxn} = \Delta_f G^\circ_{\mathrm{M}_{ims}} + \Delta_f G^\circ_{\mathrm{P}_m} - \Delta_f G^\circ_{\mathrm{M}_m} - \Delta_f G^\circ_{\mathrm{P}_{ims}} \tag{50}$$

is the standard Gibbs free energy change of the reaction. Since the species are chemically identical across compartments, $\Delta_f G^\circ_{rxn}$ is close to zero, and the equilibrium distribution is dominated by the concentration ratios.

From conservation of mass in each metabolite pool, the analytical equilibrium concentrations can be written as explicit functions of initial metabolite concentrations. The full derivation is given in Appendix H. The resulting closed-form equilibrium concentrations are:

$$S_m^{eq} = \frac{([S_m^0] + [S_{ims}^0])\,([S_m^0] + [P_{ims}^0])}{[S_m^0] + [S_{ims}^0] + [P_m^0] + [P_{ims}^0]}, \tag{51}$$

$$S_{ims}^{eq} = \frac{([S_m^0] + [S_{ims}^0])\,([P_m^0] + [S_{ims}^0])}{[S_m^0] + [S_{ims}^0] + [P_m^0] + [P_{ims}^0]}, \tag{52}$$

$$P_m^{eq} = \frac{([S_m^0] + [P_{ims}^0])\,([P_m^0] + [S_{ims}^0])}{[S_m^0] + [S_{ims}^0] + [P_m^0] + [P_{ims}^0]}, \tag{53}$$

$$P_{ims}^{eq} = \frac{([S_m^0] + [S_{ims}^0])\,([P_m^0] + [P_{ims}^0])}{[S_m^0] + [S_{ims}^0] + [P_m^0] + [P_{ims}^0]}. \tag{54}$$

These closed-form expressions allow direct analytical validation of the simulated equilibrium state of the reduced transporter model against thermodynamic constraints.

3.10 Simulating the Effect of Succinate Accumulation in the Mitochondrial Matrix on the Dynamics of the SLC25A10 Transporter

To simulate succinate accumulation, we incorporated a source and a sink into our transporter model. Specifically, we added the flux of succinyl-CoA synthetase (SCAS) as a source of succinate and the flux of succinate dehydrogenase (SDH) as a sink for succinate.

SDH is a mitochondrial enzyme that functions in both the tricarboxylic acid (TCA) cycle and the electron transport chain (ETC). It catalyzes the oxidation of succinate to fumarate (F_m) while reducing ubiquinone (Q_m) to ubiquinol ($QH_{2,m}$). This reaction depletes the mitochondrial succinate pool, thereby affecting the fluxes and dynamic behavior of the SLC25A10 transporter, which exchanges succinate with phosphate. The electron transfer reactions catalyzed by SDH (Complex II) are:

$$\mathrm{S}_m + \mathrm{FAD}_m \rightleftharpoons \mathrm{F}_m + \mathrm{FADH}_{2,m} \tag{R10}$$

$$\mathrm{FADH}_{2,m} + \mathrm{Q}_m \rightleftharpoons \mathrm{FAD}_m + \mathrm{QH}_{2,m} \tag{R11}$$

which can be lumped into a single overall reaction:

$$\mathrm{S}_m + \mathrm{Q}_m \rightleftharpoons \mathrm{F}_m + \mathrm{QH}_{2,m}, \tag{R12}$$

where S_m denotes mitochondrial succinate, F_m fumarate, Q_m ubiquinone, and $QH_{2,m}$ ubiquinol. The flux of this reaction, J_{SDH}, was adopted from Sadri et al. [17]. The complete flux equation, parameter values, and assumptions are provided in Appendix Appendix E.

SCAS is another enzyme of the TCA cycle that catalyzes the reversible conversion of succinyl-CoA into succinate. This reaction simultaneously produces a nucleoside triphosphate (typically GTP) from mitochondrial phosphate (P_m) and GDP, thereby increasing mitochondrial succinate levels while depleting phosphate:

$$\text{Succinyl-CoA}_m + \text{GDP}_m + \text{P}_m \rightleftharpoons \text{S}_m + \text{GTP}_m + \text{CoA}_m + \text{H}_m^+. \tag{R13}$$

The flux of this enzyme, J_{SCAS}, was also taken from Sadri et al. [17]; full details are provided in Appendix F.

We integrated these fluxes into the dynamic equations governing the SLC25A10 transporter: J_{SDH} was included as a sink (negative term) and J_{SCAS} as a source (positive term). High SDH activity results in rapid succinate depletion, whereas high SCAS activity leads to succinate accumulation and phosphate consumption.

We simulated two scenarios: SDH-active (normal mitochondria), where succinate is oxidized by SDH, and SDH-deficient, where SDH is knockdown. The modified reduced ODE system for the SDH-active condition is:

$$\frac{dM_m}{dt} = J_{\text{mal}}, \tag{50.1}$$

$$\frac{dM_{ims}}{dt} = -J_{\text{mal}}, \tag{50.2}$$

$$\frac{dS_m}{dt} = J_{\text{succ}} - J_{\text{SDH}} + J_{\text{SCAS}}, \tag{50.3}$$

$$\frac{dS_{ims}}{dt} = -J_{\text{succ}}, \tag{50.4}$$

$$\frac{dP_m}{dt} = -J_{\text{pho}} - J_{\text{SCAS}}, \tag{50.5}$$

$$\frac{dP_{ims}}{dt} = J_{\text{pho}}. \tag{50.6}$$

For the SDH-deficient case, we set $J_{\text{SDH}} = 0$.

4 Results

4.1 Structural Identifiability Analysis of the SLC25A10 Transporter Model

The local structural identifiability analysis indicates that the system is not fully observable and that not all parameters are structurally identifiable under the current model formulation and output configuration. Two main structural reasons explain this loss of identifiability are: Scaling symmetries between $T^x_{\max}$ and K^x_m, for x substrate and Relative nature of λ_1, λ_2, and λ_3 parameters.

In each flux equation, $T^x_{\max}$ and K^x_m appear together as the ratio $T^x_{\max}/K^x_m$ because the denominator is of the form $K^x_m(\delta_1 + \phi\,\delta_2)$. Multiplying $T^x_{\max}$ by a constant factor

and K_m^x by the same factor leaves the flux unchanged, making them inseparable without additional constraints or data.

In the ϕ_1 and ϕ_2 expressions, the λ values act only as proportional weights on succinate, malate, and phosphate concentrations. Scaling all λ values by a common constant leaves both ϕ_1 and ϕ_2 unchanged. As a result, the absolute values of λ_1, λ_2, and λ_3 cannot be uniquely determined—only their ratios, and thus the relative weighting between substrates, are structurally identifiable.

To address the symmetry in the λ parameters, we reparameterized the model by introducing the ratios $\lambda_{21} = \lambda_2/\lambda_1$ and $\lambda_{31} = \lambda_3/\lambda_1$ as new parameters, replacing λ_1, λ_2, and λ_3 in the ϕ terms. These ratios represent relative weightings of malate (λ_2) and phosphate (λ_3) with respect to succinate (λ_1) in determining the transporter's conformational bias terms (ϕ_1, ϕ_2).

A second STRIKE-GOLDD analysis of the reparameterized model showed that λ_{21} and λ_{31} became structurally identifiable. However, the transport capacities $T_{\max}^x$ and the Michaelis constants K_m^x for each substrate remained structurally unidentifiable due to their appearance only as ratios $T_{\max}^x/K_m^x$ in the flux equations.

To fully resolve the identifiability issue, we adopted literature values for $T_{\max}^x$ and K_m^x for succinate and malate from Palmieri et al. [3] and for phosphate from Indiveri et al. [44] and Sadri et al. [17]. This parameter fixing removed the scaling symmetry between $T_{\max}^x$ and K_m^x, rendering the remaining free parameters structurally identifiable in the STRIKE-GOLDD analysis.

4.2 Local Sensitivity Analysis

Following the structural identifiability analysis and reparameterization of the model, we investigated how the kinetic parameters influence the dynamics of the SLC25A10 transporter. To this end, we computed normalized local sensitivity coefficients (LSCs) for three key output fluxes: succinate (J_{succ}), malate (J_{mal}), and phosphate (J_{pho}). Positive values indicate that an increase in the parameter enhances the flux, while negative values indicate suppression.

The analysis was performed on the reparameterized transporter model with seven kinetic parameters: the maximum transport rates for succinate ($T_{\max}^s$) and malate ($T_{\max}^m$); the dissociation constants for succinate (K_m^s), malate (K_m^m), and phosphate (K_m^p); and the coupling ratios λ_{21} and λ_{31}. For phosphate, we applied the cyclic balance constraint from Eq. (9), so no independent phosphate transport capacity was included.

Parameter values were initialized according to Table 1. Intermembrane space (IMS) metabolite concentrations were set to match the experimental data of Palmieri et al. [3], specifically the third dataset measuring malate uptake in the presence of 0.5 mM external succinate. This condition provides a direct test of competitive inhibition. Here, the IMS malate concentration was fixed at 0.9077 mM, external succinate at 0.5 mM, and other conditions matched the experimental setup.

Figure 3 shows the normalized LSCs for J_{succ}, J_{mal}, and J_{pho} under these competitive conditions. his normalization makes the coefficients dimensionless and comparable across parameters with different units and magnitudes. For succinate flux, λ_{31} exhibits the strongest positive influence, indicating that phosphate–succinate coupling is the dominant driver when IMS malate is fixed. The maximal succinate transport rate $T_{\max}^s$ also has a substantial positive effect, reflecting the direct role of transport capacity. By contrast, λ_{21}

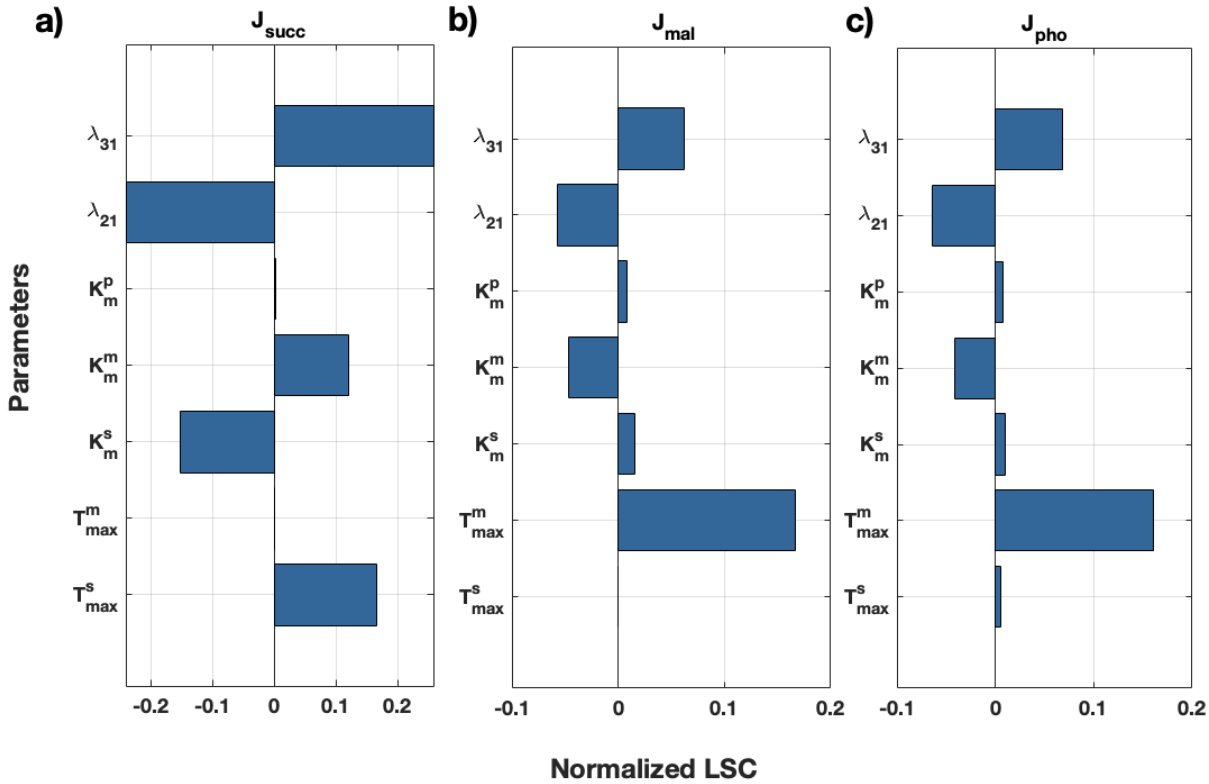

Figure 3: Normalized Local sensitivity coefficients (LSCs) for (a) succinate flux J_{succ}, (b) malate flux J_{mal}, and (c) phosphate flux J_{pho} with respect to model parameters. Here, "normalized" means that each sensitivity is scaled relative to both the value of the parameter and the corresponding flux, making the coefficients dimensionless. This allows the influence of parameters with different units and magnitudes to be compared on the same scale. Positive values indicate that increasing a parameter increases the fluxes, whereas negative values imply the opposite.

shows a negative sensitivity, implying that stronger malate coupling suppresses succinate turnover through competition. The Michaelis constant K_m^s has a small negative effect, consistent with increased affinity improving transport. Thus, succinate flux is primarily governed by phosphate coupling and intrinsic capacity, with malate coupling acting as a suppressor.

For malate flux, T_{max}^m is the dominant parameter, strongly and positively controlling flux. This shows that malate uptake is limited by its transport capacity rather than competition in this regime. λ_{31} exerts a weaker positive effect, while K_m^m contributes a moderate negative effect, indicating improved transport with higher malate affinity. Other parameters play negligible roles. Hence, malate flux is mainly determined by its own transport kinetics, suggesting saturation as the primary limiting factor.

For phosphate flux, T_{max}^m again emerges as the principal driver, reflecting the mechanistic coupling between phosphate efflux and malate influx in the ping–pong cycle. λ_{31} remains positively influential but with reduced magnitude compared to the succinate case. Other parameters have little effect. Thus, phosphate transport is primarily governed by malate dynamics, with coupling parameters exerting only secondary influence.

4.3 Bayesian Parameter Estimation

Following the structural identifiability and local sensitivity analyses, we employed a Bayesian inference framework to quantitatively estimate the kinetic parameters and assess the uncertainty of the SLC25A10 transporter model. The model was then validated against experimental flux data.

We ran 100,000 Metropolis Hastings MCMC iterations, discarding the first 2,000 as burn-in to reduce dependence on the initial guess. Posterior means, standard deviations, modes, and 95% credible intervals were computed from the retained samples for all parameters, including σ^2. A statistical summary of the estimated kinetic parameters is presented in Table 4.

For convergence diagnostics, we ran four independent MCMC chains initialized from dispersed starting values, each for 100,000 iterations with the first 2,000 discarded as burn-in. For each parameter, we computed the split-$\hat{R}$ statistic using the post–burn-in draws across chains. All parameters were achieved $\hat{R} < 1.1$ (Table 5), indicating good mixing and agreement between the variances within and between chains, and thus providing strong evidence of convergence to a common stationary posterior. The Metropolis–Hastings transition kernel used in our sampler satisfies a detailed balance with respect to the posterior target by construction; the small $\hat{R}$ values confirm that the chains reached this stationary regime in practice.

Table 4: Statistical summary of estimated parameters with units (where applicable) and their 95% credible intervals.

Parameter	**Mean**	**Median**	**Mode**	**Std**	**95% Credible Interval**	
					Low	**High**
$T^s_{\max}$ (μmol/min/g)	68.114	68.008	67.858	3.4163	61.794	75.065
$T^m_{\max}$ (μmol/min/g)	61.795	59.811	60.748	6.7289	52.777	75.94
K^s_m (mM)	1.1389	1.1377	1.1340	0.074369	0.99842	1.2872
K^m_m (mM)	0.23122	0.23109	0.23009	0.016133	0.20041	0.26303
K^p_m (mM)	0.91577	0.91178	0.90201	0.11189	0.70476	1.1392
λ_{21}	5.0303	3.2860	1.3373	4.9702	0.72787	18.141
λ_{31}	0.63160	0.62641	0.63160	0.24360	0.20378	1.1658
σ^2	2.3836	1.8947	1.6721	1.5863	1.0919	8.2493

The effective sample sizes (N_{eff}) ranged from 490 to 700, indicating that the chains provided several hundred effectively independent samples per parameter. The Monte Carlo standard errors (MCSEs) were small relative to the posterior standard deviations (Σ), with MCSE/Σ ratios between 0.053 and 0.144. Most parameters satisfied the conventional benchmark of MCSE/$\Sigma < 0.10$, suggesting that sampling variability contributed negligibly to posterior uncertainty. Exceptions were $T^m_{\max}$ (0.134), λ_{21} (0.141), λ_{31} (0.131), and σ^2 (0.136), which stabilized slightly above the 0.10 threshold. This behavior reflects posterior correlations and limited information in the experimental data rather than poor mixing, as evidenced by the $\hat{R}$ values, which were all close to 1.0 (≤ 1.03), confirming satisfactory convergence. Overall, the diagnostics indicate that the posterior estimates are reliable, although the relatively high MCSE/Σ for some parameters highlights directions where data constraints limit identifiability.

Figure 4 shows the MCMC traces and posterior distributions for the coupling ratios λ_{21}

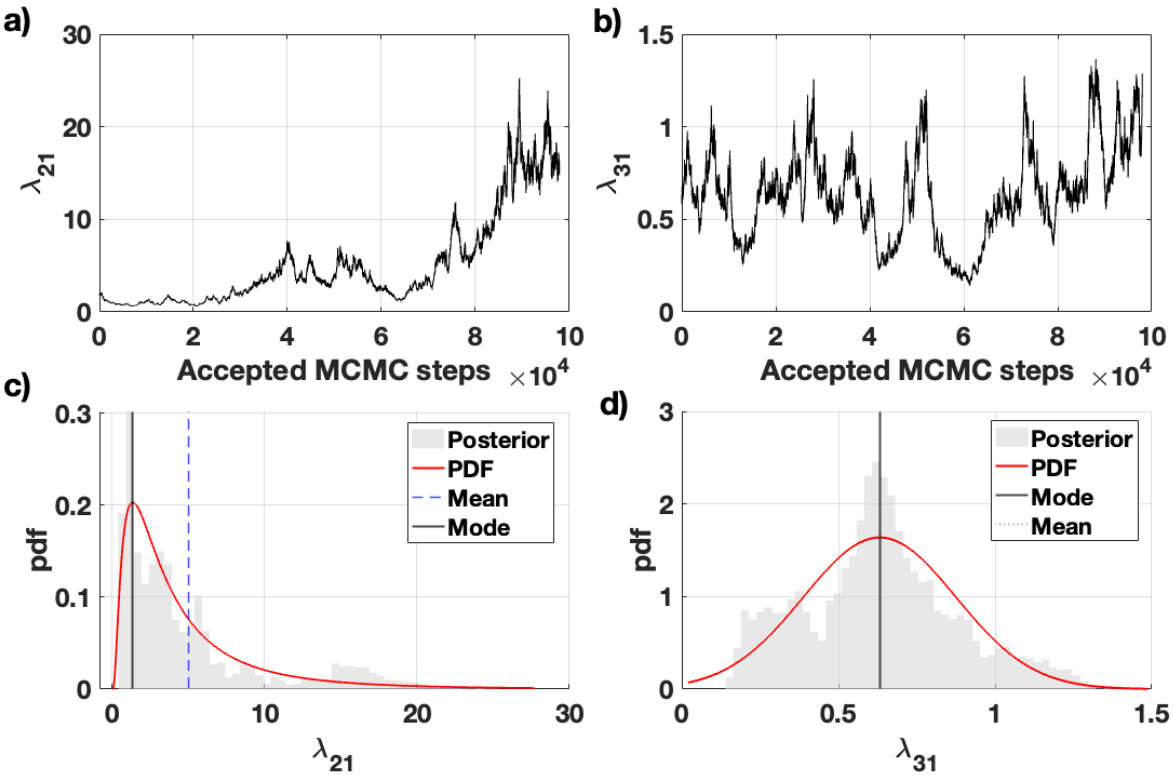

Figure 4: MCMC results for coupling parameters. (a,b) Trace plots for λ_{21} and λ_{31} across accepted iterations. (c,d) Posterior densities with kernel density estimates (red), posterior mode (solid line), and mean (dashed line).

Table 5: MCMC diagnostics per parameter, with respecto to total draws (N); burn-in draws (N_{burn}); effective sample size (N_{eff}); Monte Carlo standard error (MCSE); posterior standard deviation (Σ); relative Monte Carlo error (MCSE/Σ); $\hat{R}$.

Parameter	N	N_{burn}	N_{eff}	**MCSE**	Σ	**MCSE**/Σ	$\hat{R}$
$T^s_{\max}$	100000	2000	700	0.2280	3.4163	0.067	1.0011
$T^m_{\max}$	100000	2000	503	0.9044	6.7289	0.134	1.0183
K^s_m	100000	2000	662	0.0040	0.0744	0.053	1.0001
K^m_m	100000	2000	647	0.0011	0.0161	0.068	1.0015
K^p_m	100000	2000	542	0.0098	0.1119	0.088	1.0008
λ_{21}	100000	2000	490	0.6997	4.9702	0.141	1.0183
λ_{31}	100000	2000	495	0.0320	0.2436	0.131	1.0323
σ^2	100000	2000	491	0.2164	1.5863	0.136	1.0010

and λ_{31}. The posterior analysis of these parameters revealed distinct but complementary features of transporter binding dynamics. For λ_{21}, which captures the relative influence of malate versus succinate, the chains explored a wide range of values, and the trace did not collapse into a narrow band, suggesting that multiple parameter regimes are consistent with the data (Fig. 4a). The posterior distribution is highly skewed to the right, with a sharp peak near zero (mode) but a long tail extending to higher values (Fig. 4c). The mean is pulled upward by the long tail, while the mode is 1.3371 (Table 4). This indicates weak identifiability and uncertainty about whether malate or succinate dominates, with the posterior supporting both succinate-favored ($\lambda_{21} < 1$) and malate-favored ($\lambda_{21} > 1$)

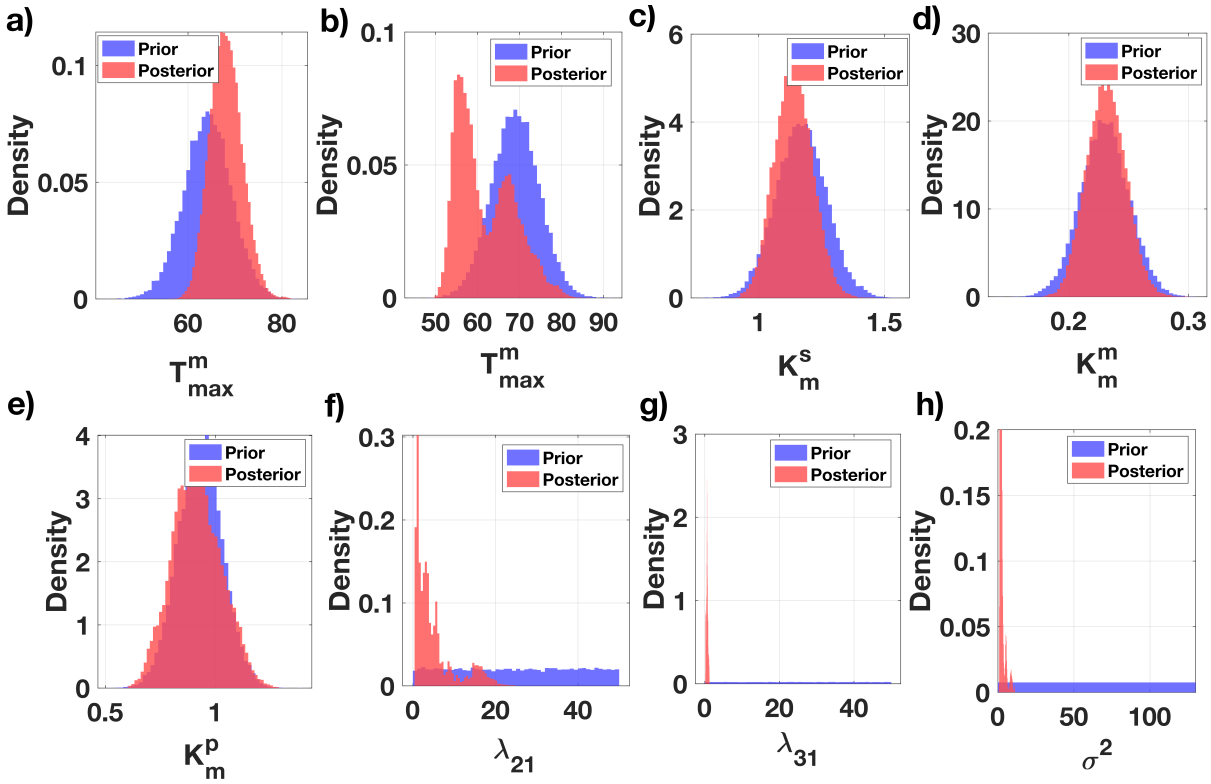

Figure 5: Comparison of posterior distributions with prior distributions for all model parameters of the SLC25A10 transporter. (a–b) show the posterior distributions (red) of transport capacities $T^s_{\max}$ and $T^m_{\max}$, which are significantly constrained relative to their priors (blue). (c–e) display the posterior distributions of substrate affinity constants (K^s_m, K^m_m, K^p_m). (f–g) illustrate the coupling parameters λ_{21} (malate/succinate coupling) and λ_{31} (phosphate/succinate coupling).

regimes. Biologically, this implies a finely balanced competition in which the transporter may shift between succinate- and malate-dominated states depending on cellular context and local metabolite availability.

In contrast, the posterior of λ_{31}, which represents the relative influence of phosphate versus succinate, showed an approximately symmetric distribution centered at 0.6316, where mean and mode overlapped. The MCMC trace supported this, with the chain fluctuating within a narrower range ($\sim$ 0.3–1.2), indicating tighter constraints and better identifiability compared to λ_{21} (Fig. 4b,d). This suggests phosphate is a consistent competitor with succinate, exerting moderate but stable influence. From a biological perspective, this balance highlights the central role of phosphate exchange in the carrier's ping–pong mechanism, ensuring effective competition with dicarboxylates while maintaining exchange stoichiometry.

Figure 5 compares prior and posterior distributions for the seven free parameters of the SLC25A10 model and error variance. For the transport capacities $T^s_{\max}$ (Fig. 5a), the wide Gaussian priors collapsed into narrower posterior distributions, indicating that the experimental data strongly constrain the maximal transport rates of succinate. However, multimodality appeared in the posterior distribution of $T^m_{\max}$ (Fig. 5b), arising because the experimental data are not strong enough to uniquely identify a single optimal value of this parameter. The Michaelis constants for succinate (Fig. 5c), malate (Fig. 5d), and phosphate (Fig. 5e) also showed substantial posterior narrowing, confirming that the

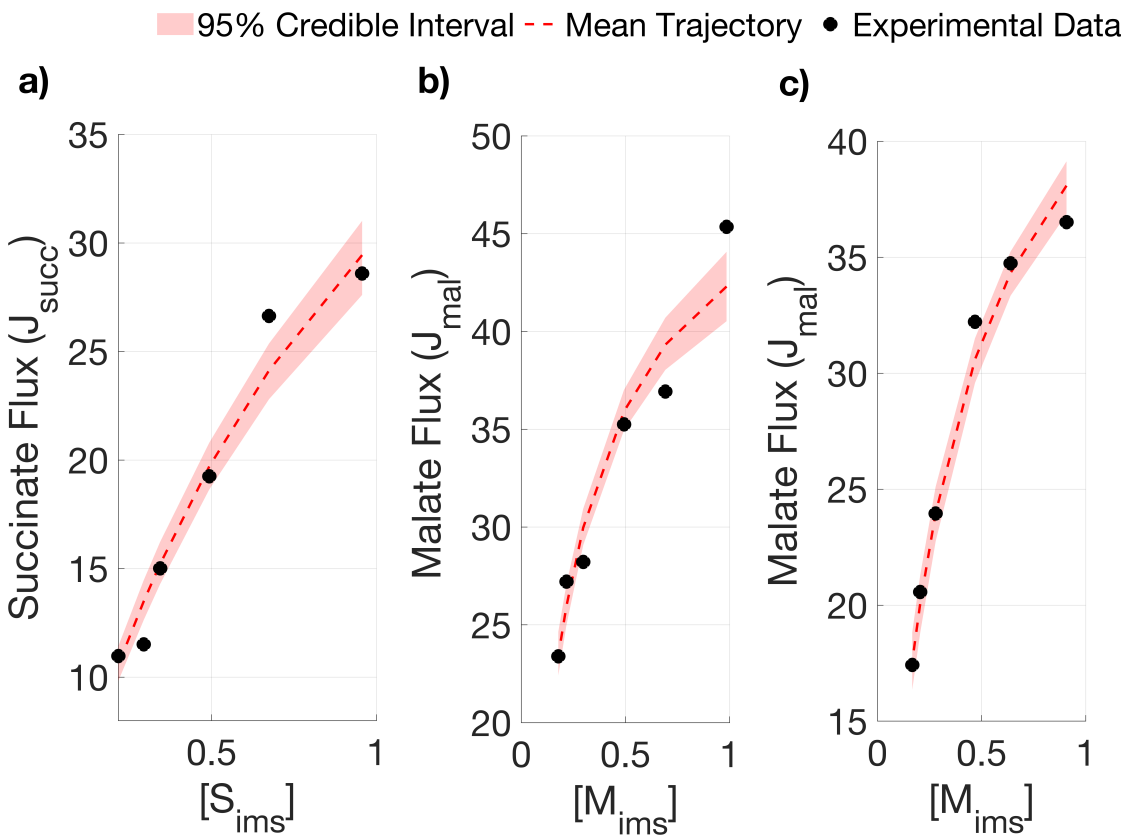

Figure 6: Model validation using isolated mitochondrial transport data. Experimental flux measurements (black dots) and Bayesian model fits (posterior mean: dashed line; 95% credible interval: shaded region) for three experimental datasets: (a) succinate uptake (J_{succ}) with varying $[S_{ims}]$, phosphate and malate set to zero; (b) malate uptake (J_{mal}) with varying $[M_{ims}]$ under non-competitive conditions (no succinate or phosphate in buffer); and (c) malate uptake (J_{mal}) with varying $[M_{ims}]$ under competitive conditions (0.5 mM succinate present, phosphate still zero).

binding affinities of dicarboxylates and phosphate are well informed by the competition assays.

The posterior distribution of error variance (σ^2) collapsed toward very low values compared to the prior, suggesting that the model explains most of the experimental variation (Fig. 5h). Biologically, this means the mechanistic framework captures the key dynamics of SLC25A10 with minimal unexplained noise.

Figure 6 compares model predictions based on posterior samples with the experimental flux measurements. For succinate flux J_{succ} (Fig. 6a), the posterior predictions closely follow the experimental uptake curve as a function of external succinate concentration. All experimental data points fall within the 95% credible band, demonstrating that the Bayesian-calibrated model reliably captures succinate transport dynamics. For malate flux J_{mal} without succinate competition (Fig. 6b), the predicted mean trajectory reproduces the experimental trend across the tested concentration range. Although one data point lies slightly above the credible interval, the overall agreement indicates that malate affinity and transport capacity are well captured. For malate flux J_{mal} in the presence of 0.5 mM external succinate (Fig. 6c), the posterior predictions accurately replicate the reduction in flux due to competitive inhibition. The close match validates the reparameterized coupling ratios λ_{21} and λ_{31}, showing that the ping–pong model framework

quantitatively accounts for substrate competition.

Together, these results confirm that the Bayesian-calibrated model reproduces both succinate and malate flux kinetics and correctly incorporates competitive inhibition, providing a mechanistically and statistically consistent representation of SLC25A10 transport dynamics.

4.4 Thermodynamic Validation of the Kinetic Model

To ensure that the SLC25A10 model is not only mathematically consistent but also thermodynamically sound, we validated it by analyzing flux trajectories, Gibbs free energy dissipation, and equilibrium metabolite concentrations under defined initial conditions.

Figure 7 demonstrates that the model satisfies the thermodynamic constraints and correctly predicts equilibrium partitioning between compartments. The exchange nature of the transporter is confirmed by the opposite behavior of J_{succ} and J_{pho}, which decay symmetrically to zero at steady state (Fig. 7a). The Gibbs free energy change, ΔG, decreases rapidly and asymptotically approaches zero, consistent with the second law of thermodynamics (Fig. 7b). The system therefore begins with a positive driving force and dissipates free energy until equilibrium is reached ($\Delta G = 0$).

Simulated metabolite concentrations at equilibrium matched closely with the analytically predicted equilibrium concentrations derived from the reduced single-variable formulation (Fig. 7c–f). This agreement further confirms the thermodynamic correctness of the model and its suitability for equilibrium-based analysis of mitochondrial transport dynamics.

These results demonstrate that SLC25A10 operates as an electroneutral antiporter, exchanging succinate and phosphate in a strictly coupled manner. The decay of fluxes and free energy to equilibrium reflects the reversible, thermodynamically constrained nature of the transporter. The equilibration patterns highlight the carrier's physiological role in maintaining dicarboxylate–phosphate balance across the inner mitochondrial membrane, which is essential for both TCA cycle function and phosphate availability for ATP synthesis.

4.5 Our model reveals the non-equilibrium dynamics of the dicarboxylate carrier (SLC25A10), shedding light on behaviors that are experimentally challenging

To investigate the dynamic behavior of the SLC25A10 transporter under experimentally realistic conditions, we simulated a competitive transport scenario analogous to the classical malate–succinate uptake experiments of Palmieri et al. [3]. The system was initialized with 0.91 mM malate, 0.5 mM succinate, and no phosphate in the IMS, while the mitochondrial matrix contained 10 mM of each metabolite (Table 1). The volumes of the matrix and IMS were set according to Table 1. These conditions mimic isolated mitochondrial uptake assays but allow us to resolve rapid transients that are experimentally inaccessible due to the sub-second timescale of equilibration and the technical difficulty of measuring subcellular metabolite gradients in real time.

Figure 8 shows the time evolution of metabolite concentrations and their gradients across the mitochondrial inner membrane. Matrix malate (M_m) increased rapidly (Fig. 8a),

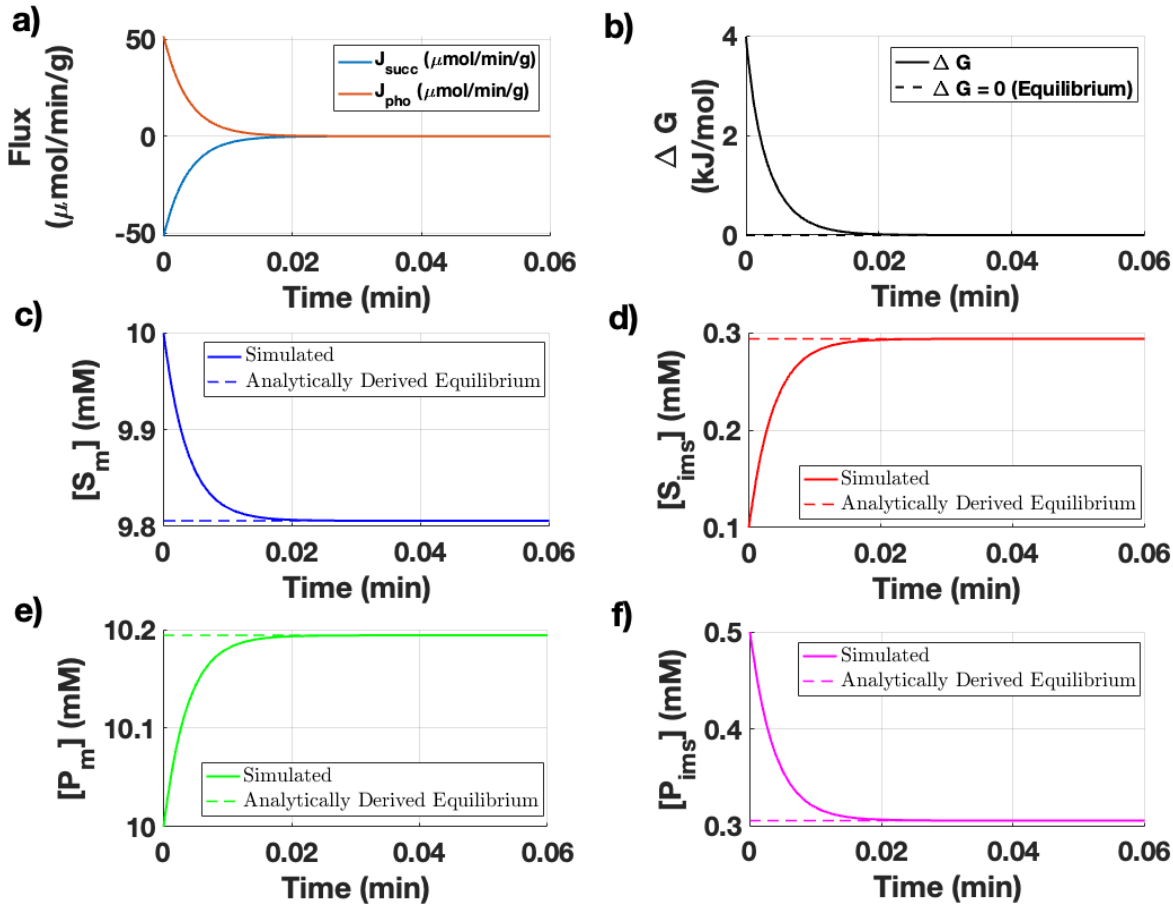

Figure 7: Thermodynamic analysis and equilibrium validation of the SLC25A10 antiport model. (a) Time-dependent fluxes of succinate (J_{succ}) and phosphate (J_{pho}) illustrate the electroneutral antiport mechanism and convergence to steady state. (b) Time-resolved Gibbs free energy change (ΔG) for the reaction $\mathrm{S}_m^{2-} + \mathrm{P}_{\text{ims}}^{2-} \rightleftharpoons \mathrm{S}_{\text{ims}}^{2-} + \mathrm{P}_m^{2-}$. (c–f) Simulated concentrations of succinate and phosphate in the mitochondrial matrix (MM) and intermembrane space (IMS) compared with analytically derived equilibrium expressions (dashed lines), obtained from the reduced single-variable formulation. Initial conditions: $[S_{\text{ims}}] = 0.1\,\text{mM}$, $[P_{\text{ims}}] = 0.5\,\text{mM}$, with malate initially set to zero in both compartments. Parameter values for $T^s_{\max}$, $T^m_{\max}$, K^s_m, K^m_m, and K^p_m correspond to posterior means, while λ_{21} and λ_{31} are fixed at their posterior modes from Table 4.

while IMS malate (M_{ims}) decreased correspondingly (Fig. 8b), establishing a steep and rising malate concentration gradient (Fig. 8c). A similar but less pronounced pattern was observed for succinate: matrix succinate (S_m) increased slightly (Fig. 8d), while IMS succinate (S_{ims}) decreased (Fig. 8e), producing a gradually increasing succinate gradient (Fig. 8f). In contrast, phosphate displayed the opposite behavior: matrix phosphate (P_m) decreased (Fig. 8g), while IMS phosphate (P_{ims}) increased (Fig. 8h), leading to a steeply declining phosphate gradient (Fig. 8i).

The corresponding flux trajectories (Fig. 9) reveal the mechanistic basis of these concentration changes. Initially, malate flux (J_{mal}) was strongly positive, indicating rapid import into the matrix (Fig. 9a). In parallel, phosphate flux (J_{pho}) was strongly negative, reflecting efflux into the IMS, while succinate flux (J_{succ}) showed only a modest positive influx. Over time, all fluxes decayed toward zero as the concentration gradients equilibrated. The total transport activity (Fig. 9b) peaked at approximately 400 μmol/min/g immediately after gradient imposition, then rapidly declined within milliseconds, consis-

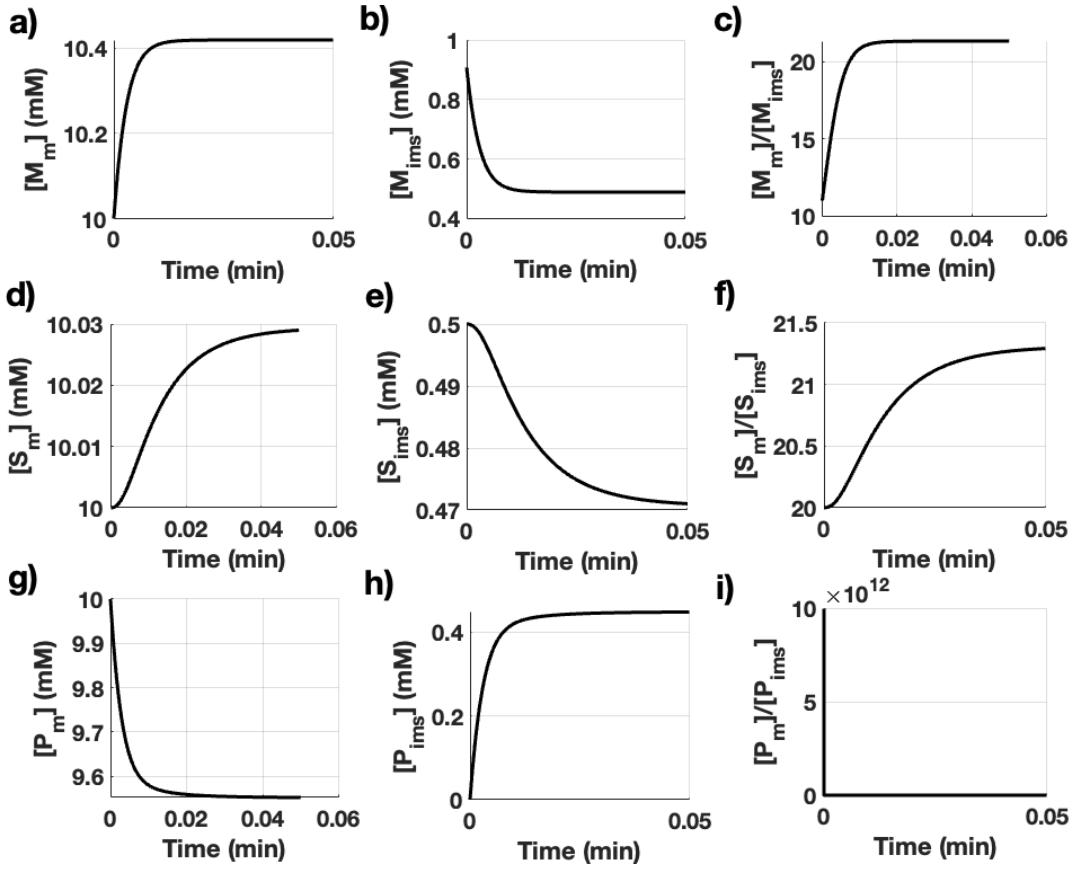

Figure 8: Time-dependent concentration and gradient dynamics of the SLC25A10 transporter under experimental-like conditions. (a–b) Malate concentrations in the MM and IMS; (c) malate concentration gradient. (d–e) Succinate concentrations in the MM and IMS; (f) succinate concentration gradient. (g–h) Phosphate concentrations in the MM and IMS; (i) phosphate concentration gradient. Initial IMS concentrations: 0.91 mM malate, 0.5 mM succinate, and no phosphate. The MM contained 10 mM of each metabolite. Parameter values for $T^s_{\max}$, $T^m_{\max}$, K^s_m, K^m_m, and K^p_m correspond to posterior means, while λ_{21} and λ_{31} are fixed at their posterior modes (Table 4).

tent with a transient burst of exchange activity.

Together, these simulations highlight the transient and gradient-driven nature of SLC25A10 transport. The transporter harnesses phosphate gradients to drive malate and succinate import, thereby supplying reducing equivalents and TCA intermediates to the mitochondrial matrix for oxidative phosphorylation [5, 4]. In parallel, phosphate efflux ensures electroneutrality and sustains antiport cycling. Notably, succinate import was secondary to malate transport during the early phase, reflecting both competitive binding and the displacement dynamics of the ping–pong mechanism. As the phosphate gradient collapsed, transport activity diminished, demonstrating that SLC25A10 acts primarily as a rapid buffering system rather than a sustained flux provider under steady-state conditions. This implies that phosphate is the main thermodynamic driver of the bidirectional transport cycle. Overall, these non-equilibrium dynamics reveal how SLC25A10 coordinates dicarboxylate exchange with phosphate efflux, enabling mitochondria to adapt rapidly to changes in substrate supply during metabolic stress or experimental perturbations.

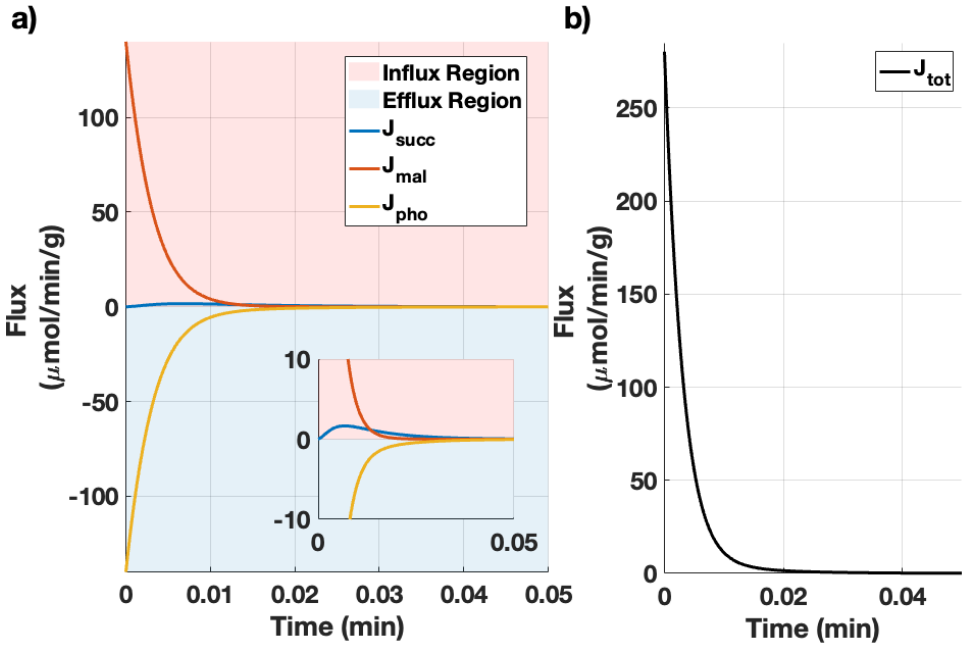

Figure 9: Time-dependent fluxes of the SLC25A10 transporter under experimental-like conditions. (a) Individual fluxes for malate (J_{mal}), succinate (J_{succ}), and phosphate (J_{pho}). Shaded regions denote influx (blue) and efflux (red). (b) Total transport activity defined as $J_{\text{tot}} = |J_{\text{succ}}| + |J_{\text{mal}}| + |J_{\text{pho}}|$. Initial IMS concentrations: 0.91 mM malate, 0.5 mM succinate, and no phosphate. The MM contained 10 mM of each metabolite. Parameter values for T^s_{max}, T^m_{max}, K^s_m, K^m_m, and K^p_m correspond to posterior means, while λ_{21} and λ_{31} are fixed at their posterior modes (Table 4).

4.6 Effect of Mitochondrial Morphology on Initial SLC25A10 Fluxes

To quantify how mitochondrial morphology modulates dicarboxylate exchange, we investigated the sensitivity of initial SLC25A10 fluxes to compartment volumes in two complementary swelling scenarios: IMS swelling with a fixed matrix volume, and matrix swelling with the IMS fixed at 10% of the matrix volume. For each condition, we recorded the initial fluxes of succinate (J_{succ}), malate (J_{mal}), phosphate (J_{pho}), and the magnitude of the total transport activity (J_{tot}) (Fig. 10).

Figure 10 shows that increasing V_{ims} monotonically decreased the initial magnitudes of malate and phosphate exchange fluxes, while succinate flux behaved differently. The initial succinate flux (J_{succ}) remained negative across all conditions, indicating persistent efflux from the matrix into the IMS. Interestingly, this efflux exhibited a biphasic response: as IMS volume increased, J_{succ} first became less negative (weaker efflux), reflecting a temporary dampening or reduction in the effective strength of the succinate gradient, before declining again as substrate dilution reduced the driving force. In contrast, initial J_{mal} declined monotonically, and the phosphate counter-flux (J_{pho}) became less negative, indicating weaker export. The aggregate outcome was a marked reduction in J_{tot} with increasing V_{ims}, consistent with slower initial carrier turnover when the IMS is swollen. This behavior is expected, as IMS swelling dilutes extramitochondrial substrate pools and reduces the transmembrane concentration gradients that drive antiport.

In the second scenario, expanding the matrix volume also dampened the initial exchange rates (Figs. 10a–d). The primary mechanism is dilution of matrix-side substrates,

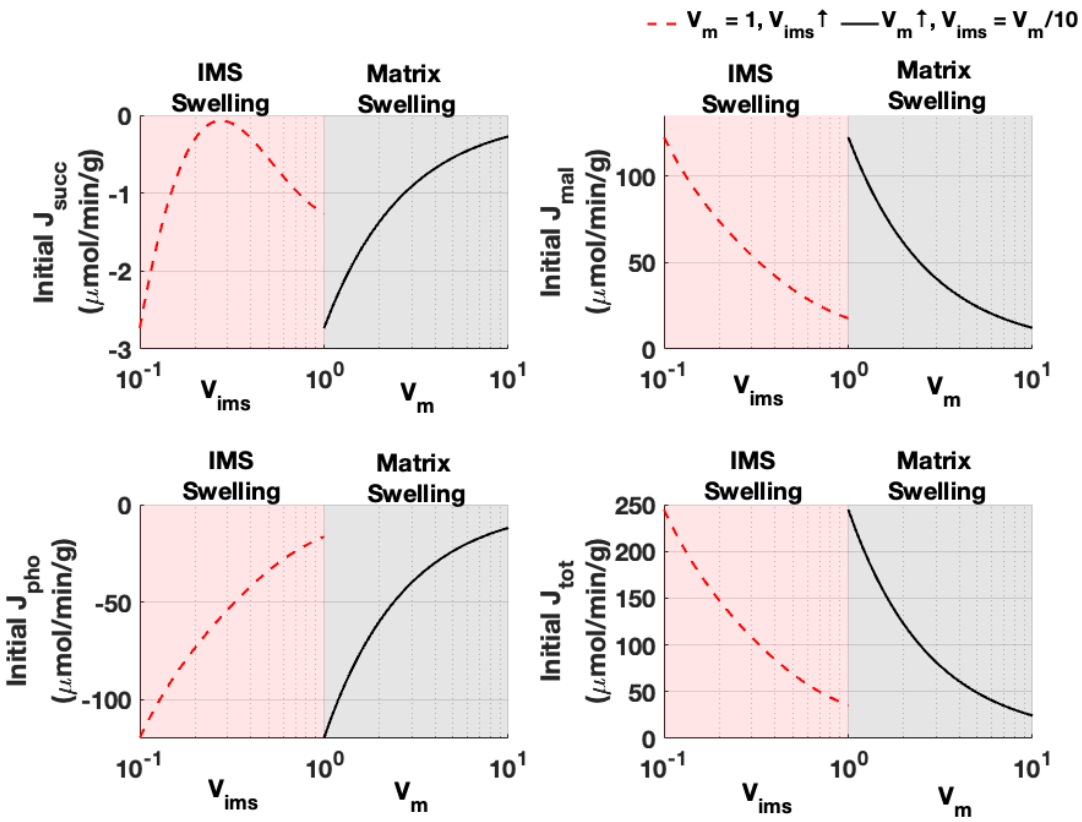

Figure 10: Effect of IMS and Matrix Swelling on Initial SLC25A10 Fluxes. Changes in the initial flux of (a) J_{succ}, (b) J_{mal}, (c) J_{pho}, and (d) total transport activity (J_{tot}) under IMS swelling (red), where $V_m = 1\ \mu\text{L}\,\text{mg}^{-1}$ is fixed while V_{ims} is varied (log-scale), and matrix swelling (grey), where $V_{\text{ims}} = V_m/10$ while V_m is varied (log-scale). Simulations were initialized with IMS concentrations of 0.91 mM malate, 0.5 mM succinate, and 0.1 mM phosphate, and 10 mM of each metabolite in the matrix. Parameter values for T^s_{max}, T^m_{max}, K^s_m, K^m_m, and K^p_m correspond to posterior means, while λ_{21} and λ_{31} are fixed at their posterior modes (Table 4).

which lowers the matrix-to-IMS concentration gradient and shifts the system into a more unsaturated regime. Although the intrinsic dissociation constants (K^s_m, K^m_m, K^p_m) remain unchanged, this dilution effectively increases the apparent dissociation constants, thereby reducing the transporter's effective affinity for substrates. As a result, initial J_{succ} and J_{mal} decline monotonically with increasing V_m, while J_{pho} becomes less negative. The combined outcome is a reduction in initial J_{tot}, demonstrating that matrix swelling slows the onset of exchange even when the IMS expands proportionally.

Across both scenarios, the trends are monotonic and substantial over a tenfold change in volume. Malate flux shows the largest absolute drop at small volumes, reflecting its higher absolute initial rate under the competitive assay conditions. Phosphate export also weakens as either compartment swells, consistent with its role as the counter-exchanged anion. These results suggest that mitochondrial swelling—whether in the IMS or the matrix—attenuates the initial transport capacity of SLC25A10 by diminishing the effective driving forces for exchange. This finding aligns with biophysical expectations: larger compartments buffer concentration changes and impose dilution penalties on transport-mediated fluxes [25, 26, 27, 28, 29]. Physiologically, mild, transient volume adjustments may fine-tune exchange rates, whereas pronounced swelling (e.g., during os-

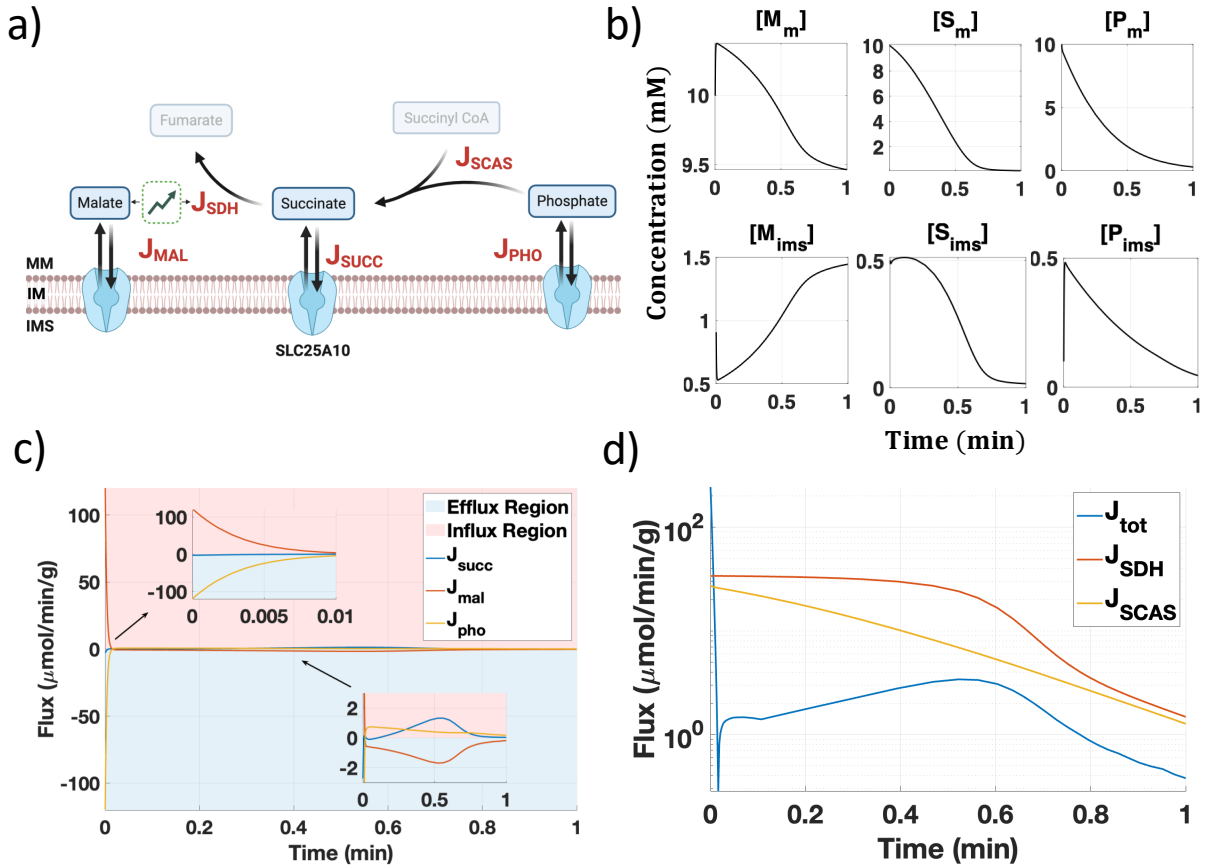

Figure 11: Metabolic integration of SLC25A10 with succinate dehydrogenase (SDH) and succinyl-CoA synthetase (SCAS). (a) Schematic of the SLC25A10-mediated antiport system coupled to SDH (succinate oxidation) and SCAS (succinate production). (b) Time-dependent metabolite concentrations in the mitochondrial matrix (MM, top) and intermembrane space (IMS, bottom). (c) Dynamic fluxes through the dicarboxylate carrier ($J_{\text{succ}}, J_{\text{mal}}, J_{\text{pho}}$). (d) Comparison of total transporter activity (J_{tot}) with enzymatic fluxes from SDH (J_{SDH}) and SCAS (J_{SCAS}). Simulations were initialized with IMS concentrations of 0.91 mM malate, 0.5 mM succinate, and 0.1 mM phosphate, and 10 mM of each metabolite in the matrix. Parameter values for $T^s_{\max}$, $T^m_{\max}$, K^s_m, K^m_m, and K^p_m correspond to posterior means, while λ_{21} and λ_{31} are fixed at their posterior modes (Table 4).

motic stress or early reperfusion) could blunt dicarboxylate/phosphate exchange and slow the re-establishment of steady-state metabolite distributions.

4.7 Succinate accumulation drives SLC25A10-mediated transport dynamics under SDH deficiency

Succinate is a key intermediate of the TCA cycle; however, excessive accumulation in the mitochondrial matrix is associated with multiple pathophysiological states, including cancer and metabolic disorders [5]. Within the matrix, succinate levels are tightly regulated by two enzymes: succinyl-CoA synthetase (SCAS), which generates succinate, and succinate dehydrogenase (SDH), which consumes it [15, 16, 17, 39]. Inactivating mutations in SDH impair succinate oxidation and lead to pathological succinate buildup [53, 54, 39, 5]. A central question is how the dicarboxylate carrier SLC25A10 responds under these SDH-deficient conditions, when the normal metabolic sink is absent.

To address this, we extended our transporter model to include SDH and SCAS reactions, which act as the enzymatic sink and source of matrix succinate, respectively (Fig. 11a). This integration enabled direct comparison of SDH-active and SDH-deficient conditions, thereby isolating the effects of succinate accumulation on SLC25A10-mediated dynamics.

Figure 11 shows how coupling to SDH and SCAS reshapes transport behavior. In the SDH-active case, matrix succinate (S_m) decreased monotonically as SDH consumed it, while S_{ims} also fell as SLC25A10 attempted to replenish the matrix pool. Matrix malate initially rose as in the uncoupled case (Fig. 8), but subsequently declined once SDH consumption outpaced transporter-mediated import. Correspondingly, IMS malate decreased sharply at first (due to uptake) but later rebounded, reflecting a switch from transporter-driven import to SDH-driven depletion (Fig. 11d). Phosphate dynamics followed a similar biphasic pattern: initial efflux was followed by re-import as SCAS activity sustained a net phosphate demand in the matrix (Fig. 11b). These behaviors reveal two distinct regimes: (i) an early burst phase dominated by transporter-driven import, and (ii) a longer-term phase where enzymatic reactions (SDH, SCAS) govern metabolite levels.

Figure 12 compares SDH-active and SDH-deficient mitochondria. In the absence of SDH, succinate accumulated steadily in the matrix, reaching nearly twice the concentration observed under SDH-active conditions (Fig. 12b). As the succinate gradient exceeded those of malate and phosphate, SLC25A10 switched to mediating net succinate export into the IMS, coupled to malate and phosphate import (Fig. 12a,c). This behavior is physiologically logical: malate import replenishes the TCA cycle, which is blocked at SDH; without fumarate production, matrix malate cannot be sustained, making cytosolic replenishment essential. Likewise, phosphate import supports SCAS activity and succinyl-CoA cycling. Thus, in SDH-deficient mitochondria, SLC25A10 effectively rewires its role from a malate importer to a succinate exporter.

Flux profiles confirmed these trajectories (Fig. 12g–i). Malate (J_{mal}) and phosphate (J_{pho}) fluxes decayed rapidly under both conditions, indicating their transient and gradient-driven nature. Succinate flux (J_{succ}), however, showed striking differences: with SDH active, succinate import peaked around 0.5 min before returning to equilibrium (Fig. 12h), whereas in SDH-deficient mitochondria, J_{succ} shifted into sustained efflux. In the absence of a metabolic sink, succinate was exported down its concentration gradient, with SLC25A10 coupling this efflux to malate and phosphate uptake.

These results demonstrate that SLC25A10 plays a dual role depending on SDH activity. In healthy mitochondria, SDH consumes succinate, and SLC25A10 primarily supports malate import with transient succinate uptake. In SDH-deficient mitochondria, succinate accumulates in the matrix, and SLC25A10 switches to exporting succinate in exchange for malate and phosphate. This rewiring represents a compensatory mechanism: succinate efflux relieves matrix overload while simultaneously importing metabolites needed to sustain residual TCA cycling and SCAS activity. Importantly, this phenomenon aligns with observations in SDH-deficient tumors, where succinate acts as an oncometabolite driving pseudohypoxia, HIF stabilization, and epigenetic dysregulation [53, 5]. Once exported to the IMS, succinate can diffuse into the cytoplasm, where it inhibits prolyl hydroxylases (PHDs) and stabilizes hypoxia-inducible factor-1α (HIF-1α), initiating transcription of hypoxia-responsive genes [12, 13, 55, 14]. This metabolic adaptation underlies the pseudohypoxic phenotype characteristic of SDH-deficient chromaffin cells and tumors, such as paragangliomas and pheochromocytomas.

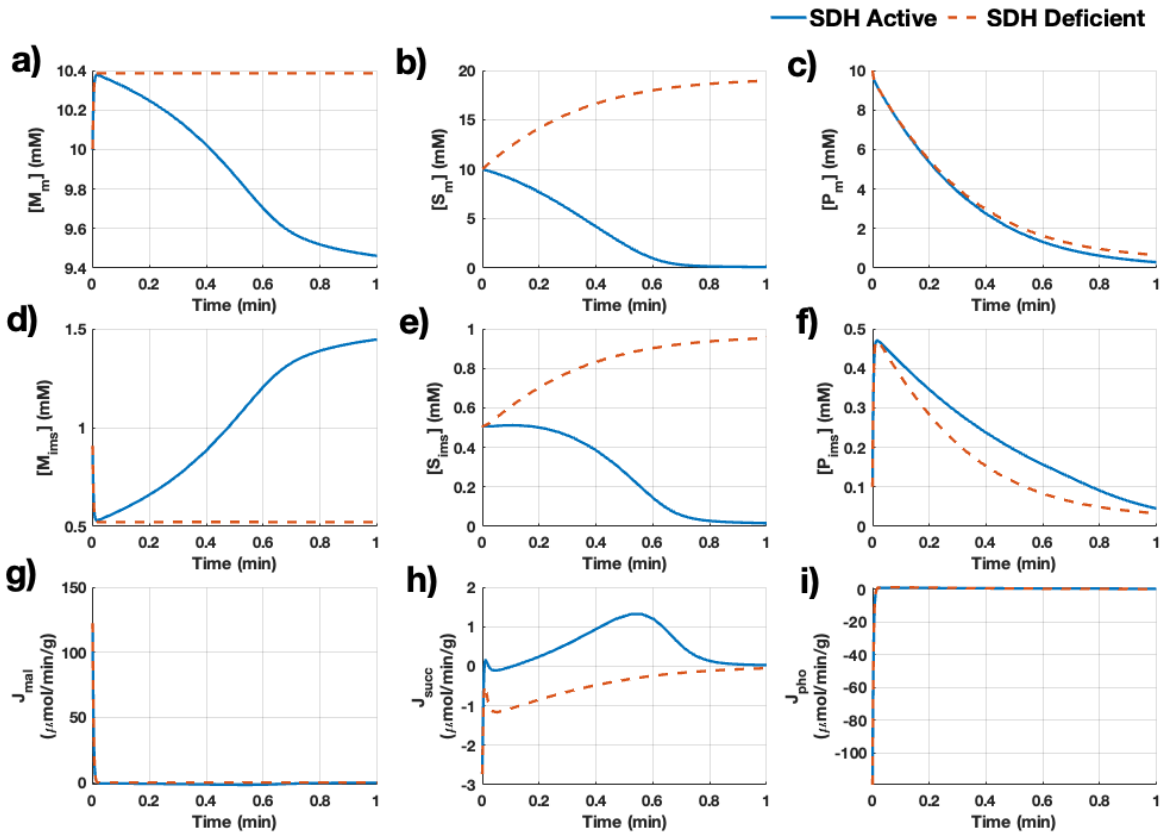

Figure 12: Comparison of metabolite concentration and flux profiles in SDH-active and SDH-deficient conditions. Concentration trajectories in the mitochondrial matrix (MM) and intermembrane space (IMS) under SDH-active (blue) and SDH-deficient (red) conditions: (a) matrix malate $[M_m]$, (b) matrix succinate $[S_m]$, (c) matrix phosphate $[P_m]$, (d) IMS malate $[M_{ims}]$, (e) IMS succinate $[S_{ims}]$, and (f) IMS phosphate $[P_{ims}]$. Flux trajectories in SDH-active (blue) and SDH-deficient (red, dashed) conditions: (g) malate flux (J_{mal}), (h) succinate flux (J_{succ}), and (i) phosphate flux (J_{pho}). Simulations were initialized with IMS concentrations of 0.91 mM malate, 0.5 mM succinate, and 0.1 mM phosphate, and 10 mM of each metabolite in the matrix. Parameter values for $T^s_{\max}$, $T^m_{\max}$, K^s_m, K^m_m, and K^p_m correspond to posterior means, while λ_{21} and λ_{31} were fixed at their posterior modes (Table 4). SDH deficiency was simulated by setting the SDH flux to zero ($J_{\text{SDH}} = 0$).

Finally, to experimentally validate the model predictions, we performed targeted metabolomic analysis using immortalized murine chromaffin cells (imCCs) with inducible knockdown of Slc25a10 (SLC25A10-KD), alongside wild-type imCCs as controls (see Appendix Appendix G for detailed methods). The data revealed significant alterations in intracellular succinate levels attributable to SLC25A10 deficiency. As shown in Fig. 13, succinate accumulated markedly in SLC25A10-KD cells relative to controls, consistent with impaired succinate efflux. These findings provide direct experimental support for the role of SLC25A10 in controlling succinate distribution between the mitochondrial matrix and cytosol.

Our model therefore extends experimental observations by providing a mechanistic framework for how SLC25A10 contributes to succinate handling in SDH deficiency, highlighting its role as both a gatekeeper and a pressure-release valve for matrix succinate levels.

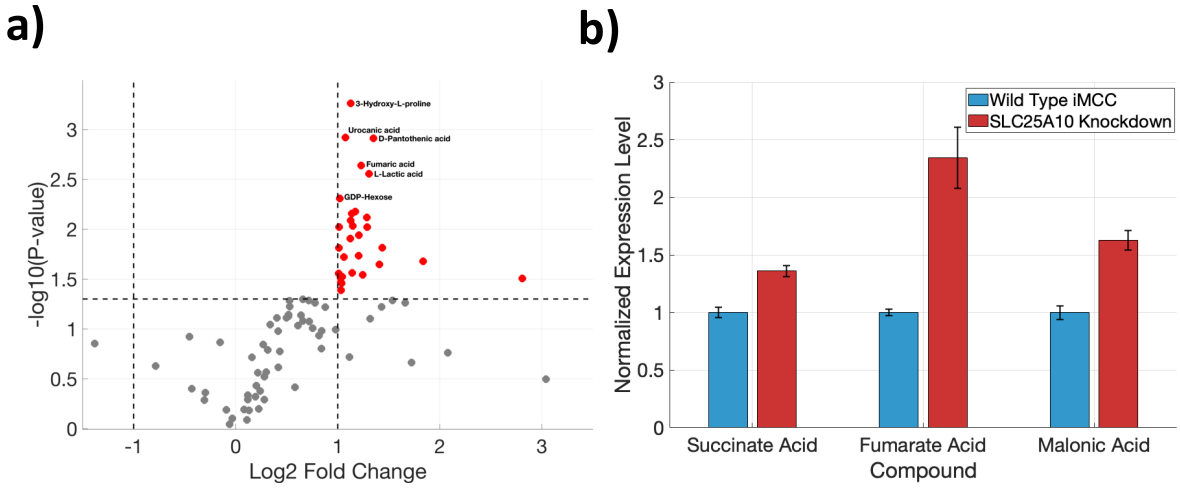

Figure 13: Experimental metabolomics data showing accumulation of dicarboxylates in SLC25A10 knockdown immortalized murine chromaffin cells (imCCs). (a) Differential gene expression (DGE) analysis of metabolites reveals significant upregulation in SLC25A10 knockdown cells. Red dots denote metabolites with statistically significant increases, most prominently succinate, fumarate, and malonic acid, while grey dots represent non-significant changes. **(b)** Comparative metabolite levels in wild-type imCCs (blue) versus SLC25A10 knockdown cells (red), showing elevated concentrations of dicarboxylates in the knockdown condition.

5 Discussion and Conclusion

In this study, we developed the first mechanistically derived and thermodynamically consistent kinetic model of the mitochondrial dicarboxylate carrier SLC25A10, based on the ping–pong mechanism. Our framework incorporates competitive binding, conformational bias weights, and thermodynamic constraints, allowing the model to quantitatively reproduce experimental transport assays while providing mechanistic insights into regimes that remain experimentally inaccessible.

The strengths of the framework extend beyond parameter estimation. Structural identifiability analysis clarified which parameters can be determined from experimental outputs and guided reparameterization. Bayesian inference enabled statistically rigorous calibration of kinetic parameters with credible intervals that quantify uncertainty. Thermodynamic validation ensured compliance with physical laws, confirming that fluxes, Gibbs free energy, and equilibrium concentrations converge consistently. Together, these analyses establish a robust and generalizable modeling platform for mitochondrial carriers of the SLC25 family.

Several kinetic models of SLC25A10 have been proposed previously, including those by Bazil et al. [15] and Zhang et al. [16]. These models incorporate competitive binding, reversibility, heteroexchange, and thermodynamic consistency, but they rely on the assumption of a sequential transport mechanism. Such models were calibrated using classical transport assays [23, 20] and employ the King–Altman method [30] to derive rate equations. While conceptually valuable, this approach simplifies kinetics and lacks mechanistic depth. Recent structural and biophysical evidence, however, demonstrates that SLC25A10 is monomeric with a single binding site, consistent with a ping–pong mechanism [1]. Our work therefore advances the field by explicitly embedding this mechanism into a thermodynamically consistent kinetic framework.

A central innovation of the model is the introduction of conformational bias weights, λ_{21} and λ_{31}, which quantify the relative influence of malate versus succinate and phosphate versus succinate, respectively. Together with the ratios ϕ_1 (Eq. (5)) and ϕ_2 (Eq. (6)), these parameters determine the directional preference of SLC25A10 by defining which substrate and which side of the membrane most strongly bias initiation of the transport cycle. Values near unity indicate equal competition, values below unity indicate succinate dominance, and values above unity indicate bias toward malate or phosphate. From a flux perspective, J_{succ} and J_{mal} depend directly on λ_{21}, while phosphate flux is shaped by λ_{31}. These bias weights thus provide a mechanistic lens for dissecting competitive exchange dynamics beyond what can be inferred from King–Altman–based formulations.

Bayesian analysis revealed that λ_{21} exhibited a broad and skewed posterior distribution, suggesting that the transporter can operate flexibly under different metabolic contexts (Fig. 4). When $\lambda_{21} < 1$, succinate dominates binding and transport, consistent with conditions where succinate accumulates (e.g., SDH deficiency). When $\lambda_{21} > 1$, malate dominates, reflecting increased malate demand to replenish the TCA cycle. This duality suggests that SLC25A10 may act as a metabolic switch, favoring succinate export under pathological accumulation or malate import during high biosynthetic demand. In contrast, λ_{31} showed a tightly centered posterior distribution, indicating that phosphate consistently competes strongly with succinate across conditions. This reflects the obligatory role of phosphate in the ping pong antiport cycle: phosphate is always exchanged and provides the driving force for dicarboxylate transport. Biologically, this suggests that phosphate availability sets a lower bound on transporter activity without sufficient phosphate, succinate and malate exchange cannot proceed efficiently.

Another strength of our framework is its ability to provide mechanistic insight into heteroexchange behavior that is inaccessible to classical transport assays [3, 23]. Conventional uptake experiments measure bulk metabolite exchange but cannot resolve transient dynamics or subcellular gradients. Our simulations revealed that phosphate efflux powers the rapid import of malate and succinate, with malate flux dominating over succinate, and that these fluxes collapse as gradients dissipate (Fig. 8 and Fig. 9). Such transient competition is a hallmark of the ping–pong mechanism but occurs on millisecond timescales, making it experimentally challenging to capture. Thus, the model bridges a critical gap, enabling quantification of exchange kinetics, prediction of driving forces, and analysis of coordinated dicarboxylate–phosphate fluxes.

The simulations also highlight the role of mitochondrial morphology in modulating SLC25A10 activity (Fig. 10). Both IMS and matrix swelling attenuated initial fluxes: IMS swelling diluted extramitochondrial substrate pools, whereas matrix swelling reduced matrix-side saturation. These findings align with experimental and computational studies showing that cristae geometry and compartment volumes strongly influence carrier activity [26, 29]. Thus, SLC25A10 fluxes are constrained not only by enzyme kinetics but also by mitochondrial structure, linking morphology to metabolic adaptation.

Coupling the model to SDH and SCAS fluxes revealed how metabolic context reshapes transport behavior (Fig. 11). Under SDH-active conditions, succinate is rapidly oxidized, and SLC25A10 primarily mediates malate import and phosphate exchange. In contrast, SDH deficiency caused succinate accumulation and its export into the IMS, coupled to malate and phosphate import (Fig. 12). This dual role—import under normal metabolism versus export under deficiency—positions SLC25A10 as both a gatekeeper and a pressure-release valve for matrix succinate. Metabolomics experiments in SLC25A10 knockdown

chromaffin cells corroborated this prediction, showing succinate accumulation when the transporter was impaired (Fig. 13). This mechanistic link between succinate efflux and HIF stabilization [55, 12, 54, 39] underscores the role of SLC25A10 in pseudohypoxic signaling and tumor progression.

Despite these advances, the model has limitations. An important constraint in parameter estimation is the multimodality observed in the posterior distribution of λ_{21}. This reflects the limited resolution of steady-state experimental data, which cannot fully resolve transient conformational preferences, and consequently introduces uncertainty in determining whether succinate or malate exerts stronger control under specific conditions. By contrast, λ_{31} showed tighter constraints and better identifiability.

While a conventional benchmark for MCMC precision is MCSE/$\Sigma < 0.10$, several parameters in our analysis ($T^m_{\max}$, λ_{21}, λ_{31}, and σ^2) stabilized slightly above this threshold (Table 5). We interpret this not as a limitation of the sampling algorithm, since all $\hat{R}$ values were close to 1.0 and effective sample sizes exceeded 490, but rather as a reflection of the limited informativeness of the experimental data. The flux assays used for calibration exhibited correlated measurement errors, restricted dynamic range in substrate concentrations, and posterior correlations between transport rates and bias parameters, which reduced the effective sample size. These features constrain identifiability, making it difficult for any MCMC algorithm to reduce MCSE below this level even with longer chains. We therefore regard the reported MCSE/Σ values as the best achievable under the available data, and emphasize that they provide a reliable empirical calibration of our model. Future work with richer or more diverse experimental datasets should improve identifiability and further reduce Monte Carlo error.

Beyond this, our Bayesian calibration framework assumes independent, identical Gaussian distribution for error in the model prediction. This assumption is clearly an approximation: real experimental errors or model-data discrepancy may be heteroskedastic (larger fluxes incur larger variance), correlated (fluxes are measured under the same assay and share systematic bias), or skewed due to detection limits and instrumental drift. Ignoring such features can lead to overconfident posterior intervals or biased estimates. Nevertheless, we adopted the Gaussian assumption here to enable tractable likelihood evaluation and parameter inference. We view this work as a foundation for more sophisticated calibration methods that incorporate realistic error structures in future work.

Moreover, the ping–pong kinetics are simplified and do not capture potential intermediate conformational states, which may overlook subtle regulatory steps in the transport cycle. The assumption of symmetric rate constants may bias flux predictions by ignoring possible differences in binding and release kinetics. SCAS and SDH fluxes were adopted from the literature rather than jointly re-estimated, potentially reducing quantitative accuracy in simulating coupled dynamics. Compartments were modeled as well-mixed volumes, neglecting sub-mitochondrial microdomains and interactions with other transporters, which may limit applicability to highly structured mitochondrial environments. Finally, experimental calibration relied primarily on isolated mitochondrial assays; tissue-specific regulation, post-translational modifications, and in vivo dynamics remain unexplored, limiting the direct translatability of the model to physiological or pathological states. Future extensions should integrate these features into whole-mitochondrial models for a more comprehensive description.

In conclusion, this work establishes a mechanistically derived, thermodynamically validated kinetic model of SLC25A10 that bridges transporter structure and function. The

model reveals how succinate, malate, and phosphate compete through conformational bias, how mitochondrial morphology shapes transport efficiency, and how SDH deficiency rewires exchange directionality. Beyond reproducing classical transport assays, the framework generates testable predictions and provides a foundation for integrative studies of mitochondrial carrier dynamics. These insights extend our understanding of mitochondrial metabolism and link transporter behavior to broader physiological and pathological processes, including cancer metabolism and conditions in which these metabolites are misregulated, such as in ischaemia. More broadly, the modeling strategy can be generalized to other SLC25 family members, demonstrating the value of combining mechanistic modeling, Bayesian inference, and experimental validation in the study of mitochondrial transport.

References

[1] Camila Cimadamore-Werthein et al. "Human mitochondrial carriers of the SLC25 family function as monomers exchanging substrates with a ping-pong kinetic mechanism". In: *EMBO Journal* (2024). ISSN: 14602075. DOI: 10.1038/s44318-024-00150-0.

[2] Edmund R.S. Kunji et al. "The SLC25 carrier family: Important transport proteins in mitochondrial physiology and pathology". In: *Physiology* 35 (5 Sept. 2020), pp. 302–327. ISSN: 15489221. DOI: 10.1152/physiol.00009.2020.

[3] Ferdinando Palmieri et al. "Kinetic Study of the Dicarboxylate Carrier in Rat Liver Mitochondria". In: *European Journal of Biochemistry* 22 (1 1971), pp. 66–74. ISSN: 14321033. DOI: 10.1111/j.1432-1033.1971.tb01515.x.

[4] Luc Rochette et al. *Mitochondrial SLC25 carriers: Novel targets for cancer therapy.* May 2020. DOI: 10.3390/molecules25102417.

[5] Adrian Casas-Benito, Sonia Martínez-Herrero, and Alfredo Martínez. *Succinate-Directed Approaches for Warburg Effect-Targeted Cancer Management, an Alternative to Current Treatments?* May 2023. DOI: 10.3390/cancers15102862.

[6] Amer Ahmed et al. *The Role of Mitochondrial Solute Carriers SLC25 in Cancer Metabolic Reprogramming: Current Insights and Future Perspectives.* Jan. 2025. DOI: 10.3390/ijms26010092.

[7] Eva Pyrihová et al. "A mitochondrial carrier transports glycolytic intermediates to link cytosolic and mitochondrial glycolysis in the human gut parasite Blastocystis". In: *eLife* 13 (May 2024). ISSN: 2050084X. DOI: 10.7554/ELIFE.94187.

[8] Shinji Mizuarai et al. "Identification of dicarboxylate carrier Slc25a10 as malate transporter in de Novo fatty acid synthesis". In: *Journal of Biological Chemistry* 280 (37 Sept. 2005), pp. 32434–32441. ISSN: 00219258. DOI: 10.1074/jbc.M503152200.

[9] Charlotte Lussey-Lepoutre et al. *Mitochondrial deficiencies in the predisposition to paraganglioma.* June 2017. DOI: 10.3390/metabo7020017.

[10] Julian Hlouschek et al. "Targeting SLC25A10 alleviates improved antioxidant capacity and associated radioresistance of cancer cells induced by chronic-cycling hypoxia". In: *Cancer Letters* 439 (Dec. 2018), pp. 24–38. ISSN: 18727980. DOI: 10.1016/j.canlet.2018.09.002.

[11] Ferdinando Palmieri, Pasquale Scarcia, and Magnus Monné. *Diseases caused by mutations in mitochondrial carrier genes SLC25: A review*. Apr. 2020. DOI: 10.3390/biom10040655.

[12] Katarina Kluckova and Daniel A. Tennant. *Metabolic implications of hypoxia and pseudohypoxia in pheochromocytoma and paraganglioma*. May 2018. DOI: 10.1007/s00441-018-2801-6.

[13] Katarína Kľučková et al. "Succinate dehydrogenase deficiency in a chromaffin cell model retains metabolic fitness through the maintenance of mitochondrial nadh oxidoreductase function". In: *FASEB Journal* 34 (1 2020), pp. 303–315. ISSN: 15306860. DOI: 10.1096/fj.201901456R.

[14] Elías Vera-Sigüenza et al. *A Mathematical Exploration of SDH-b Loss in Chromaffin Cells*. July 2024. DOI: 10.1101/2024.07.15.603520. URL: http://biorxiv.org/lookup/doi/10.1101/2024.07.15.603520.

[15] Jason N. Bazil, Gregery T. Buzzard, and Ann E. Rundell. "Modeling mitochondrial bioenergetics with integrated volume dynamics". In: *PLoS Computational Biology* 6 (1 2010). ISSN: 15537358. DOI: 10.1371/journal.pcbi.1000632.

[16] Xiao Zhang et al. "Integrated computational model of the bioenergetics of isolated lung mitochondria". In: *PLoS ONE* 13 (6 June 2018). ISSN: 19326203. DOI: 10.1371/journal.pone.0197921.

[17] Shima Sadri et al. "Computational Modeling of Substrate-Dependent Mitochondrial Respiration and Bioenergetics in the Heart and Kidney Cortex and Outer Medulla". In: *Function* 4 (5 2023). ISSN: 26338823. DOI: 10.1093/function/zqad038.

[18] J J Ruprecht and E R S Kunji. "Annual Review of Biochemistry Structural Mechanism of Transport of Mitochondrial Carriers". In: (2021). DOI: 10.1146/annurev-biochem-072820. URL: https://doi.org/10.1146/annurev-biochem-072820-.

[19] Vasiliki Mavridou et al. "Substrate binding in the mitochondrial ADP/ATP carrier is a step-wise process guiding the structural changes in the transport cycle". In: *Nature Communications* 13 (1 Dec. 2022). ISSN: 20411723. DOI: 10.1038/s41467-022-31366-5.

[20] F. Palmieri. *Mitochondrial carrier proteins*. June 1994. DOI: 10.1016/0014-5793(94)00329-7.

[21] R N Johnson and J B Chappell. *The Transport of Inorganic Phosphate by the Mitochondrial Dicarboxylate Carrier*. 1973. URL: http://portlandpress.com/biochemj/article-pdf/134/3/769/780527/bj1340769.pdf.

[22] F Bisaccia, C Indiveri, and F Palmieri. *Purification and reconstitution of two anion carriers from rat liver mitoehondria: the dicarboxylate and the 2-oxoglutarate carrier*. 1988.

[23] C Indiveri et al. *Kinetics of the reconstituted dicarboxylate carrier from rat liver mitochondria*. 1989.

[24] C Indiveri et al. *Kinetic discrimination of two substrate binding sites of the reconstituted dicarboxylate carrier from rat liver mitochondria*. 1989.

[25] Emmet A Francis et al. "Spatial modeling algorithms for reactions and transport in biological cells". en. In: *Nat. Comput. Sci.* 5.1 (Jan. 2025), pp. 76–89.

[26] Guadalupe C Garcia et al. "Mitochondrial morphology provides a mechanism for energy buffering at synapses". en. In: *Sci. Rep.* 9.1 (Dec. 2019), p. 18306.

[27] Sabzali Javadov, Xavier Chapa-Dubocq, and Vladimir Makarov. "Different approaches to modeling analysis of mitochondrial swelling". In: *Mitochondrion* 38 (Jan. 2018), pp. 58–70.

[28] Raquel Adams et al. "How the topology of the mitochondrial inner membrane modulates ATP production". en. In: *Cells* 14.4 (Feb. 2025), p. 257.

[29] Nasrin Afzal et al. "Effect of crista morphology on mitochondrial ATP output: A computational study". en. In: *Curr. Res. Physiol.* 4 (Apr. 2021), pp. 163–176.

[30] By L Edward King and Carl Altman. *Method of Deriving Rate Laws for Enzyme-catalyzed Reactions A SCHEMATIC METHOD OF DERIVING THE RATE LAWS FOR ENZYME-CATALYZED REACTIONS*. 2025. URL: `https://pubs.acs.org/sharingguidelines`.

[31] Lucy R Forrest, Reinhard Krämer, and Christine Ziegler. "The structural basis of secondary active transport mechanisms". en. In: *Biochim. Biophys. Acta* 1807.2 (Feb. 2011), pp. 167–188.

[32] Jonathan J. Ruprecht and Edmund R.S. Kunji. *The SLC25 Mitochondrial Carrier Family: Structure and Mechanism*. Mar. 2020. DOI: `10.1016/j.tibs.2019.11.001`.

[33] Alex Berlaga and Anatoly B. Kolomeisky. "Molecular Mechanisms of Active Transport in Antiporters: Kinetic Constraints and Efficiency". In: *Journal of Physical Chemistry Letters* 12 (39 Oct. 2021), pp. 9588–9594. ISSN: 19487185. DOI: `10.1021/acs.jpclett.1c02846`.

[34] Alex Berlaga and Anatoly B. Kolomeisky. "Understanding Mechanisms of Secondary Active Transport by Analyzing the Effects of Mutations and Stoichiometry". In: *Journal of Physical Chemistry Letters* 13 (24 June 2022), pp. 5405–5412. ISSN: 19487185. DOI: `10.1021/acs.jpclett.2c01232`.

[35] Alex Berlaga and Anatoly B. Kolomeisky. "Theoretical study of active secondary transport: Unexpected differences in molecular mechanisms for antiporters and symporters". In: *Journal of Chemical Physics* 156 (8 Feb. 2022). ISSN: 10897690. DOI: `10.1063/5.0082589`.

[36] Jonathan J. Ruprecht et al. "The Molecular Mechanism of Transport by the Mitochondrial ADP/ATP Carrier". In: *Cell* 176 (3 Jan. 2019), 435–447.e15. ISSN: 10974172. DOI: `10.1016/j.cell.2018.11.025`.

[37] W. F. Widdas. "Inability of diffusion to account for placental glucose transfer in the sheep and consideration of the kinetics of a possible carrier transfer". In: *Journal of Physiology* 118 (1952), pp. 23–39.

[38] Clifford S. Patlak. "Contributions to the theory of active transport". In: *Bulletin of Mathematical Biology* 18 (1956), pp. 271–315. URL: `https://api.semanticscholar.org/CorpusID:119838164`.

[39] Elías Vera-Sigüenza et al. "A mathematical exploration of SDH-b loss in chromaffin cells". en. In: *Bull. Math. Biol.* 87.4 (Mar. 2025), p. 53.

[40] Alejandro F. Villaverde et al. "A protocol for dynamic model calibration". In: *Briefings in Bioinformatics* 23 (1 Jan. 2022). ISSN: 14774054. DOI: 10.1093/bib/bbab387.

[41] Alejandro F. Villaverde, Antonio Barreiro, and Antonis Papachristodoulou. "Structural Identifiability of Dynamic Systems Biology Models". In: *PLoS Computational Biology* 12 (10 Oct. 2016). ISSN: 15537358. DOI: 10.1371/journal.pcbi.1005153.

[42] Hanwen Huang, Andreas Handel, and Xiao Song. "A Bayesian approach to estimate parameters of ordinary differential equation". In: *Computational Statistics* 35 (3 Sept. 2020), pp. 1481–1499. ISSN: 16139658. DOI: 10.1007/s00180-020-00962-8.

[43] Christophe Andrieu et al. "On the utility of Metropolis-Hastings with asymmetric acceptance ratio". In: (Mar. 2018). URL: http://arxiv.org/abs/1803.09527.

[44] C Indlverl et al. "Kinetic characterization of the reconstituted dicarboxylate carrier from mitochondria: a four-binding-site sequential transport system". In: *Btochtmtca et Btophystca Acta* (1993), pp. 310–318.

[45] Aki Vehtarh et al. "Rank-Normalization, Folding, and Localization: An Improved (Formula presented) for Assessing Convergence of MCMC (with Discussion)*†". In: *Bayesian Analysis* 16 (2 2021), pp. 667–718. ISSN: 19316690. DOI: 10.1214/20-BA1221.

[46] Andrew Gelman et al. *Bayesian Data Analysis*. 3rd. London: Chapman & Hall/CRC, 2013.

[47] Bob Carpenter et al. "Stan: A probabilistic programming language". In: *Journal of Statistical Software* 76 (1 2017). ISSN: 15487660. DOI: 10.18637/jss.v076.i01.

[48] Ying Liu, Dootika Vats, and James M. Flegal. "Batch Size Selection for Variance Estimators in MCMC". In: *Methodology and Computing in Applied Probability* 24 (1 Mar. 2022), pp. 65–93. ISSN: 15737713. DOI: 10.1007/s11009-020-09841-7.

[49] Andrew Gelman and Donald B Rubin. "Inference from iterative simulation using multiple sequences". In: *Stat. Sci.* 7.4 (Nov. 1992), pp. 457–472.

[50] P. Stephen et al. "General methods for monitoring convergence of iterative simulations". In: *Journal of Computational and Graphical Statistics* 7 (1998), pp. 434–455. URL: https://api.semanticscholar.org/CorpusID:7300890.

[51] Stefan J. Jol et al. "Thermodynamic calculations for biochemical transport and reaction processes in metabolic networks". In: *Biophysical Journal* 99 (10 Nov. 2010), pp. 3139–3144. ISSN: 15420086. DOI: 10.1016/j.bpj.2010.09.043.

[52] X. Li et al. "A database of thermodynamic quantities for the reactions of glycolysis and the tricarboxylic acid cycle". In: *Journal of Physical Chemistry B* 114 (49 Dec. 2010), pp. 16068–16082. ISSN: 15205207. DOI: 10.1021/jp911381p.

[53] Katarina Kluckova and Daniel A Tennant. "Metabolic implications of hypoxia and pseudohypoxia in pheochromocytoma and paraganglioma". In: *Cell and tissue research* 372 (2018), pp. 367–378.

[54] Katarína Kl'učková et al. "Succinate dehydrogenase deficiency in a chromaffin cell model retains metabolic fitness through the maintenance of mitochondrial NADH oxidoreductase function". In: *The FASEB Journal* 34.1 (2020), pp. 303–315.

[55] G. M. Tannahill et al. "Succinate is an inflammatory signal that induces IL-1 through HIF-1". In: *Nature* 496 (7444 Apr. 2013), pp. 238–242. ISSN: 00280836. DOI: 10.1038/nature11986.

[56] Wm Wallace Cleland. *Derivation of Rate Equations for Multisite Ping-Pong Mechanisms with Ping-Pong Reactions at One or More Sites**. 1973.

[57] Eric Letouzé et al. "SDH mutations establish a hypermethylator phenotype in paraganglioma". In: *Cancer cell* 23.6 (2013), pp. 739–752.

Data Availability

The codes used in this article are publicly available on the Github webpage:
https://github.com/rxn315/MATHEMATICAL-MODEL-SLC25A10.git

Acknowledgements

ES was supported by a Cancer Research UK grant (C42109/A24757). YL was supported by The Paradifference Foundation. FS was supported by a UKRI Future Leaders Fellowship (MR/T043571/1). We acknowledge that we used ChatGPT to refine and enhance the clarity of this article. However, all ideas and content are our own, and we take full responsibility for the final submission. Additionally, I acknowledge the use of BioRender in creating some of the scientific illustrations for this article.

Author Contributions

Ramin Nashebi: Mathematical model conceptualisation, computational methodology, software, visualisation, model validation, model analysis, writing, and editing.

Yingying Liu: Experimental data procurement and writing the description of the experimental work.

Elías Vera-Sigüenza: Model Validation, model analysis, article review.

Daniel A. Tennant: Conceptualisation, experimental data validation, article review, and editing.

Fabian Spill: Mathematical model conceptualisation, model validation, article review and editing, supervised and managed the study.

Appendix A Full ODE System for SLC25A10 Ping–Pong Model

The complete set of ordinary differential equations (ODEs) governing transporter states, complexes, and metabolite concentrations is:

$$\frac{d[T_m]}{dt} = -k_1^s[T_m][S_m] + k_{-1}^s[T_mS_m] - k_1^m[T_m][M_m] + k_{-1}^m[T_mM_m] + k_3^p[T_mP_m] - k_{-3}^p[T_m][P_m], \tag{A.1}$$

$$\frac{d[T_mS_m]}{dt} = k_1^s[T_m][S_m] - k_{-1}^s[T_mS_m] - k_c^s[T_mS_m] + k_{-c}^s[T_{ims}S_{ims}], \tag{A.2}$$

$$\frac{d[T_mM_m]}{dt} = k_1^m[T_m][M_m] - k_{-1}^m[T_mM_m] - k_c^m[T_mM_m] + k_{-c}^m[T_{ims}M_{ims}], \tag{A.3}$$

$$\frac{d[T_{ims}S_{ims}]}{dt} = k_c^s[T_mS_m] - k_{-c}^s[T_{ims}S_{ims}] - k_3^s[T_{ims}S_{ims}] + k_{-3}^s[T_{ims}][S_{ims}], \tag{A.4}$$

$$\frac{d[T_{ims}M_{ims}]}{dt} = k_c^m[T_mM_m] - k_{-c}^m[T_{ims}M_{ims}] - k_3^m[T_{ims}M_{ims}] + k_{-3}^m[T_{ims}][M_{ims}], \tag{A.5}$$

$$\frac{d[T_{ims}P_{ims}]}{dt} = k_1^p[T_{ims}][P_{ims}] - k_{-1}^p[T_{ims}P_{ims}] - k_c^p[T_{ims}P_{ims}] + k_{-c}^p[T_mP_m], \tag{A.6}$$

$$\frac{d[T_mP_m]}{dt} = k_c^p[T_{ims}P_{ims}] - k_{-c}^p[T_mP_m] - k_3^p[T_mP_m] + k_{-3}^p[T_m][P_m], \tag{A.7}$$

$$\frac{d[T_{ims}]}{dt} = -k_1^p[T_{ims}][P_{ims}] + k_{-1}^p[T_{ims}P_{ims}] + k_3^s[T_{ims}S_{ims}] - k_{-3}^s[T_{ims}][S_{ims}] + k_3^m[T_{ims}M_{ims}] - k_{-3}^m[T_{ims}][M_{ims}], \tag{A.8}$$

$$\frac{d[S_m]}{dt} = \frac{1}{V_m}\Big(- k_1^s[T_m][S_m] + k_{-1}^s[T_mS_m]\Big), \tag{A.9}$$

$$\frac{d[M_m]}{dt} = \frac{1}{V_m}\Big(- k_1^m[T_m][M_m] + k_{-1}^m[T_mM_m]\Big), \tag{A.10}$$

$$\frac{d[S_{ims}]}{dt} = \frac{1}{V_{ims}}\Big(k_3^s[T_{ims}S_{ims}] - k_{-3}^s[T_{ims}][S_{ims}]\Big), \tag{A.11}$$

$$\frac{d[M_{ims}]}{dt} = \frac{1}{V_{ims}}\Big(k_3^m[T_{ims}M_{ims}] - k_{-3}^m[T_{ims}][M_{ims}]\Big), \tag{A.12}$$

$$\frac{d[P_{ims}]}{dt} = \frac{1}{V_{ims}}\Big(- k_1^p[T_{ims}][P_{ims}] + k_{-1}^p[T_{ims}P_{ims}]\Big), \tag{A.13}$$

$$\frac{d[P_m]}{dt} = \frac{1}{V_m}\Big(k_3^p[T_mP_m] - k_{-3}^p[T_m][P_m]\Big). \tag{A.14}$$

Appendix B Chemical Reaction Network of Ping-Pong Mechanism After Fast Conformational change assumption

Fast conformational change assumption simplifies the kinetics of SLC25A10 transporter by assuming a rapid translocation event relative to substrate binding and release [1, 2, 36]. Consequently, the transporter-substrate complexes on mitochondrial-side (T_mS_m, T_mM_m,

T_mP_m) and inner membrane-side ($T_{ims}S_{ims}$, $T_{ims}M_{ims}$, $T_{ims}P_{ims}$) are lumped together and the conformational change consider instantaneous. This allows us to merge the MM facing intermediates and IMS facing intermediates:

$$T_mS_m \underset{k_{-1}^s}{\overset{k_3^s}{\rightleftharpoons}} T_{ims}S_{ims}$$

$$T_mM_m \underset{k_{-1}^m}{\overset{k_3^m}{\rightleftharpoons}} T_{ims}M_{ims}$$

$$T_{ims}P_{ims} \underset{k_{-1}^p}{\overset{k_3^p}{\rightleftharpoons}} T_mP_m$$

into single effective reactions for forward cycle as follow:

$$T_mS_m \underset{k_{-3}^s}{\overset{k_3^s}{\rightleftharpoons}} T_{ims} + S_{ims},$$

$$T_mM_m \underset{k_{-1}^m}{\overset{k_3^m}{\rightleftharpoons}} T_{ims} + M_{ims}.$$

$$T_{ims}P_{ims} \underset{k_{-3}^p}{\overset{k_3^p}{\rightleftharpoons}} T_m + P_m.$$

and reverse cycle as follows:

$$T_{ims}S_{ims} \underset{k_1^s}{\overset{k_{-1}^s}{\rightleftharpoons}} T_m + S_m,$$

$$T_{ims}M_{ims} \underset{k_1^m}{\overset{k_{-1}^m}{\rightleftharpoons}} T_m + M_m.$$

$$T_mP_m \underset{k_1^p}{\overset{k_{-1}^p}{\rightleftharpoons}} T_{ims} + P_{ims}.$$

Under this assumption the ODEs describing the system dynamics are simplified as follows:

$$\frac{d[T_m]}{dt} = -2k_1^s[T_m][S_m] + k_{-1}^s[T_mS_m] + k_{-1}^s[T_{ims}S_{ims}] - 2k_1^m[T_m][M_m] + k_{-1}^m[T_mM_m + k_{-1}^m[T_{ims}M_{ims}] + k_3^p[T_{ims}P_{ims}] + k_3^p[T_mP_m] - 2k_{-3}^p[T_m][P_m], \tag{B.1}$$

$$\frac{d[T_mS_m]}{dt} = k_1^s[T_m][S_m] - k_{-1}^s[T_mS_m] - k_3^s[T_mS_m] + k_{-3}^s[T_{ims}][S_{ims}], \tag{B.2}$$

$$\frac{d[T_mM_m]}{dt} = k_1^m[T_m][M_m] - k_{-1}^m[T_mM_m] - k_3^m[T_mM_m] + k_{-1}^m[T_{ims}][M_{ims}], \tag{B.3}$$

$$\frac{d[T_{ims}S_{ims}]}{dt} = k_1^s[T_m][S_m] - k_{-1}^s[T_{ims}S_{ims}] - k_3^s[T_{ims}S_{ims}] + k_{-3}^s[T_{ims}][S_{ims}], \tag{B.4}$$

$$\frac{d[T_{ims}M_{ims}]}{dt} = k_1^m[T_m][M_m] - k_{-1}^m[T_{ims}M_{ims}] - k_3^m[T_{ims}M_{ims}] + k_{-1}^m[T_{ims}][M_{ims}], \tag{B.5}$$

$$\frac{d[T_{ims}P_{ims}]}{dt} = k_1^p[T_{ims}][P_{ims}] - k_{-1}^p[T_{ims}P_{ims}] - k_3^p[T_{ims}P_{ims}] + k_{-3}^p[T_m][P_m], \tag{B.6}$$

$$\frac{d[T_mP_m]}{dt} = k_1^p[T_{ims}][P_{ims}] - k_{-1}^p[T_mP_m] - k_3^p[T_mP_m] + k_{-3}^p[T_m][P_m], \tag{B.7}$$

$$\frac{d[T_{ims}]}{dt} = -2k_1^p[T_{ims}][P_{ims}] + k_{-1}^p[T_{ims}P_{ims}] + k_{-1}^p[T_mP_m] + k_3^s[T_mS_m] + k_3^s[T_{ims}S_{ims}] - 2k_{-3}^s[T_{ims}][S_{ims}] + k_3^m[T_{ims}M_{ims}] + k_3^m[T_mM_m] - 2k_{-1}^m[T_{ims}][M_{ims}], \tag{B.8}$$

$$\frac{d[S_m]}{dt} = \frac{1}{V_m}\Big(- 2k_1^s[T_m][S_m] + k_{-1}^s[T_mS_m] + k_{-1}^s[T_{ims}S_{ims}]\Big), \tag{B.9}$$

$$\frac{d[M_m]}{dt} = \frac{1}{V_m}\Big(- 2k_1^m[T_m][M_m] + k_{-1}^m[T_mM_m] + k_{-1}^m[T_{ims}M_{ims}]\Big), \tag{B.10}$$

$$\frac{d[S_{ims}]}{dt} = \frac{1}{V_{ims}}\Big(k_3^s[T_{ims}S_{ims}] + k_3^s[T_mS_m] - 2k_{-3}^s[T_{ims}][S_{ims}]\Big), \tag{B.11}$$

$$\frac{d[M_{ims}]}{dt} = \frac{1}{V_{ims}}\Big(k_3^m[T_{ims}M_{ims}] + k_3^m[T_mM_m] - 2k_{-1}^m[T_{ims}][M_{ims}]\Big), \tag{B.12}$$

$$\frac{d[P_{ims}]}{dt} = \frac{1}{V_{ims}}\Big(- 2k_1^p[T_{ims}][P_{ims}] + k_{-1}^p[T_{ims}P_{ims}] + k_{-1}^p[T_mP_m]\Big), \tag{B.13}$$

$$\frac{d[P_m]}{dt} = \frac{1}{V_m}\Big(k_3^p[T_mP_m] + k_3^p[T_{ims}P_{ims}] - 2k_{-3}^p[T_m][P_m]\Big). \tag{B.14}$$

Under this formulation, both the forward and reverse cycles of the ping–pong mechanism are explicitly represented: the forward reactions capture dicarboxylate import coupled to phosphate export, while the reverse reactions describe phosphate import coupled to dicarboxylate efflux. Together, these terms ensure that the ODE system accounts for fully reversible exchange dynamics across the mitochondrial inner membrane.

Appendix C Symmetric Transport Assumption

We assume that the SLC25A10 transporter operates under a symmetric transport mechanism [33, 34, 35]. Under this assumption, the rate constants governing substrate binding,

conformational transitions, and product release are identical in magnitude for both the mitochondrial matrix and IMS directions. For example, in the case of succinate, the binding and release rates on the matrix side (k_1^s, k_{-1}^s) are assumed equal to the corresponding reverse-direction rates on the IMS side (k_{-3}^s, k_3^s):

$$k_1^s = k_{-3}^s, \tag{C.1}$$

$$k_{-1}^s = k_3^s. \tag{C.2}$$

Analogous relations hold for malate and phosphate. This symmetry reduces the number of independent kinetic parameters, facilitates parameter estimation, and ensures that the transporter satisfies microscopic reversibility and detailed balance at equilibrium.

Appendix D The Quasi-Steady-State Assumption and Derivation of the Rate Equation

Appendix D.1 Forward Cycle

We utilize the quasi-steady-state assumption, a fundamental concept in Michaelis-Menten enzyme kinetics, which can also be extended to transport processes [37, 38]. This assumption posits that, at steady state, in forward cycle the rates of formation and dissociation of the transporter-substrate complexes T_mS_m, T_mM_m, and $T_{ims}P_{ims}$ are balanced, leading to constant concentrations of these intermediates over time. For instance, the steady-state condition for T_mS_m results in the following:

$$\frac{d[T_mS_m]}{dt} = k_1^s[T_m][S_m] - k_{-1}^s[T_mS_m] - k_3^s[T_mS_m] + k_{-3}^s[T_{ims}][S_{ims}] = 0. \tag{D.1}$$

$$[T_mS_m] = \frac{k_1^s[T_m][S_m]}{k_{-1}^s + k_3^s} + \frac{k_{-3}^s[T_{ims}][S_{ims}]}{k_{-1}^s + k_3^s}. \tag{D.2}$$

Define the Michaelis-Menten constant for forward cycle for succinate considering symmetry as, respectively:

$$K_m^s = \frac{k_{-1}^s + k_3^s}{k_1^s} = \frac{k_{-1}^s + k_3^s}{k_{-3}^s}. \tag{D.3}$$

By substituting eq. (D.3) into eq. (D.2), the concentration of T_mS_m becomes:

$$[T_mS_m] = \frac{[T_m][S_m] + [T_{ims}][S_{ims}]}{K_m^s} \tag{D.4}$$

The formation and breakdown of T_mM_m and $T_{ims}P_{ims}$ follow the same reaction structure as succinate. Thus, applying the same derivation procedure as used for succinate, the concentration of T_mM_m is given by:

$$[T_mM_m] = \frac{[T_m][M_m] + [T_{ims}][M_{ims}]}{K_m^m}. \tag{D.5}$$

where the forward Michaelis-Menten constant for malate is defined as:

$$K_m^m = \frac{k_{-1}^m + k_3^m}{k_1^m} = \frac{k_{-1}^m + k_3^m}{k_{-3}^m}. \tag{D.6}$$

Similarly, the concentration of $T_{ims}P_{ims}$ is given by:

$$[T_{ims}P_{ims}] = \frac{[T_{ims}][P_{ims}] + [T_m][P_m]}{K_m^p}. \tag{D.7}$$

where the forward Michaelis-Menten constant for phosphate is defined as:

$$K_m^p = \frac{k_{-1}^p + k_3^p}{k_1^p} = \frac{k_{-1}^p + k_3^p}{k_{-3}^p}. \tag{D.8}$$

We continue the derivation of the rate equations for forward cycle with a description of the product formation rates for the intermediate products S_{ims} and M_{ims}, which result from the reaction of the transporter-substrate complexes T_mS_m and T_mM_m, respectively. The rate of intermediate product formation for forward cycle, denoted as v_1^f, is the sum of the contributions from both pathways. Each pathway corresponds to a specific substrate bound to the transporter, leading to the following expression:

$$v_1^f = \frac{d[S_{ims}]}{dt} + \frac{d[M_{ims}]}{dt} \tag{D.9}$$

$$= \frac{1}{V_{ims}}\left(k_3^s[T_mS_m] - k_{-3}^s[T_{ims}][S_{ims}] + k_3^m[T_mM_m] - k_{-3}^m[T_{ims}][M_{ims}]\right). \tag{D.10}$$

This equation reflects the fact that the production of S_{ims} or M_{ims} depends on the conformational rates k_3^s and k_3^m of their respective complexes. To make this expression more practical, we substitute the steady-state concentrations of $[T_mS_m]$ (eq. (D.4)) and $[T_mM_m]$ (eq. (D.5)), which are derived from the Michaelis-Menten relationship. Substituting these expressions gives:

$$v_1^f = \frac{1}{V_{ims}}\left(k_3^s\frac{[T_m][S_m] + [T_{ims}][S_{ims}]}{K_m^s} - k_{-3}^s[T_{ims}][S_{ims}]\right. \tag{D.11}$$

$$\left. + k_3^m\frac{[T_m][M_m] + [T_{ims}][M_{ims}]}{K_m^m} - k_{-3}^m[T_{ims}][M_{ims}]\right), \tag{D.12}$$

where K_m^s and K_m^m are the Michaelis constants for S_m and M_m, respectively. By substituting K_m^s and K_m^m from equation (D.3) and (D.6) we can Simplify this equation as follow:

$$v_1^f = \frac{1}{V_{ims}}\left(\frac{k_3^s[T_m][S_m] - k_{-1}^s[T_{ims}][S_{ims}]}{K_m^s} + \frac{k_3^m[T_m][M_m] - k_{-1}^m[T_{ims}][M_{ims}]}{K_m^m}\right), \tag{D.13}$$

using symmetry, we can further simplified it into:

$$v_1^f = \frac{1}{V_{ims}}\left(\frac{k_3^s\left([T_m][S_m] - [T_{ims}][S_{ims}]\right)}{K_m^s} + \frac{k_3^m\left([T_m][M_m] - [T_{ims}][M_{ims}]\right)}{K_m^m}\right), \tag{D.14}$$

$$v_1^f = \frac{1}{V_{ims}}\left[[T_m]\left(\frac{[S_m]}{K_s} + \frac{[M_m]}{K_m}\right) - [T_{ims}]\left(\frac{[S_{ims}]}{K_s} + \frac{[M_{ims}]}{K_m}\right)\right], \tag{D.15}$$

where $K_s = \frac{K_3^s}{K_m^s}$ and $K_m = \frac{K_3^m}{K_m^m}$.

This equation demonstrates that v_1^f is directly proportional to the free transporter concentration $[T_m]$ and the substrate concentrations $[S_m]$ and $[M_m]$, modulated by their respective Michaelis constants.

The rate of the final product P_m formation in forward cycle, denoted as v_2^f, is determined by the conversion of the transporter-product complex $T_{ims}P_{ims}$ to P_m. The rate is expressed as:

$$v_2^f = \frac{d[P_m]}{dt} = \frac{1}{V_m}\left(k_3^p[T_{ims}P_{ims}] - k_{-3}^p[T_m][P_m]\right). \tag{D.16}$$

Substituting the steady-state concentration of $[T_{ims}P_{ims}]$ (eq. (D.7)), we obtain:

$$v_2^f = \frac{1}{V_m}\left(k_3^p\frac{[T_{ims}][P_{ims}] + [T_m][P_m]}{K_m^p} - k_{-3}^p[T_m][P_m]\right), \tag{D.17}$$

where K_m^p is the Michaelis constant for the secondary substrate P_{ims}. By substituting K_m^p from equation (D.8), we can simplify this equation as follows:

$$v_2^f = \frac{1}{V_m}\left(\frac{k_3^p[T_{ims}][P_{ims}] - k_{-1}^p[T_m][P_m]}{K_m^p}\right), \tag{D.18}$$

using symmetry, we can further simplified it into:

$$v_2^f = \frac{1}{V_m}\left(\frac{k_3^p[T_{ims}][P_{ims}] - k_3^p[T_m][P_m]}{K_m^p}\right), \tag{D.19}$$

$$v_2^f = \frac{1}{V_m}\left[[T_{ims}]\left(\frac{[P_{ims}]}{K_p}\right) - [T_m]\left(\frac{[P_m]}{K_p}\right)\right], \tag{D.20}$$

where $K_p = \frac{K_3^p}{K_m^p}$.
This equation highlights that v_2^f depends on the concentration of the modified transporter $[T_{ims}]$, the concentration of P_{ims}, and their specific binding and turnover rates.

In a cyclic reaction mechanism, such as the ping-pong kinetics described here, the flux of the transporter through the cycle must remain constant at a steady state [56]. This requires that in forward cycle the rate of P_m production (v_2^f) matches the rate of intermediate product S_{ims} and M_{ims} production (v_1^f). The transporter continuously cycles through its states ($T_m \rightarrow T_{ims} \rightarrow T_m$) without the accumulation of intermediates ($T_mS_m, T_mM_m, T_{ims}P_{ims}$). At steady state, the concentrations of all transporter-bound complexes remain constant, ensuring that the rates of their formation and breakdown are equal. Consequently, the rates of production for S_{ims}, M_{ims}, and P_m must also be equal:

$$v_1^f = v_2^f. \tag{D.21}$$

This equality ensures a balanced flux throughout the reaction cycle, reflecting the intrinsic coordination of the transporter's kinetic properties. By equating v_1^f and v_2^f, and substituting the expressions for $[T_m S_m]$, $[T_m M_m]$, and $[T_{ims} P_{ims}]$, the rate equations can be further simplified to reflect the dependence of product formation on substrate concentrations and transporter kinetics. This steady-state analysis underpins the core principles of the ping-pong kinetics mechanism with competitive substrate binding.

By substituting the steady-state expressions for $[T_m S_m]$ (eq. (D.4)), $[T_m M_m]$ (eq. (D.5)) and $[T_{ims} P_{ims}]$ (eq. (D.7)), into this equality, we get:

$$\frac{1}{V_{ims}}\left[[T_m]\left(\frac{[S_m]}{K_s}+\frac{[M_m]}{K_m}\right)-[T_{ims}]\left(\frac{[S_{ims}]}{K_s}+\frac{[M_{ims}]}{K_m}\right)\right]=\frac{1}{V_m}\left[[T_{ims}]\left(\frac{[P_{ims}]}{K_p}\right)-[T_m]\left(\frac{[P_m]}{K_p}\right)\right], \tag{D.22}$$

$$\frac{[T_m]}{V_{ims}}\left(\frac{[S_m]}{K_s}+\frac{[M_m]}{K_m}\right)-\frac{[T_{ims}]}{V_{ims}}\left(\frac{[S_{ims}]}{K_s}+\frac{[M_{ims}]}{K_m}\right)=\frac{[T_{ims}]}{V_m}\left(\frac{[P_{ims}]}{K_p}\right)-\frac{[T_m]}{}V_m\left(\frac{[P_m]}{K_p}\right), \tag{D.23}$$

$$\frac{[T_m]}{V_{ims}}\left(\frac{[S_m]}{K_s}+\frac{[M_m]}{K_m}\right)+\frac{[T_m]}{V_m}\left(\frac{[P_m]}{K_p}\right)=\frac{[T_{ims}]}{V_m}\left(\frac{[P_{ims}]}{K_p}\right)+\frac{[T_{ims}]}{V_{ims}}\left(\frac{[S_{ims}]}{K_s}+\frac{[M_{ims}]}{K_m}\right), \tag{D.24}$$

$$[T_m]\left(\frac{[S_m]}{V_{ims}K_s}+\frac{[M_m]}{V_{ims}K_m}+\frac{[P_m]}{V_mK_p}\right)=[T_{ims}]\left(\frac{[P_{ims}]}{V_mK_p}+\frac{[S_{ims}]}{V_{ims}K_s}+\frac{[M_{ims}]}{V_{ims}K_m}\right), \tag{D.25}$$

$$[T_m]\left(\lambda_1[S_m]+\lambda_2[M_m]+\lambda_3[P_m]\right)=[T_{ims}]\left(\lambda_3[P_{ims}]+\lambda_1[S_{ims}]+\lambda_2[M_{ims}]\right), \tag{D.26}$$

where $\lambda_1=\frac{1}{V_{ims}K_s}$, $\lambda_2=\frac{1}{V_{ims}K_m}$, and $\lambda_3=\frac{1}{V_mK_p}$ solving for T_{ims}, we get:

$$[T_m]\left(\frac{\lambda_1[S_m]+\lambda_2[M_m]+\lambda_3[P_m]}{\lambda_1[S_{ims}]+\lambda_2[M_{ims}]+\lambda_3[P_{ims}]}\right)=[T_{ims}], \tag{D.27}$$

$$[T_m]\left(\frac{[S_m]+\frac{\lambda_2}{\lambda_1}[M_m]+\frac{\lambda_3}{\lambda_1}[P_m]}{[S_{ims}]+\frac{\lambda_2}{\lambda_1}[M_{ims}]+\frac{\lambda_3}{\lambda_1}[P_{ims}]}\right)=[T_{ims}], \tag{D.28}$$

$$[T_m]\phi_1=[T_{ims}], \tag{D.29}$$

where $\frac{\lambda_2}{\lambda_1}=\lambda_{21}$, and $\frac{\lambda_3}{\lambda_1}=\lambda_{31}$.

$$\phi_1=\left(\frac{[S_m]+\lambda_{21}[M_m]+\lambda_{31}[P_m]}{[S_{ims}]+\lambda_{21}[M_{ims}]+\lambda_{31}[P_{ims}]}\right)$$

$$\phi_1=\frac{\lambda_1[S_m]+\lambda_2[M_m]+\lambda_3[P_m]}{\lambda_1[S_{ims}]+\lambda_2[M_{ims}]+\lambda_3[P_{ims}]}$$

Appendix D.1.1 Total Transporter Conservation

The total transporter concentration $[T_{\text{total}}]$ is distributed between all transporter states, leading to the expression:

$$[T_{\text{total}}] = [T_m] + [T_m S_m] + [T_m M_m] + [T_{ims}] + [T_{ims} P_{ims}]. \tag{D.30}$$

Substitutin equations (D.4),(D.5), and (D.7) into equation (D.30), we obtain:

$$[T_{\text{total}}] = [T_m] + \frac{[T_m][S_m] + [T_{ims}][S_{ims}]}{K_m^s} + \frac{[T_m][M_m] + [T_{ims}][M_{ims}]}{K_m^m} \tag{D.31}$$

$$+ [T_{ims}] + \frac{[T_{ims}][P_{ims}] + [T_m][P_m]}{K_m^p}. \tag{D.32}$$

This can be written as:

$$[T_{\text{total}}] = [T_m]\delta_1 + [T_{ims}]\delta_2. \tag{D.33}$$

where

$$\delta_1 = \left(1 + \frac{[S_m]}{K_m^s} + \frac{[M_m]}{K_m^m} + \frac{[P_m]}{K_m^p}\right)$$

$$\delta_2 = \left(1 + \frac{[S_{ims}]}{K_m^s} + \frac{[M_{ims}]}{K_m^m} + \frac{[P_{ims}]}{K_m^p}\right).$$

Substituting equation (D.29) into equation (D.33), we get:

$$[T_{\text{total}}] = [T_m]\delta_1 + [T_m]\phi_1\delta_2. \tag{D.34}$$

Solving for $[T_m]$:

$$[T_m] = \frac{[T_{\text{total}}]}{\delta_1 + \phi_1\delta_2}. \tag{D.35}$$

Substituting equation(D.35) into equation (D.15), we obtain:

$$v_1^f = \frac{1}{V_{ims}}\left[\frac{[T_{\text{total}}]}{\delta_1 + \phi_1\delta_2}\left(\frac{[S_m]}{K_s} - \frac{\phi_1[S_{ims}]}{K_s}\right) + \frac{[T_{\text{total}}]}{\delta_1 + \phi_1\delta_2}\left(\frac{[M_m]}{K_m} - \frac{\phi_1[M_{ims}]}{K_m}\right)\right]. \tag{D.36}$$

After simplifying, we get:

$$v_1^f = \frac{1}{V_{ims}}\left[\frac{[T_{\text{total}}]}{\delta_1 + \phi_1\delta_2}\left(\frac{k_3^s\left([S_m] - \phi_1[S_{ims}]\right)}{K_m^s}\right) + \frac{[T_{\text{total}}]}{\delta_1 + \phi_1\delta_2}\left(\frac{k_3^m\left([M_m] - \phi_1[M_{ims}]\right)}{K_m^m}\right)\right]. \tag{D.37}$$

This can be written as:

$$v_1^f = \frac{1}{V_{ims}}\left[\frac{T_{max}^s\left([S_m] - \phi_1[S_{ims}]\right)}{K_m^s\delta_1 + K_m^s\phi_1\delta_2} + \frac{T_{max}^m\left([M_m] - \phi_1[M_{ims}]\right)}{K_m^m\delta_1 + K_m^m\phi_1\delta_2}\right], \tag{D.38}$$

where $T_{max}^s = k_3^s[T_{total}]$, and $T_{max}^m = k_3^m[T_{total}]$

Similarly, substituting equation equation(D.35) into equation (D.20), we obtain:

$$v_2^f = \frac{1}{V_m}\left[[T_m]\phi_1\left(\frac{[P_{ims}]}{K_p}\right) - [T_m]\left(\frac{[P_m]}{K_p}\right)\right], \tag{D.39}$$

Which simplifies to:

$$v_2^f = \frac{1}{V_m}\left[[T_m]\left(\frac{\phi_1[P_{ims}]}{K_p} - \frac{[P_m]}{K_p}\right)\right]. \tag{D.40}$$

Substituting equation (D.35), we obtain:

$$v_2^f = \frac{1}{V_m}\left[\frac{[T_{\text{total}}]}{\delta_1 + \phi_1\delta_2}\left(\frac{k_3^p\left(\phi_1[P_{ims}] - [P_m]\right)}{K_m^p}\right)\right], \tag{D.41}$$

which can be written as:

$$v_2^f = \frac{1}{V_m}\left(\frac{T_{max}^p\left(\phi_1[P_{ims}] - [P_m]\right)}{K_m^p\delta_1 + K_m^p\phi_1\delta_2}\right), \tag{D.42}$$

where $T_{max}^p = k_3^p[T_{\text{total}}]$.

Appendix D.2 Reverse Cycle

For the reverse cycle, the flux of dicarboxylates into the matrix is given by

$$v_1^r = \frac{d[S_m]}{dt} + \frac{d[M_m]}{dt} \tag{D.43}$$

$$= \frac{1}{V_m}\left(k_{-1}^s[T_{ims}S_{ims}] - k_1^s[T_m][S_m] + k_{-1}^m[T_{ims}M_{ims}] - k_1^m[T_m][M_m]\right). \tag{D.44}$$

Similar to the forward cycle, under the quasi–steady-state assumption the $T_{ims}S_{ims}, T_{ims}M_{ims}, T_{ims}P_{ims}$ are balanced in the reverse cycle, resulting in constant concentrations of these intermediates.

$$\frac{d[T_{ims}S_{ims}]}{dt} = k_1^s[T_m][S_m] - k_{-1}^s[T_{ims}S_{ims}] - k_3^s[T_{ims}S_{ims}] + k_{-3}^s[T_{ims}][S_{ims}] = 0 \tag{D.45}$$

$$[T_{ims}S_{ims}] = \frac{k_1^s[T_m][S_m]}{k_{-1}^s + k_3^s} + \frac{k_{-3}^s[T_{ims}][S_{ims}]}{k_{-1}^s + k_3^s}. \tag{D.46}$$

By substituting eq. (D.3) into eq. (D.46), the concentration of T_mS_m becomes:

$$[T_{ims}S_{ims}] = \frac{[T_m][S_m] + [T_{ims}][S_{ims}]}{K_m^s} \tag{D.47}$$

similarly,

$$[T_{ims}M_{ims}] = \frac{[T_m][M_m] + [T_{ims}][M_{ims}]}{K_m^m}. \tag{D.48}$$

and

$$[T_m P_m] = \frac{[T_{ims}][P_{ims}] + [T_m][P_m]}{K_m^p}. \tag{D.49}$$

substituting eq. (D.47) and (D.48) in eq. (D.44) we get:

$$\begin{aligned} v_1^r = \frac{1}{V_m}\Bigg(& k_{-1}^s \frac{[T_m][S_m] + [T_{ims}][S_{ims}]}{K_m^s} - k_1^s [T_m][S_m] \\ & + k_{-1}^m \frac{[T_m][M_m] + [T_{ims}][M_{ims}]}{K_m^m} - k_1^m [T_m][M_m] \Bigg). \end{aligned} \tag{D.50}$$

$$v_1^r = \frac{1}{V_m}\left(\frac{k_{-1}^s [T_{ims}][S_{ims}] - k_3^s [T_m][S_m]}{K_m^s} + \frac{k_{-1}^m [T_{ims}][M_{ims}] - k_3^m [T_m][M_m]}{K_m^m} \right), \tag{D.51}$$

using symmetry, we can further simplify it into:

$$v_1^f = \frac{1}{V_m}\left(\frac{k_3^s \left([T_{ims}][S_{ims}] - [T_m][S_m]\right)}{K_m^s} + \frac{k_3^m \left([T_{ims}][M_{ims}] - [T_m][M_m]\right)}{K_m^m} \right), \tag{D.52}$$

$$v_1^r = \frac{1}{V_m}\left[[T_{ims}] \left(\frac{[S_{ims}]}{K_s} + \frac{[M_{ims}]}{K_m} \right) - [T_m] \left(\frac{[S_m]}{K_s} + \frac{[M_m]}{K_m} \right) \right], \tag{D.53}$$

where $K_s = \frac{K_3^s}{K_m^s}$ and $K_m = \frac{K_3^m}{K_m^m}$.

$$v_2^r = \frac{d[P_{ims}]}{dt} = \frac{1}{V_{ims}}\left(k_{-1}^p [T_m P_m] - k_1^p [T_{ims}][P_{ims}] \right). \tag{D.54}$$

$$v_2^r = \frac{1}{V_{ims}}\left(k_{-1}^p \frac{[T_{ims}][P_{ims}] + [T_m][P_m]}{K_m^p} - k_1^p [T_{ims}][P_{ims}] \right), \tag{D.55}$$

where K_m^p is the Michaelis constant for the secondary substrate P_{ims}. By substituting K_m^p from equation (D.8), we can simplify this equation as follows:

$$v_2^r = \frac{1}{V_{ims}}\left(\frac{k_{-1}^p [T_m][P_m] - k_3^p [T_{ims}][P_{ims}]}{K_m^p} \right), \tag{D.56}$$

using symmetry, we can further simplified it into:

$$v_2^r = \frac{1}{V_{ims}}\left(\frac{k_3^p [T_m][P_m] - k_3^p [T_{ims}][P_{ims}]}{K_m^p} \right), \tag{D.57}$$

$$v_2^r = \frac{1}{V_{ims}}\left[[T_m] \left(\frac{[P_m]}{K_p} \right) - [T_{ims}] \left(\frac{[P_{ims}]}{K_p} \right) \right], \tag{D.58}$$

where $K_p = \frac{K_3^p}{K_m^p}$.

$$\frac{1}{V_m}\left[[T_{ims}]\left(\frac{[S_{ims}]}{K_s}+\frac{[M_{ims}]}{K_m}\right)-[T_m]\left(\frac{[S_m]}{K_s}+\frac{[M_m]}{K_m}\right)\right]=\frac{1}{V_{ims}}\left[[T_m]\left(\frac{[P_m]}{K_p}\right)-[T_{ims}]\left(\frac{[P_{ims}]}{K_p}\right)\right], \tag{D.59}$$

$$\frac{[T_{ims}]}{V_m}\left(\frac{[S_{ims}]}{K_s}+\frac{[M_{ims}]}{K_m}\right)-\frac{[T_m]}{V_m}\left(\frac{[S_m]}{K_s}+\frac{[M_m]}{K_m}\right)=\frac{[T_m]}{V_{ims}}\left(\frac{[P_m]}{K_p}\right)-\frac{[T_{ims}]}{V_{ims}}\left(\frac{[P_{ims}]}{K_p}\right), \tag{D.60}$$

$$\frac{[T_{ims}]}{V_m}\left(\frac{[S_{ims}]}{K_s}+\frac{[M_{ims}]}{K_m}\right)+\frac{[T_{ims}]}{V_{ims}}\left(\frac{[P_{ims}]}{K_p}\right)=\frac{[T_m]}{V_{ims}}\left(\frac{[P_m]}{K_p}\right)+\frac{[T_m]}{V_m}\left(\frac{[S_m]}{K_s}+\frac{[M_m]}{K_m}\right), \tag{D.61}$$

$$[T_{ims}]\left(\frac{[S_{ims}]}{V_mK_s}+\frac{[M_{ims}]}{V_mK_m}+\frac{[P_{ims}]}{V_{ims}K_p}\right)=[T_m]\left(\frac{[P_m]}{V_{ims}K_p}+\frac{[S_m]}{V_mK_s}+\frac{[M_m]}{V_mK_m}\right), \tag{D.62}$$

$$[T_m]\left(\beta_1[S_m]+\beta_2[M_m]+\beta_3[P_m]\right)=[T_{ims}]\left(\beta_3[P_{ims}]+\beta_1[S_{ims}]+\beta_2[M_{ims}]\right), \tag{D.63}$$

where $\beta_1 = \frac{V_{ims}}{V_m}\lambda_1$, $\beta_2 = \frac{V_{ims}}{V_m}\lambda_2$, and $\beta_3 = \frac{V_m}{V_{ims}}\lambda_3$

$$[T_m]\left(\frac{\beta_1[S_m]+\beta_2[M_m]+\beta_3[P_m]}{\beta_1[S_{ims}]+\beta_2[M_{ims}]+\beta_3[P_{ims}]}\right)=[T_{ims}], \tag{D.64}$$

$$[T_m]\left(\frac{[S_m]+\frac{\beta_2}{\beta_1}[M_m]+\frac{\beta_3}{\beta_1}[P_m]}{[S_{ims}]+\frac{\beta_2}{\beta_1}[M_{ims}]+\frac{\beta_3}{\beta_1}[P_{ims}]}\right)=[T_{ims}], \tag{D.65}$$

$$[T_m]\phi_2=[T_{ims}], \tag{D.66}$$

where $\frac{\beta_2}{\beta_1} = \frac{\frac{V_{ims}}{V_m}\lambda_2}{\frac{V_{ims}}{V_m}\lambda_1} = \lambda_{21}$, and $\frac{\beta_3}{\beta_1} = \frac{\frac{V_m}{V_{ims}}\lambda_3}{\frac{V_{ims}}{V_m}\lambda_1} = (\frac{V_m}{V_{ims}})^2\lambda_{31}$

$$\phi_2=\left(\frac{[S_m]+\lambda_{21}[M_m]+(\frac{V_m}{V_{ims}})^2\lambda_{31}[P_m]}{[S_{ims}]+\lambda_{21}[M_{ims}]+(\frac{V_m}{V_{ims}})^2\lambda_{31}[P_{ims}]}\right)$$

$$\phi_2=\left(\frac{[S_m]+\lambda_{21}[M_m]+(\frac{V_m}{V_{ims}})^2\lambda_{31}[P_m]}{[S_{ims}]+\lambda_{21}[M_{ims}]+(\frac{V_m}{V_{ims}})^2\lambda_{31}[P_{ims}]}\right)$$

$$\phi_2=\frac{\lambda_1[S_m]+\lambda_2[M_m]+(\frac{V_m}{V_{ims}})^2\lambda_3[P_m]}{\lambda_1[S_{ims}]+\lambda_2[M_{ims}]+(\frac{V_m}{V_{ims}})^2\lambda_3[P_{ims}]}$$

Appendix D.2.1 Total Transporter Conservation

The total transporter concentration $[T_{\text{total}}]$ is distributed between all transporter states, leading to the expression:

$$[T_{\text{total}}] = [T_m] + [T_{ims}S_{ims}] + [T_{ims}M_{ims}] + [T_{ims}] + [T_mP_m]. \tag{D.67}$$

$$[T_{\text{total}}] = [T_m] + \frac{[T_m][S_m] + [T_{ims}][S_{ims}]}{K_m^s} + \frac{[T_m][M_m] + [T_{ims}][M_{ims}]}{K_m^m} \tag{D.68}$$

$$+ [T_{ims}] + \frac{[T_{ims}][P_{ims}] + [T_m][P_m]}{K_m^p}. \tag{D.69}$$

$$[T_{\text{total}}] = [T_m]\delta_1 + [T_{ims}]\delta_2. \tag{D.70}$$

$$\delta_1 = \left(1 + \frac{[S_m]}{K_m^s} + \frac{[M_m]}{K_m^m} + \frac{[P_m]}{K_m^p}\right)$$

$$\delta_2 = \left(1 + \frac{[S_{ims}]}{K_m^s} + \frac{[M_{ims}]}{K_m^m} + \frac{[P_{ims}]}{K_m^p}\right)$$

$$[T_{\text{total}}] = [T_m]\delta_1 + [T_m]\phi_2\delta_2. \tag{D.71}$$

$$[T_m] = \frac{[T_{\text{total}}]}{\delta_1 + \phi_2\delta_2} \tag{D.72}$$

$$v_1^r = \frac{1}{V_m}\left[[T_{ims}]\left(\frac{[S_{ims}]}{K_s} + \frac{[M_{ims}]}{K_m}\right) - [T_m]\left(\frac{[S_m]}{K_s} + \frac{[M_m]}{K_m}\right)\right], \tag{D.73}$$

$$v_1^r = \frac{1}{V_m}\left[[T_m]\phi_2\left(\frac{[S_{ims}]}{K_s} + \frac{[M_{ims}]}{K_m}\right) - [T_m]\left(\frac{[S_m]}{K_s} + \frac{[M_m]}{K_m}\right)\right], \tag{D.74}$$

$$v_1^r = \frac{1}{V_m}\left[\frac{[T_{\text{total}}]}{\delta_1 + \phi_2\delta_2}\left(\frac{\phi_2[S_{ims}]}{K_s} - \frac{[S_m]}{K_s}\right) + \frac{[T_{\text{total}}]}{\delta_1 + \phi_2\delta_2}\left(\frac{\phi_2[M_{ims}]}{K_m} - \frac{[M_m]}{K_m}\right)\right], \tag{D.75}$$

$$v_1^r = \frac{1}{V_m}\left[\frac{[T_{\text{total}}]}{\delta_1 + \phi_2\delta_2}\left(\frac{k_3^s\left(\phi_2[S_{ims}] - [S_m]\right)}{K_m^s}\right)\right. \tag{D.76}$$

$$\left. + \frac{[T_{\text{total}}]}{\delta_1 + \phi_2\delta_2}\left(\frac{k_3^m\left(\phi_2[M_{ims}] - [M_m]\right)}{K_m^m}\right)\right],$$

$$v_1^r = \frac{1}{V_m}\left[\frac{T_{max}^s\left(\phi_2[S_{ims}] - [S_m]\right)}{K_m^s\delta_1 + K_m^s\phi_2\delta_2} + \frac{T_{max}^m\left(\phi_2[M_{ims}] - [M_m]\right)}{K_m^m\delta_1 + K_m^m\phi_2\delta_2}\right], \tag{D.77}$$

where $T_{max}^s = k_3^s[T_{total}]$, and $T_{max}^m = k_3^m[T_{total}]$

$$v_2^r = \frac{1}{V_{ims}}\left[[T_m]\left(\frac{[P_m]}{K_p}\right) - [T_{ims}]\left(\frac{[P_{ims}]}{K_p}\right)\right], \tag{D.78}$$

$$v_2^r = \frac{1}{V_{ims}}\left[[T_m]\left(\frac{[P_m]}{K_p}\right) - [T_m]\phi_2\left(\frac{[P_{ims}]}{K_p}\right)\right], \tag{D.79}$$

$$v_2^r = \frac{1}{V_{ims}}\left[[T_m]\left(\frac{[P_m] - \phi_2[P_{ims}]}{K_p}\right)\right], \tag{D.80}$$

$$v_2^r = \frac{1}{V_{ims}}\left[\frac{[T_{\text{total}}]}{\delta_1 + \phi_2\delta_2}\left(\frac{k_3^p\left([P_m] - \phi_2[P_{ims}]\right)}{K_m^p}\right)\right], \tag{D.81}$$

$$v_2^r = \frac{1}{V_{ims}}\left[\frac{T_{max}^p\left([P_m] - \phi_2[P_{ims}]\right)}{K_m^p\delta_1 + K_m^p\phi_2\delta_2}\right], \tag{D.82}$$

where $T_{max}^p = k_3^p[T_{\text{total}}]$.

Appendix D.3 Net Flux of the Complete Cycle

The net exchange (production) rates of succinate and malate for the forward and reverse cycles are given by:

$$V_1^{net} = \frac{1}{V_m}\left[\frac{T_{max}^s\left(\phi_2[S_{ims}] - [S_m]\right)}{K_m^s\delta_1 + K_m^s\phi_2\delta_2} + \frac{T_{max}^m\left(\phi_2[M_{ims}] - [M_m]\right)}{K_m^m\delta_1 + K_m^m\phi_2\delta_2}\right] \tag{D.83}$$

$$- \frac{1}{V_{ims}}\left[\frac{T_{max}^s\left([S_m] - \phi_1[S_{ims}]\right)}{K_m^s\delta_1 + K_m^s\phi_1\delta_2} + \frac{T_{max}^m\left([M_m] - \phi_1[M_{ims}]\right)}{K_m^m\delta_1 + K_m^m\phi_1\delta_2}\right], \tag{D.84}$$

We can express the net flux as the sum of the fluxes for succinate and malate transport:

$$V_1^{net} = J_{succ} + J_{mal}, \tag{D.85}$$

where the flux contribution from succinate (J_{succ}) is:

$$J_{succ} = \frac{1}{V_m}\left[\frac{T_{max}^s\left(\phi_2[S_{ims}] - [S_m]\right)}{K_m^s\delta_1 + K_m^s\phi_2\delta_2}\right] - \frac{1}{V_{ims}}\left[\frac{T_{max}^s\left([S_m] - \phi_1[S_{ims}]\right)}{K_m^s\delta_1 + K_m^s\phi_1\delta_2}\right], \tag{D.86}$$

and the flux contribution from malate (J_{mal}) is:

$$J_{mal} = \frac{1}{V_m}\left[\frac{T_{max}^m\left(\phi_2[M_{ims}] - [M_m]\right)}{K_m^m\delta_1 + K_m^m\phi_2\delta_2}\right] - \frac{1}{V_{ims}}\left[\frac{T_{max}^m\left([M_m] - \phi_1[M_{ims}]\right)}{K_m^m\delta_1 + K_m^m\phi_1\delta_2}\right], \tag{D.87}$$

with

$$\delta_1 = \left(1 + \frac{[S_m]}{K_m^s} + \frac{[M_m]}{K_m^m} + \frac{[P_m]}{K_m^p}\right),$$

$$\delta_2 = \left(1 + \frac{[S_{ims}]}{K_m^s} + \frac{[M_{ims}]}{K_m^m} + \frac{[P_{ims}]}{K_m^p}\right),$$

$$\phi_1 = \left(\frac{[S_m] + \lambda_{21}[M_m] + \lambda_{31}[P_m]}{[S_{ims}] + \lambda_{21}[M_{ims}] + \lambda_{31}[P_{ims}]}\right),$$

$$\phi_2 = \left(\frac{[S_m] + \lambda_{21}[M_m] + (\frac{V_m}{V_{ims}})^2\lambda_{31}[P_m]}{[S_{ims}] + \lambda_{21}[M_{ims}] + (\frac{V_m}{V_{ims}})^2\lambda_{31}[P_{ims}]}\right).$$

The net exchange (production) rate of phosphate is given by:

$$V_2^{net} = \frac{1}{V_{ims}}\left[\frac{T_{max}^p\left([P_m] - \phi_2[P_{ims}]\right)}{K_m^p\delta_1 + K_m^p\phi_2\delta_2}\right] - \frac{1}{V_m}\left(\frac{T_{max}^p\left(\phi_1[P_{ims}] - [P_m]\right)}{K_m^p\delta_1 + K_m^p\phi_1\delta_2}\right), \tag{D.88}$$

and the corresponding net flux for phosphate can be written as:

$$J_{pho} = \frac{1}{V_{ims}}\left[\frac{T_{max}^p\left([P_m] - \phi_2[P_{ims}]\right)}{K_m^p\delta_1 + K_m^p\phi_2\delta_2}\right] - \frac{1}{V_m}\left(\frac{T_{max}^p\left(\phi_1[P_{ims}] - [P_m]\right)}{K_m^p\delta_1 + K_m^p\phi_1\delta_2}\right). \tag{D.89}$$

Appendix E Simulating the Effect of Succinate dehydrogenase (SDH) on the Dynamics of the SLC25A10 Transporter

Succinate dehydrogenase (SDH) is an enzyme involved in both the tricarboxylic acid (TCA) cycle and the electron transport chain (ETC). It takes part in tranportation of electrons by catalyzing the oxidation of succinate into fumarate (F) while reducing ubiquinone (Q) to ubiquinol (QH_2). This reaction results in the depletion of the mitochondrial succinate pool, affecting the fluxes and dynamics of the SLC25A10 transporter due to its role in exchanging succinate with phosphate. The electron transfer reactions catalyzed by SDH or Complex II are:

$$\mathrm{S}_m + \mathrm{FAD}_m \rightleftharpoons \mathrm{F}_m + \mathrm{FADH}_{2m} \tag{E.1}$$

$$\mathrm{FADH}_{2m} + \mathrm{Q}_m \rightleftharpoons \mathrm{FAD}_m + \mathrm{QH}_m \tag{E.2}$$

These reactions can be lumped into a single reaction:

$$\mathrm{S}_m + \mathrm{Q}_m \rightleftharpoons \mathrm{F}_m + \mathrm{QH}_m \tag{E.3}$$

where S_m denotes mitochondrial succinate, Q_m denotes ubiquinone, F_m denotes mitochondrial fumarate and QH_m denotes mitochondrial ubiquinol.

The overall reaction flux, J_{SDH}, is adopted from Shima Sadri et al. (2023), who modeled using a reversible bi-bi kinetic equation, the flux equation is as follow:

$$J_{\mathrm{SDH}} = \frac{V_{\max}^{sdh}\left(\frac{[\mathrm{S}_m][\mathrm{Q}_m]}{k_m^{s,\mathrm{eff}}k_m^q} - \frac{[\mathrm{F}_m][\mathrm{QH}_m]}{k_m^f k_m^{qh} K_{\mathrm{eq}}^{sdh}}\right)}{\left(1 + \frac{[S_m]}{k_m^{s,\mathrm{eff}}} + \frac{[F_m]}{k_m^f}\right)\left(1 + \frac{[Q_m]}{k_m^q} + \frac{[QH_m]}{k_m^{qh}}\right)} \tag{E.4}$$

where $k_m^{s,\text{eff}}$ is the effective succinate binding constant and calculated as follow:

$$k_m^{s,\text{eff}} = k_m^{s,sdh}\left(\frac{k_m^o + [O_m]}{k_m^o}\right)\left(\frac{k_m^{m,sdh}}{k_m^{m,sdh} + [M_m]}\right) \tag{E.5}$$

this modification to the succinate binding constant ($k_m^{s,sdh}$) reveals that SDH is inhibited by oxaloacetate (O_m) accumulation and stimulated by malate (M_m) accumulation in the mitochondrial matrix. The equilibrium constant (K_{eq}^{sdh}) is derived from the Gibbs free energy:

$$K_{\text{eq}} = e^{-\Delta G'^0_{sdh}/RT} \tag{E.6}$$

where is $\Delta G'^0_{sdh}$ is gibbs free energy for SDH enzyme. The kinetic parameters for the SDH model are given in Table 6.

Table 6: SDH Model Kinetic Parameters

Parameter	Definition	Value	Units	Ref.
$V_{\max}^{sdh}$	Maximum forward reaction rate	100	$\mu mol/min/g$	Assumed
$k_m^{s,sdh}$	Succinate binding constant	1.80×10^{-3}	M	[17]
k_m^q	Ubiquinone binding constant	140×10^{-6}	M	[17]
k_m^f	Fumarate binding constant	1.80×10^{-3}	M	[17]
k_m^{qh}	Ubiquinol binding constant	2.45×10^{-6}	M	[17]
k_m^o	Oxaloacetate binding constant	0.0315×10^{-6}	M	[17]
k_m^m	Malate binding constant	11.7×10^{-6}	M	[17]
$\Delta G'^0_{sdh}$	Gibbs free energy of the reaction (pH=7)	-2.41	KJ/mol	[17]

The fixed mitochondrial concentrations of metabolites involved in the SCAS reaction are given in Table 7.

Table 7: Fixed Mitochondrial Concentrations for SDH Model

Metabolite	Concentration	Unit	Source
F_m	10	mM	[17]
O_m	10	mM	[17]
Q_m	3.75×10^{-1}	mM	[17]
QH_{2m}	1.12	mM	[17]

We incorporate the flux of this reaction (J_{sdh}) as an external source into reduced SLC25A10 model with a negative sign, representing the catalytic efficiency of SDH. A high activity level implies rapid depletion of mitochondrial succinate due to its conversion to fumarate. Conversely, low activity indicates succinate accumulation within mitochondria, whereas moderate activity corresponds to balanced succinate metabolism. The modified system of ordinary differential equations (ODEs) thus becomes:

$$\frac{dM_m}{dt} = J_{mal}, \tag{E.7}$$

$$\frac{dM_{ims}}{dt} = -J_{mal}, \tag{E.8}$$

$$\frac{dS_m}{dt} = J_{succ} - J_{sdh}, \tag{E.9}$$

$$\frac{dS_{ims}}{dt} = -J_{succ}, \tag{E.10}$$

$$\frac{dP_m}{dt} = -J_{pho}, \tag{E.11}$$

$$\frac{dP_{ims}}{dt} = J_{pho}. \tag{E.12}$$

Appendix F Simulating the Effect of Succinyl-CoA synthetase (SCoAS) on the Dynamics of the SLC25A10 Transporter

Succinyl–CoA synthetase (SCoAS), also known as succinyl–CoA ligase, is another enzyme which is involved in TCA cycle. This enzyme catalysis the reversable reaction of conversion of succinyl-coA to succinate. The free energy released from this reaction drives the substrate-level phosphorylation of guanosine diphosphate (GDP) to guanosine triphosphate (GTP), using inorganic mitochondrial phosphate (P_m). This reaction result into depletion of mitochondrial phosphate pool and increasing the mitochondrial succinate pool by conversion of succinyl-coA to succinate. Therefore it affects the fluxes and dynamic of SLC25A10 transporter. The chemical reactions are:

$$\mathrm{SCoA_m + GDP_m + P_m \rightleftharpoons S_m + GTP_m + CoA_m + H_m^+}$$

We adopte overal flux model of this transporter form sadri et al. (2023). The overall reaction flux, J_{SCAS}, is given by:

$$J_{\mathrm{SCAS}} = \frac{V_{\max}^{scas}\left(\frac{[\mathrm{SCoA}_m][\mathrm{GDP}_m][\mathrm{P}_m]}{K_m^{scoa}K_m^{gdp}K_m^{p,scas}} - \frac{[\mathrm{S}_m][\mathrm{GTP}_m][\mathrm{CoA}_m]}{K_m^{s,scas}K_m^{gtp}K_m^{coa}K'_{\mathrm{eq,scas}}}\right)}{\left(1+\frac{[\mathrm{SCoA}_m]}{K_m^{scoa}}+\frac{[\mathrm{S}_m]}{K_m^{s,scas}}+\frac{[\mathrm{CoA}_m]}{K_m^{coa}}+\frac{[\mathrm{S}_m][\mathrm{CoA}_m]}{K_m^{s,scas}K_m^{coa}}\right)\left(1+\frac{[\mathrm{GDP}_m]}{K_m^{gdp}}+\frac{[\mathrm{P}_m]}{K_m^{p,scas}}+\frac{[\mathrm{GTP}_m]}{K_m^{gtp}}+\frac{[\mathrm{GDP}_m][\mathrm{P}_m]}{K_m^{p,scas}K_m^{gdp}}\right)} \tag{F.1}$$

where equilibrium constant ($K'_{\mathrm{eq,scas}}$) for this reaction is:

$$K'_{\mathrm{eq,SCAS}} = \exp\left(\frac{-\Delta G'^{0}_{\mathrm{SCAS}}}{RT}\right) \times 10^{\mathrm{pH}_m - 7} \tag{F.2}$$

this equation incorporate the effect of pH because of generation of one proton.

The kinetic parameters for the SCAS model are given in Table 8.

The fixed mitochondrial concentrations of metabolites involved in the SCAS reaction are given in Table 9.

Table 8: SCAS Model Kinetic Parameters

Parameter	Definition	Value	Unit	Reference
$V_{\max}^{scas}$	Maximum forward reaction rate	100	$\mu mol \times min^{-1} \times g^{-1}$	Assumed
K_m^{scoa}	SCoA binding constant	12.5×10^{-6}	M	[17]
K_m^{gdp}	GDP binding constant	5.70×10^{-6}	M	[17]
$K_m^{p,scas}$	Pi binding constant	2.10×10^{-3}	M	[17]
$K_m^{s,scas}$	SUC binding constant	451×10^{-6}	M	[17]
K_m^{gtp}	GTP binding constant	23.1×10^{-6}	M	[17]
K_m^{coa}	CoA binding constant	17.7×10^{-6}	M	[17]
$\Delta G'^{0}_{\text{SCAS}}$	Gibbs free energy of the reaction (pH=7)	1.26	$KJ \times mol^{-1}$	[17]

Table 9: Fixed Mitochondrial Concentrations for SCAS Model

Metabolite	Concentration	Unit	Source
SCoA_m	10×10^{-3}	M	[17]
GDP_m	2.5×10^{-5}	M	[17]
P_m	1×10^{-3}	M	[17]
S_m	0.5×10^{-3}	M	[17]
GTP_m	9.75×10^{-4}	M	[17]
CoA_m	10×10^{-3}	M	[17]

Appendix G Description of the experimental work

To elucidate the metabolic consequences of diminished SLC25A10 activity, we conducted a comparative metabolomic analysis. We utilized immortalized murine chromaffin cells (imCCs) wherein an inducible knockdown of Slc25a10 (SLC25A10-KD) was established, alongside corresponding scramble imCCs serving as controls. Subsequent to the verification of Slc25a10 knockdown efficiency, cellular metabolites extracts from both SLC25A10-KD and scramble imCCs were subjected to comprehensive liquid chromatography-mass spectrometry (LC-MS) based metabolomic profiling.

The metabolomic data revealed significant alterations in the cellular metabolic landscape attributable to SLC25A10 deficiency. As illustrated in the accompanying figures [Ramin, you can refer to your specific figure number here], a targeted analysis, demonstrated a marked accumulation of key dicarboxylates – namely succinate, fumarate, and malonate – in the SLC25A10-KD cells relative to controls. This finding directly aligns with the known function of SLC25A10 as a mitochondrial dicarboxylate transporter, indicating that its reduced expression impairs the mitochondrial efflux or exchange of these metabolites.

Furthermore, a broader, untargeted view of the metabolome (visualized in a volcano plot, Figure 1B) underscored the extensive impact of SLC25A10 knockdown. This analysis highlighted a global metabolic reprogramming, with numerous metabolites exhibiting statistically significant changes in abundance. Among those notably elevated in SLC25A10-KD cells were L-lactic acid, 3-hydroxy-L-proline, urocanic acid, and D-pantothenic acid, in addition to fumaric acid. These widespread metabolic shifts suggest that SLC25A10 plays an integral role in maintaining broader cellular metabolic homeostasis, likely through

its influence on the tricarboxylic acid (TCA) cycle and interconnected pathways.

The detailed metabolomic signature obtained from these experiments, characterizing the impact of SLC25A10 dysfunction, provides a crucial empirical foundation. These data will be instrumental in guiding the development of our envisioned comprehensive mitochondrial dynamic model, which will seek to integrate the functions of SLC25A10 with other mitochondrial transporters and enzymes to better understand and predict mitochondrial and cellular metabolism.

Appendix G.1 Method description

Cell Lines and Culture Conditions: Immortalized murine chromaffin cells (imCCs) [57] were utilized for all experiments. Cells were maintained in Dulbecco's Modified Eagle Medium (DMEM) high glucose (Gibco, Cat# 11965), supplemented with 10% (v/v) fetal bovine serum (FBS; Sigma, Cat# 7524). Cultures were maintained at 37 °C in a humidified atmosphere containing 5% CO_2. Cells were routinely passaged at 70–80% confluency using TrypLE and seeded for experiments.

Generation of Inducible Slc25a10 Knockdown imCCs: To generate imCCs with inducible knockdown of Slc25a10, a Tet-On 3G doxycycline-inducible shRNA lentiviral system (VectorBuilder) was used. This system involves sequential stable expression of the Tet regulatory protein and a Tet-On inducible knockdown sequence. Doxycycline (5 µg/mL) was added to the cells for 48 hours to induce knockdown, after which knockdown efficacy was confirmed via western blotting. Cells were then plated onto 6-well plates, and doxycycline was added the day after plating to induce knockdown. After 48 hours, metabolites were harvested from scramble and knockdown cells for downstream LC-MS analysis.

LC-MS Sample Preparation: Cells were washed with ice-cold saline and scraped into pre-cooled acetonitrile/methanol/water (40:40:20) containing 0.5% formic acid and 1 µg/mL D_6-glutaric acid (internal standard), and immediately placed on ice. After 5 minutes, 8.8 µL of 15% NH_4HCO_3 per 100 µL of sample was added and mixed. Samples were immediately snap-frozen on dry ice for 15 minutes, then centrifuged at 14,800 g for 5 minutes at 4 °C. Supernatants were collected and stored at −80 °C until LC-MS analysis.

LC-MS Analysis: Samples were analysed using an Agilent Infinity II HPLC coupled with an Agilent G6545A qTOF mass spectrometer. Metabolites were separated on a Waters Premier BEH Z-HILIC column (1.7 µm, 2.1 × 150 mm). Mobile phase A consisted of 20 mM ammonium bicarbonate with 0.1% ammonium hydroxide and 0.1% InfinityLab deactivator. Mobile phase B consisted of H_2O:ACN (1:9 ratio) with 0.1% InfinityLab deactivator. The flow rate was 0.2 mL/min with the following gradient: 10% A held for 2 min, ramped to 35% A at 18 min, 70% A at 22 min, 90% A at 22.1 min (held for 2.9 min), followed by 10% A at 25.1 min and held for 5 min. Data processing was performed using Agilent Profinder 10. Normalisation to the internal standard and total protein content was performed using an in-house script.

Appendix H Analytical Equilibrium Concentrations for SLC25A10 Transporter

To derive analytical equilibrium expressions for the concentrations of mitochondrial succinate ($[S_m^{eq}]$), phosphate ($[P_m^{eq}]$), and malate ($[M_m^{eq}]$), as well as IMS succinate ($[S_{ims}^{eq}]$), phosphate ($[P_{ims}^{eq}]$), and malate ($[M_{ims}^{eq}]$), as functions of the initial mitochondrial concentrations ($[S_m^0]$, $[P_m^0]$, $[M_m^0]$) and IMS concentrations ($[S_{ims}^0]$, $[P_{ims}^0]$, $[M_{ims}^0]$), we employ conservation laws and Gibbs free energy minimization.

For the succinate–phosphate electroneutral antiport, the transport reaction is:

$$\mathrm{S}_m^{2-} + \mathrm{P}_{ims}^{2-} \rightleftharpoons \mathrm{S}_{ims}^{2-} + \mathrm{P}_m^{2-}.$$

Here, we assume zero malate concentration and derive analytical expressions for succinate and phosphate on both the matrix and IMS sides.

Let $S_{\text{tot}}, P_{\text{tot}}, \mathcal{M}_{\text{tot}}$, and $\mathcal{I}_{\text{tot}}$ denote the total initial concentration of succinate across both compartments, phosphate across both compartments, total initial substrate concentration in the matrix, and total initial substrate concentration in the IMS, respectively. These quantities are given by:

$$S_{\text{tot}} = [S_m^0] + [S_{ims}^0], \tag{H.1}$$
$$P_{\text{tot}} = [P_m^0] + [P_{ims}^0], \tag{H.2}$$
$$\mathcal{M}_{\text{tot}} = [S_m^0] + [P_m^0], \tag{H.3}$$
$$\mathcal{I}_{\text{tot}} = [S_{ims}^0] + [P_{ims}^0]. \tag{H.4}$$

From conservation laws, we can then write:

$$[S_m^{eq}] + [S_{ims}^{eq}] = S_{\text{tot}}, \tag{H.5}$$
$$[P_m^{eq}] + [P_{ims}^{eq}] = P_{\text{tot}}, \tag{H.6}$$
$$[S_m^{eq}] + [P_m^{eq}] = \mathcal{M}_{\text{tot}}, \tag{H.7}$$
$$[S_{ims}^{eq}] + [P_{ims}^{eq}] = \mathcal{I}_{\text{tot}}. \tag{H.8}$$

The Gibbs free energy change for electroneutral exchange is:

$$\Delta G = RT \ln \left(\frac{[S_{ims}][P_m]}{[S_m][P_{ims}]} \right). \tag{H.9}$$

At equilibrium, $\Delta G = 0$, which implies:

$$[S_{ims}^{eq}][P_m^{eq}] = [S_m^{eq}][P_{ims}^{eq}]. \tag{H.10}$$

Using conservation laws, we express the equilibrium concentrations as:

$$[S_{ims}^{eq}] = [S_m^0] + [S_{ims}^0] - [S_m^{eq}], \tag{H.11}$$
$$[P_m^{eq}] = [S_m^0] + [P_{ims}^0] - [S_m^{eq}], \tag{H.12}$$
$$[P_{ims}^{eq}] = [P_m^0] - [S_m^0] + [S_m^{eq}]. \tag{H.13}$$

Substituting these into the equilibrium condition (Eq. (H.10)) and solving for $[S_m^{eq}]$ yields a quadratic equation, which simplifies to:

$$[S_m^{eq}] = \frac{([S_m^0] + [S_{ims}^0])([S_m^0] + [P_{ims}^0])}{[S_m^0] + [S_{ims}^0] + [P_m^0] + [P_{ims}^0]}. \tag{H.14}$$

The other equilibrium concentrations follow directly:

$$[S_{ims}^{eq}] = \frac{([S_m^0] + [S_{ims}^0])([P_m^0] + [S_{ims}^0])}{[S_m^0] + [S_{ims}^0] + [P_m^0] + [P_{ims}^0]}, \tag{H.15}$$

$$[P_m^{eq}] = \frac{([S_m^0] + [P_{ims}^0])([P_m^0] + [S_{ims}^0])}{[S_m^0] + [S_{ims}^0] + [P_m^0] + [P_{ims}^0]}, \tag{H.16}$$

$$[P_{ims}^{eq}] = \frac{([S_m^0] + [S_{ims}^0])([P_m^0] + [P_{ims}^0])}{[S_m^0] + [S_{ims}^0] + [P_m^0] + [P_{ims}^0]}. \tag{H.17}$$

These closed-form solutions provide the equilibrium partitioning of succinate and phosphate between the mitochondrial matrix and the IMS under SLC25A10-mediated antiport. An analogous derivation can be carried out for malate–phosphate exchange by assuming zero succinate concentration.